

**THEORETICAL INVESTIGATION OF CO₂
ACTIVATION AND CHEMICAL CONVERSION ON
CATALYTIC NANOPARTICLES**

by

Natalie Austin

Bachelor of Science in Chemical Engineering, University of
Maryland, Baltimore County, 2013

Submitted to the Graduate Faculty of
the Swanson School of Engineering in partial fulfillment
of the requirements for the degree of

Doctor of Philosophy

University of Pittsburgh

2018

UNIVERSITY OF PITTSBURGH
SWANSON SCHOOL OF ENGINEERING

This dissertation was presented

by

Natalie Austin

It was defended on

July 19, 2018

and approved by

Giannis Mpourmpakis, PhD, Assistant Professor, Department of Chemical and Petroleum
Engineering

John Keith, PhD, Assistant Professor, Department of Chemical and Petroleum Engineering

Götz Vesper, PhD, Professor, Department of Chemical and Petroleum Engineering

Guofeng Wang, PhD, Associate Professor, Department of Mechanical Engineering and
Materials Science

Dissertation Director: Giannis Mpourmpakis, PhD, Assistant Professor, Department of
Chemical and Petroleum Engineering

Copyright © by Natalie Austin
2018

THEORETICAL INVESTIGATION OF CO₂ ACTIVATION AND CHEMICAL CONVERSION ON CATALYTIC NANOPARTICLES

Natalie Austin, PhD

University of Pittsburgh, 2018

Growing fossil fuel consumption to meet energy demands has led to elevated levels of CO₂ (a greenhouse gas) in the atmosphere, which could have a significant impact on the environment. Novel methods for CO₂ utilization by catalytic conversion to useful chemicals and fuels are of marked interest for the mitigation of the greenhouse gas footprint.

We used electronic structure calculations to assess the conversion of CO₂ by metal nanocatalysts. Our work was focused on Cu based, M-doped (M= Ni and Zr) heterogeneous nanoparticles and their adsorption and activation of CO₂. The strong adsorption and activation of CO₂ we observed was attributed to nanoparticle charge transfer to CO₂. Due to the oxophilic nature of Zr, the interaction of CO₂ with oxidized Cu-Zr was also assessed. We determined that oxidized Zr sites on Cu-Zr can still adsorb and activate CO₂ which indicated that Cu-Zr nanoparticles are promising materials for CO₂ conversion to industrially relevant products.

As an alternative to traditional heterogeneous catalysts, we used computational methods to investigate ligand-protected Au nanoclusters as electrocatalysts for the conversion of CO₂ to CO. We found that CO₂ electroreduction over fully ligand-protected nanoclusters was not feasible because of unfavorable energies required to stabilize CO₂ reduction intermediates. However, we determined that it is thermodynamically feasible to remove ligands from the nanoclusters at experimentally applied potentials. The generated surface sites on the partially ligand-removed nanoclusters were shown to be active for CO₂ reduction as they significantly stabilized reduction intermediates. The generated sites were also active for H₂

evolution, which agrees with experimental observations that these two processes compete. Interestingly, we found that a specific mode of ligand removal results in a catalyst that was both active and selective for CO₂ reduction.

In this work, we used computational tools to provide insights into the effects of nanoparticle morphology and composition on the electronic properties of the nanoparticle. Using these insights, we developed active and selective catalysts for CO₂ conversion. Our investigations into nanoparticle properties and metal-adsorbate interactions, rationalized experimental observations and could serve as design guidelines for developing catalysts for valuable fuels and chemicals production from CO₂.

TABLE OF CONTENTS

PREFACE	xvii
1.0 INTRODUCTION	1
1.1 CO ₂ REDUCTION ON HETEROGENOUS CATALYSTS	2
1.2 CO ₂ REDUCTION ON ELECTROCATALYSTS	4
2.0 CO₂ ACTIVATION ON BIMETALLIC COPPER-NICKEL NANOPARTICLES	7
2.1 COMPUTATIONAL METHODS	7
2.2 RESULTS AND DISCUSSION	8
2.2.1 Structural and Electronic Properties of Cu _{55-x} Ni _x Nanoparticles	8
2.2.2 CO ₂ Adsorption on Cu _{55-x} Ni _x Nanoparticles	10
2.2.3 Descriptors for CO ₂ Adsorption on Cu _{55-x} Ni _x Nanoparticles	15
2.3 CONCLUSIONS	18
3.0 CO₂ ACTIVATION ON BIMETALLIC COPPER-ZIRCONIUM NANOPARTICLES	19
3.1 COMPUTATIONAL METHODS	19
3.2 RESULTS AND DISCUSSION	20
3.2.1 Zr Doping of Cu Nanoparticles	20
3.2.2 CO ₂ Adsorption and Activation on Cu ₅₄ Zr and Cu ₅₅ Nanoparticles	21
3.2.3 CO ₂ Adsorption and Activation on Cu _{55-x} Zr _x (x= 2, 4, 6, 8, 10, 12) Nanoparticles	23
3.2.4 Electronic Properties of CuZr Nanoparticles	26
3.2.5 CO ₂ Dissociation to CO on Cu ₅₄ Zr and Cu ₅₅ Nanoparticles	27

3.2.6	Experimental Observations for CO ₂ Adsorption on CuZr Catalysts	30
3.3	CONCLUSIONS	30
4.0	INFLUENCE OF ATOMIC-LEVEL GOLD CATALYST MORPHOL- OGY ON CO₂ ELECTROREDUCTION	32
4.1	COMPUTATIONAL METHODS	32
4.2	RESULTS AND DISCUSSION	34
4.2.1	Experimental Observations for CO ₂ Reduction on Au ₂₅ Nanoclusters	34
4.2.2	Computational Analysis of CO ₂ Reduction on Au ₂₅ Nanoclusters	35
4.3	CONCLUSIONS	39
5.0	ELUCIDATING THE ACTIVE SITES FOR CO₂ ELECTROREDUC- TION ON LIGAND-PROTECTED GOLD NANOCCLUSERS	40
5.1	COMPUTATIONAL METHODS	40
5.2	RESULTS AND DISCUSSION	44
5.2.1	CO ₂ Reduction and H ₂ Evolution on Fully Ligand-Protected Nan- oclusters	44
5.2.2	CO ₂ reduction and H ₂ Evolution on Partially Ligand-Removed Nan- oclusters	47
5.2.3	CO vs H ₂ Product Selectivity	53
5.3	CONCLUSIONS	56
6.0	FUTURE WORK	57
6.1	KINETIC ANALYSIS FOR LIGAND REMOVAL	57
	APPENDIX. SUPPORTING INFORMATION	59
A.1	CO ₂ Activation on Cu-based Zr-Decorated Nanoparticles	59
A.2	Influence of Atomic-Level Gold Catalyst Morphology on CO ₂ Electroreduction	63
A.3	Elucidating the Active Sites for CO ₂ Electroreduction on Ligand-protected Gold Nanoclusters	68
	BIBLIOGRAPHY	74

LIST OF TABLES

2.1	Calculated BE/n and E_{exc} of the $\text{Cu}_{55-x}\text{Ni}_x$ NPs. The negative values indicate exothermicity.	10
2.2	CO_2 binding energies on the NPs, total charge (NBO) transferred to CO_2 , and geometric properties of gas phase CO_2 (non-interacting) and CO_2 interacting with the NPs. Binding energies are in eVs. Bond lengths of C-O1 and C-O2 are in angstroms, Å. Bond angle of O1-C-O2 are in degrees,°.	13
5.1	Limiting step and potential of the Au_{25} NCs. $\text{H}^+ + \text{e}^-$ omitted for simplicity.	54
A1	Relative energies (to the lowest energy system) in eV of the Au_{25} nanoclusters optimized with different multiplicities.	68
A2	Computed adiabatic electron affinities (AEA) and adiabatic ionization potentials (AIP) of $\text{Au}_{25}(\text{SCH}_3)_{10}^0$, $\text{Au}_{25}(\text{SCH}_3)_{17}^0$, and $\text{Au}_{25}\text{S}(\text{SCH}_3)_{17}^0$ in eV. . .	68

LIST OF FIGURES

2.1	Optimized geometries of 55-atom NPs: monometallic (a) Cu_{55} and (b) Ni_{55} , decorated (c) $\text{Cu}_{43}\text{Ni}_{12}$ and (d) $\text{Cu}_{12}\text{Ni}_{43}$ NP with 12 heteroatoms located at the corner (CN6) sites of the NP, and core-shell (e) $\text{Cu}_{13}\text{Ni}_{42}$ and (f) $\text{Cu}_{42}\text{Ni}_{13}$ with 13 metal atoms located in the core and 42 heteroatoms in the shell. The equivalent CN6 and CN8 sites on the NPs are illustrated in (a). The Cu atoms are colored brown and the Ni blue.	9
2.2	CO_2 adsorption on the (a-b) monometallic, (c-d) decorated, and (e-f) core-shell Cu-Ni NPs. The color code is as depicted in Figure 1 with the addition of CO_2 (C colored grey and oxygen colored red).	12
2.3	Deviation of adsorbed CO_2 average C=O bond length (left ordinate) and O=C=O bond angle (right ordinate) from gas phase CO_2 as functions of CO_2 BE. The inset figure at the bottom left shows a linear relationship between average C=O bond length and O=C=O bond angle.	13
2.4	CO_2 BE as a function of total charge on CO_2 . The dashed black line in serves as a guide to the eye.	14
2.5	CO_2 BE as a function of local d_{C} of the $\text{Cu}_{55-x}\text{Ni}_x$ NPs. The dashed black line serves as a guide to the eye. In (b) the vertical blue line represents the LUMO orbital energy of the CO_2 molecule.	17
2.6	Visual representation of the HOMO orbitals and fractional distribution of the HOMO orbital character of the (a) Cu_{55} , (b) Ni_{55} , (c) $\text{Cu}_{43}\text{Ni}_{12}$, (c) $\text{Cu}_{12}\text{Ni}_{43}$ NPs.	17

3.1	55-atom Cu NP decorated with Zr at the three coordination sites (CN = 6, 8, 12) listed above the NP. The SE values for Zr residing on the CN8 and CN6 sites of the NP are listed below the NP. The Cu atoms are colored brown and the Zr atoms are in light blue.	21
3.2	CI-NEB calculations for the physisorbed to activated state of CO ₂ on the (a) Cu ₅₄ Zr and (b) Cu ₅₅ NP. The values in red in (a) and (b) is the change in energy (ΔE) from the physisorbed to activated state of CO ₂ ($\Delta E = E_{\text{activated}} - E_{\text{physisorbed}}$). The negative (red) value in (a) represents an exothermic step, whereas, the positive value in (b) represents an endothermic step. The color code on the structure is as in Figure 3.1 with the addition of C and O (from CO ₂) colored grey and red, respectively.	23
3.3	(a) Cu _{55-x} Zr _x (x = 2, 4, 6, 8, 10, 12) decoration on the 55-atom NPs. (b) CO ₂ adsorption as a function of surface fraction of Zr on the Cu _{55-x} Zr _x NPs. The dashed lines serve as a guide to the eye. The color code on the structure is as in Figure 3.1.	25
3.4	(a) Deviation of adsorbed CO ₂ geometric properties from gas phase CO ₂ (b) CO ₂ BE as a function of total charge on CO ₂ for each Cu _{55-x} Zr _x (x= 2, 4, 6, 8, 10, 12) NP. The inset figure shows chemisorbed CO ₂ on Cu ₄₃ Zr ₁₂ . The dashed lines in (a) and (b) serve as a guide to the eye. The color code on the structure is as in Figure 3.2.	25
3.5	(a) Cu _{55-x} Zr _x (x = 2, 4, 6, 8, 10, 12) decoration on the 55-atom NPs. The color code is as in Figure 1. (b) CO ₂ adsorption as a function of surface fraction of Zr on the Cu _{55-x} Zr _x NPs. The dashed lines serve as a guide to the eye. The color code on the structure is as in Figure 3.2.	27

3.6	(a) CO ₂ dissociation reaction path on Cu ₅₅ (black line) and Cu ₅₄ Zr (red line). For Cu ₅₅ , TS represents breaking of a C-O bond, with a C-O bond length of 1.87 Å. For Cu ₅₄ Zr, TS1 represents the breaking of a C-O bond, with a C-O bond length of 1.73 Å and TS2 represents the diffusion of O from a top site to hollow site configuration. (b) Optimized structures for the CO ₂ dissociation to CO and O on the Cu ₅₅ (top row) and Cu ₅₄ Zr (bottom row) NPs. The color code on the structure is as in Figure 3.2.	29
4.1	(a) Structures for the nanorod and the nanosphere in the presence of the NH ₄ ⁺ and SbF ₆ ⁻ counterions, respectively. Au atoms are shown in pink, S atoms shown in yellow, C atoms shown in grey, H atoms shown in white, N atoms shown in bright blue, Sb shown in purple, and F shown in light blue. The circled regions on the NCs demonstrate sites of ligand removal on the nanosphere (-SCH ₃) and nanorod (SCH ₃ , -Cl, and PH ₃) (b) ΔG values for ligand removal (in eV) from the NCs at 0 V vs RHE, where LR_NC represents "ligand-removed nanocluster", NS is nanosphere, and NR is nanorod. The blue and green lines represent removing a SCH ₃ and -Cl from the nanorod with SbF ₆ ⁻ counterions, respectively and the red line represents removing SCH ₃ from the nanosphere with a NH ₄ ⁺ counterion. All ligand removal steps are treated as electrochemical reduction steps.	36
4.2	Free energy diagrams (ΔG) for CO ₂ reduction to CO on the ligand-removed NCs at 0 V vs RHE. The black, blue, green, and red lines represent CO ₂ reduction to CO on the nanorod with PH ₃ removed, the nanorod with SCH ₃ removed, the nanorod with -Cl removed, and on the nanosphere with SCH ₃ removed, respectively.	38
5.1	Schematic of the fully-ligand protected Au ₂₅ (SCH ₃) ₁₈ NC. The system is composed of a Au ₁₃ icosahedral core protected by a shell network of six Au ₂ (SR) ₃ . The Au, S, C, and H atoms are colored yellow, blue, grey, and white, respectively. The labels A and B on the Au ₂ (SR) ₃ shell network represent the two distinct types of coordinated sulfur in the NC shell.	42

5.2	A cycle which illustrates potential states of the Au_{25} NC under reaction conditions. The top and bottom rows, show electron transfer to form the fully ligand-protected and partially ligand removed NCs in each charge state, respectively. The vertical steps indicate ligand removal from $\text{Au}_{25}(\text{SR})_{18}^q$ to form $\text{Au}_{25}(\text{SR})_{17}^q$.	44
5.3	Free energy diagrams (ΔG) for the (a) reduction of CO_2 to CO and (b) hydrogen evolution on the fully ligand-protected $\text{Au}_{25}(\text{SCH}_3)_{18}^q$ ($q = -1, 0, +1$) NCs. The black, red, and blue lines represent the energy diagrams generated using a NC in the -1, 0, and +1 charge states, respectively. The solid lines illustrate the energy diagrams at $U = 0$ V, while the dashed lines represent the energy diagrams at an applied potential of $U = -1.0$ V. (c) Illustrations of the CO_2 reduction and the hydrogen evolution reactions. The Au, S, C, and O, atoms are colored yellow, blue, grey, and red, respectively. The H atoms are white, except for H on the carboxyl (in CO_2 reduction) and the adsorbed H (in hydrogen evolution) which are colored lime green for clarity.	46
5.4	(a) Schematic for reduction of the fully ligand-protected NCs ($\text{Au}_{25}(\text{SCH}_3)_{18}^q$) to partially ligand-removed, $\text{Au}_{25}(\text{SCH}_3)_{17}^q$. (b) Free energy diagram for removing one $-\text{SCH}_3$ from the NC. As described in Figure 5.3, the colored, solid, and dashed lines represent the different charge states and energetics at $U = 0$ V and at $U = -1.0$ V, respectively.	48
5.5	Free energy diagrams (ΔG) for the (a) reduction of CO_2 to CO and the (b) hydrogen evolution reaction on the $\text{Au}_{25}(\text{SCH}_3)_{17}^q$ ($q = -1, 0, +1$) NCs (with a ligand removed). (c) Illustrations of CO_2 reduction and H_2 evolution reaction steps. The color code for the diagrams is as described in Figure 5.3.	49
5.6	(a) Schematic for reduction of the fully ligand-protected NC ($\text{Au}_{25}(\text{SCH}_3)_{18}^q$) to one with $-\text{CH}_3$ removed, $\text{Au}_{25}\text{S}(\text{SCH}_3)_{17}^q$. (b) Free energy diagram for removing one $-\text{CH}_3$ from the NC. As described in Figure 5.3, the colored, solid, and dashed lines, represent the charge states, the energetics at $U = 0$ V and at $U = -1.0$ V, respectively.	51

5.7	Free energy diagrams (ΔG) for the (a) reduction of CO_2 to CO and the (b) hydrogen evolution on the $-\text{CH}_3$ removed $\text{Au}_{25}\text{S}(\text{SCH}_3)_{17}^-$ NC and on the $-\text{SCH}_3$ removed $\text{Au}_{25}(\text{SCH}_3)_{17}^-$ NC. The orange and black lines represent the energy diagrams for the $\text{Au}_{25}\text{S}(\text{SCH}_3)_{17}^-$ and $\text{Au}_{25}(\text{SCH}_3)_{17}^-$ NCs, respectively. The solid lines illustrate the energy diagrams at $U = 0$ V, while the dashed lines represent the energy diagrams at an applied potential of $U = -1.0$ V. The color code for (c) the illustrations of CO_2 reduction and H_2 evolution are as described in Figure 5.3.	52
5.8	(a) Difference in limiting potentials of CO_2 reduction and hydrogen evolution ($U_L(\text{CO}_2) - U_L(\text{H}_2)$). The color code represents the three charge states of the Au_{25} NC (black: negative, red: neutral, blue: positive).	55
6.1	Optimized geometry of the solvated $\text{Au}_{25}(\text{SEthPh})_{18}$ NC with 158 H_2O	58
A1	Three initial adsorption configurations of CO_2 on the Cu_{54}Zr NP were considered: (a) CO_2 molecule parallel to the Cu-Zr bond, (b) CO_2 adsorption to the NP with C of CO_2 interacting with Zr on the NP, and (c) perpendicular CO_2 adsorption with the O atom pointing to Zr.	59
A2	Different dopant sites of two Zr atoms in the 55-atom $\text{Cu}_{53}\text{Zr}_2$ NP. The value below each NP is the stability of the NPs relative to the most stable structure found ($\text{Cu}_{53}\text{Zr}_2\text{-1}$).	60
A3	Chemisorbed CO_2 on $\text{Cu}_{53}\text{Zr}_2\text{-1}$ (most stable $\text{Cu}_{53}\text{Zr}_2$ NP as shown in Figure A2). The binding energy of CO_2 has been calculated to be -1.18 eV, which is strong and comparable to the segregated case of Zr.	60
A4	Local partial density of states (PDOS) of the d electrons for the $\text{Cu}_{55-x}\text{Zr}_x$ NPs. The asterisks and the solid lines below the PDOS represent the HOMO orbital energies and d_C of the $\text{Cu}_{55-x}\text{Zr}_x$ NPs. ($x = 2-12$), respectively. The green asterisk corresponds to the LUMO orbital of the CO_2 molecule. It should be noticed that the increasing Zr content brings the NP HOMO orbitals closer to the CO_2 LUMO, resulting to stronger CO_2 adsorption. The IP correlations presented in Figure 5(b) of the manuscript are relevant to the energy of the HOMO orbitals (HOMO energy can approximate the IP).	61

A5	Surface oxidation configurations for the studied Cu ₅₄ Zr NPs, for which the Zr atom is oxidized with either two or four oxygen atoms: a) Cu ₅₄ ZrO ₂ with Zr on a CN=6 site before oxidation. One oxygen atom bridges a Zr-Cu bond, and the other is on a hollow-site position between Cu and Zr. b) Cu ₅₄ ZrO ₄ with Zr on a CN=6 site before oxidation. All four oxygen atoms occupy hollow-site positions between Cu and Zr. c) Cu ₅₄ ZrO ₂ with Zr on a CN=8 site before oxidation. Both oxygen atoms are on hollow sites between Cu and Zr. d) Cu ₅₄ ZrO ₄ with Zr on a CN=8 site before oxidation. All four oxygen atoms are on hollow sites between Cu and Zr.	62
A6	Lowest-energy adsorption configurations of CO ₂ on Cu ₅₄ ZrO ₂ with Zr in a) CN=6 and b) CN=8 adsorption sites before oxidation and Cu ₅₄ ZrO ₄ with Zr in c) CN=6 and d) CN=8 before oxidation	62
A7	CO ₂ -TPD profiles of CuZr/SiC, Cu/SiC, and ZrO ₂ /SiC	63
A8	Electrocatalytic CO ₂ reduction performance of the two Au ₂₅ NCs. (a) Total current density of CO ₂ reduction, (b) Faradaic Efficiency (FE) for CO production over Au ₂₅ nanosphere and nanorod catalysts, (c) FEs for CO and H ₂ at the potential of -1.07 and -1.17 V over Au ₂₅ nanosphere and nanorod, respectively. (d) CO formation rates over Au ₂₅ nanosphere and nanorod. . . .	64
A9	Different structures and associated free energies (ΔG) for the *COOH formation step (with respect to our reference state) on the surface of the NCs with a ligand removed.	65
A10	Different structures and associated free energies (ΔG) for the CO (and H ₂ O) formation step (with respect to our reference state) on the surface of the NCs with a ligand removed.	66

A11 (a) Electronic energies in eV for ligand removal from the nanosphere (black line) and the nanorod (red line). The text on the lines refers to the type of ligand that was removed. From the nanosphere, -SCH ₃ ligands were removed from the numbered sites shown in (b). Note that site 1 is where -SCH ₃ was removed from in the manuscript. From the nanorod, ligands were removed from the numbered sites shown in (c). Note that site 1 is where -Cl was removed from in the manuscript.	67
A12 CO ₂ adsorption on the negatively charged nanoclusters (a) Au ₂₅ (SCH ₃) ₁₈ ⁻ , (b) Au ₂₅ (SCH ₃) ₁₇ ⁻ , (c) Au ₂₅ S(SCH ₃) ₁₇ ⁻ . Note that physisorption was observed on all the nanoclusters in this study (range: -0.07 to -0.16 eV).	69
A13 Changes in electronic energy (ΔE) for the reaction step of SCH ₃ removal from Site A and Site B (shown in manuscript) of the Au ₂₅ (SCH ₃) ₁₈ ⁻ NC (values are in eV).	69
A14 Free energy diagrams (ΔG) for the (a) reduction of CO ₂ to CO and the (b) hydrogen evolution reaction on the Au ₂₅ (SCH ₃) ₁₇ ⁻ NC with and without solvation effects in red and black, respectively. The Au ₂₅ (SCH ₃) ₁₇ ⁻ NC and all reaction species were reoptimized with and without solvation in Turbomole using PBE/TZVP to utilize the implicit solvation model, COSMO.	70
A15 Electronic energy comparison for the reaction step of -SR and -R removal from Au ₂₅ (SCH ₃) ₁₈ ⁻ and Au ₂₅ (EthPh) ₁₈ ⁻ . The similar magnitude of the electronic energies between ligand removal on Au ₂₅ (SCH ₃) ₁₈ ⁻ and Au ₂₅ (EthPh) ₁₈ ⁻ suggests that similar trends would hold for free energies, as electronic energies capture the majority of enthalpic contributions. This indicates that under reaction conditions removal of experimentally utilized ligands (-SEthPh) is possible.	71
A16 Bader charge analysis of select atoms from the negatively charged nanoclusters (a) Au ₂₅ (SCH ₃) ₁₈ ⁻ , (b) Au ₂₅ (SCH ₃) ₁₇ ⁻ , (c) Au ₂₅ S(SCH ₃) ₁₇ ⁻	72

A17	The projected density of states, PDOS (top graphs) for a ligand Au atom and a S atom of (a) $\text{Au}_{25}(\text{SCH}_3)_{18}^-$, the exposed Au atom of (b) $\text{Au}_{25}(\text{SCH}_3)_{17}^-$, and the exposed S atom of (c) $\text{Au}_{25}\text{S}(\text{SCH}_3)_{17}^-$. Comparison of the exposed S atom PDOS (s and p states) to the S atom PDOS of the fully protected NC, shows an increase in the electron density near the Fermi level (0 eV) of the $\text{Au}_{25}\text{S}(\text{SCH}_3)_{17}^-$ NC which contributes to the reactivity of the NC. The total density of states for the (a) $\text{Au}_{25}(\text{SCH}_3)_{18}^-$, (b) $\text{Au}_{25}(\text{SCH}_3)_{17}^-$, (c) $\text{Au}_{25}\text{S}(\text{SCH}_3)_{17}^-$ NCs are shown in the bottom graphs.	72
A18	(a) HOMO-LUMO energy gaps (in eV) of the fully-protected and partially ligand-removed NCs. A dramatic decrease in the gap is observed with ligand removal. (b) Plots of the HOMO-LUMO orbitals. The white arrows point to the ligand removed sites (-SCH ₃ and -CH ₃) from the NCs. Compared to $\text{Au}_{25}(\text{SCH}_3)_{18}^-$, the electron density on the exposed Au site of $\text{Au}_{25}(\text{SCH}_3)_{17}^-$ becomes more localized and the exposed S site of $\text{Au}_{25}(\text{SCH}_3)_{17}^-$ becomes more directional, both of which contribute to the reactivity of these generated sites.	73

PREFACE

There are many people I would like to thank for making this work possible and for making my studies at Pitt a great experience. First, I would like to thank my advisor and the members of my committee. Dr Giannis Mpourmpakis supported and advised me throughout my PhD research. I am grateful that he gave me the opportunity to work in his lab despite my initially minimal experience in computational research. I have come a long way thanks to all his patience and efforts. Dr. John Keith helped me broaden my knowledge of computational chemistry principles. Dr. Götz Vesper provided me with valuable experimental angles and broader perspectives in my research. Dr. Guofeng Wang gave me great insight into computational approaches that would benefit my work.

I am very thankful to graduate members of the Mpourmpakis Lab (CANELA), Pavlo, Michael T, James, Zihao, Michael C, Xi, and Robin. I would also like to give thanks to post-doc Dr. Mudit Dixit and the undergraduate members of the lab. Over the years they have all been positive role models in my life and work.

I would also like to give thanks to our experimental collaborators Dr. Rongchao Jin and his graduate student Shuo Zhao from Carnegie Mellon University, and Dr. James McKone for expanding my insights in the field of electrocatalysis.

I would like to thank my family, the Austin's, and my Pittsburgh Family: Tom, the Finnegan's, and the Jacoby's for their continuous support. They all provided me with great words of wisdom and motivation to keep me going and inspired me to reach for success. I appreciate them all very much.

Finally, I gratefully acknowledge the funding towards my PhD from the National Science Foundation Graduate Research Fellowship under Grant No. (1247842).

1.0 INTRODUCTION

Overproduction of carbon dioxide (CO_2), a greenhouse gas, through anthropogenic sources is a significantly detrimental result of the worlds utilization of fossil fuels. High prevalence of CO_2 contributes to climate change (temperature increase) which increases the risk for loss of major bodies of ice and sudden shifts in agricultural systems [1]. In the mid-1700s (preindustrial society), the concentration of CO_2 in the atmosphere was about 280 ppm [2]. In the 21st century, the concentration of CO_2 in the atmosphere is about 400 ppm [3], which is over the 350 ppm boundary that has been suggested by scientists across the world [4]. Increasing concerns about greenhouse gas effects on the Earth gives urgency to the design of economically and environmentally sustainable technologies that minimize the human generated carbon footprint. A viable option to mitigate the effects of CO_2 is to convert the significant source of carbon, as a C1 feedstock, into useful chemical and fuels. The diverse physical and chemical properties of metal nanoparticles (NPs) make them attractive catalysts for CO_2 conversion into valuable commodities. Thus the use of chemicals and fuels derived by renewable means could offset the negative impacts that our current reliance on fossil fuels has on the environment.

1.1 CO₂ REDUCTION ON HETEROGENOUS CATALYSTS

Catalytic conversion of CO₂ to valuable products is of significant interest as a method to alleviate the effects of CO₂ on our environment [2, 5]. The high thermodynamic stability of CO₂ limits its application in the chemical industry to a few processes including the synthesis of urea and carbonates [6, 7]. However, the abundance and low-cost of CO₂ makes it an attractive carbon source to investigate its direct chemical transformation to other important products such as CH₃OH, formic acid, hydrocarbons, and CO [2, 8].

Atomic hydrogen serves as a highly reactive reducing species to convert CO₂ to relevant chemicals and fuels in hydrogenation reactions [9–12]. The direct dissociation of CO₂ to produce CO ($\text{CO}_2 \rightarrow \text{CO}^* + \text{O}^*$) can occur even in the absence of reducing species on transition metal (TM) surfaces [13–15]. Prior to its dissociation, CO₂ can exist in a bent state (activated state) on the catalyst surface [15, 16]. This activated state is the result of charge transferred from the metal catalyst to the CO₂ molecule, which in turn results in the elongation of the C=O bonds and decrease in the O=C=O bond angle (linear to bent mode) [17, 18]. Spectroscopic studies have been instrumental in our understanding of CO₂ activation by identifying the formation of activated CO₂ on Ni(100) and K-doped Rh(111) surfaces prior to its dissociation [15, 19]. In addition, theoretical investigations of CO₂ activation have been assessed on several metal and metal oxide catalysts [13, 14, 16, 20].

Focusing on CO₂ conversion to CH₃OH, CO₂ is in the syngas mixture (CO₂/CO/H₂) used for the industrial production of CH₃OH on Cu/ZnO/Al₂O₃ catalysts at moderate temperatures (473-573K) and high pressures (50 to 100 bar) [21]. Experimental and theoretical studies have shown that CO₂ serves as the primary carbon source for the industrial synthesis of CH₃OH [22, 23]. The active sites for CO₂ and CO hydrogenation on the industrial catalyst have been identified as a Cu stepped surface decorated with Zn atoms: a CuZn(211) surface [24]. CO and CO₂ hydrogenation intermediates were shown to exhibit increased adsorption strength and decreased barriers towards CH₃OH synthesis on CuZn(211) compared to the Cu(211) surface. The authors hypothesized that Zr, which has a similar oxophilicity to Zn can result in a similar adsorption behavior as observed with the decoration of Zn atoms on the surface of Cu(211) [24]. In addition, an experimental study by Yang et al. showed

higher conversion and selectivity for CH_3OH from the hydrogenation of CO_2 on ZrO_2 -doped Cu/ZnO catalysts compared to Cu/ZnO [25]. Thus, it appears that the incorporation of Zr into Cu-based catalysts results in generating more efficient catalysts for CO_2 conversion.

CuNi systems are another example of attractive catalysts for CH_3OH synthesis as experimental studies on Ni/Cu(100) surfaces have shown enhanced catalytic activity for CH_3OH synthesis compared to the monometallic Cu(100) surface [26, 27]. Additionally, a combined Density Functional Theory (DFT) and kinetic Monte Carlo study on the effects of metal doping (metal = Au, Pd, Rh, Pt, and Ni) of Cu(111) on CH_3OH synthesis found that the Ni/Cu(111) surface showed the highest rate for CH_3OH production compared to the other alloyed systems and the monometallic Cu(111) surface [28]. Temperature programmed desorption (TPD) experiments on a Ni film grown on a Cu(110) surface showed high rates of CO_2 chemisorption compared to the Cu(110) surface on which only physisorption was observed [29]. The ability of CuNi systems to adsorb CO_2 have been theoretically investigated on Ni-doped Cu_n ($n=1-12$) clusters [30]. The Ni-doped Cu_n systems chemisorbed CO_2 in a bent state, while the pure Cu_n clusters only weakly interacted with CO_2 . In these clusters the strong CO_2 adsorption was observed when CO_2 was in direct contact with the Ni atom of the cluster. CuNi NP interactions with CO_2 have also been studied on 55-atom NPs with Ni-doped and core-shell CuNi compositions [31]. In the doped system, a single Ni atom was located in the core, surrounded by 54 Cu atoms and in the core-shell system 13 Ni atoms were located in the core and 42 Cu atoms were on the shell. Only weak CO_2 adsorption was observed on these systems as further indicated by the C=O bond lengths and O=C=O bond angle of adsorbed CO_2 ($\sim 1.172 \text{ \AA}$ and $\sim 180^\circ$) remaining like that of gas phase CO_2 (1.162 \AA and 180°).

Overall, previous studies suggest the incorporation of Zr and Ni into Cu-based catalysts results in the generation of more useful catalysts for the chemical transformation of CO_2 compared to monometallic Cu catalysts. DFT calculations can be used to provide a thorough analysis of the structural, thermodynamic, and electronic properties of Cu-based NPs that could potentially lead to identifying novel, stable, and active nanocatalysts for the adsorption, activation and conversion of CO_2 into valuable chemicals and fuels.

1.2 CO₂ REDUCTION ON ELECTROCATALYSTS

CO₂ conversion through electrocatalytic means is an alternative and attractive route to mitigate elevated CO₂ emissions by sustainable conversion of CO₂ to useful chemicals and fuels [32–36]. Electrochemical conditions are advantageous for this reaction because applied potentials can be used to drive the reduction at ambient pressures and temperatures, and the electricity required to reduce CO₂ can be acquired from renewable resources such as wind and solar power [37–41]. Presently, the challenge with reducing CO₂ electrocatalytically is that it is not industrially feasible due to the highly reducing potentials required to obtain desired products such as hydrocarbons and CO [37, 42, 43]. Additionally, at these extreme potentials, there is low selectivity for desired products due to the competing H₂ evolution reaction [38, 44]. Therefore, there is continued interest in the design of active catalysts that promote CO₂ reduction at modest potentials while minimizing hydrogen evolution.

Experimental work by Hori et al. demonstrated that bulk Au electrodes can successfully reduce CO₂ to CO [43, 45]. Additional studies have shown that nanosized Au electrodes are more active than bulk Au electrodes [46–48]. The enhanced activity of Au NPs has been attributed to catalyst properties such as high surface area and increased presence of low-coordinated sites that strongly bind reaction intermediates [47, 49–51]. Mistry et al. investigated CO₂ reduction on Au NPs 1.1 nm to 7.7 nm in size [46]. The authors identified that NPs below 5 nm were significantly more active than bulk Au whereas, NPs larger than 5 nm were comparably active to bulk Au. The activity of the Au NPs less than 5 nm in size was attributed to the presence of low-coordinated sites such as corners and edges. Interestingly, the catalytically more active and smaller NPs (< 5 nm) were more selective towards H₂ [46]. Hall et al. showed that porous Au film thickness (ranging from 0.5 to 2.7 μ m) can also influence CO₂ reduction selectivity [52]. The authors observed a suppression in hydrogen evolution with increase in film thickness, leading to increased selectivity towards CO. Thus, in addition to the presence of low-coordinated sites, mass transport effects could also play a role in resulting activity and selectivity of Au NPs for the CO₂ reduction reaction.

In contrast to polydisperse Au NPs, atomically precise Au nanoclusters (NCs), stabilized by organic ligands, exhibit well-defined structure which make them attractive for catalytic

applications [53,54]. However, the presence of ligands can also limit the accessibility of reactants to Au sites resulting in reduced catalyst activity [55–57]. Despite this, Kauffman et al., has observed enhanced catalytic activity of ligand-protected NCs compared to unprotected NPs at reducing potentials as small as -0.193 V [48]. Specifically, the authors compared the activity of a fully ligand-protected $\text{Au}_{25}(\text{SC}_2\text{H}_4\text{Ph})_{18}^-$ NC, about 1 nm in size, to unprotected (metallic) 2 nm and 5 nm Au NPs, and bulk Au. Despite the small size of the $\text{Au}_{25}(\text{SC}_2\text{H}_4\text{Ph})_{18}^-$ NC, contrary to Mistry et al. [46], the NC was more selective towards CO than the NPs and bulk Au. In addition, the $\text{Au}_{25}(\text{SC}_2\text{H}_4\text{Ph})_{18}^-$ NC produced peak CO production at -1.0 V vs RHE, at a rate 7-700 times higher than on the NPs and bulk Au. This suggests that the ligands designed to stabilize these Au NCs have an effect in the selective reduction of CO_2 to CO. Despite the negative potentials applied, a retention of the optical spectra before and after CO_2 reduction suggests that the $\text{Au}_{25}(\text{SC}_2\text{H}_4\text{Ph})_{18}^-$ NC did not change size, and that the S-Au-S-Au-S bonding motif in the cluster shell was majorly retained. The potential scalability and long-term performance of electroreduction of CO_2 over the $\text{Au}_{25}(\text{SC}_2\text{H}_4\text{Ph})_{18}^-$ NC has also been investigated [58]. Under realistic on-demand catalyst usage, CO selectivities and Faradaic efficiencies greater than 90%, were achieved through both potentiostat-controlled and renewable solar powered electrolysis. Thus, these ligand-protected Au NCs appear to be attractive electrocatalysts for feasible conversion of CO_2 .

Theoretical methods combined with experiments can be used to provide atomic level insight into the catalyst properties that influence CO_2 reduction activity over Au_{25} NCs. For instance, Kauffman et al. assessed CO_2 reduction on fully ligand-protected $\text{Au}_{25}(\text{SR})_{18}^q$ NCs in three different charge states ($q = -1, 0, +1$) using DFT calculations and experiments, wherein thiolate ligands were simulated with methylthiols in calculations [59]. The negatively charged NC was able to produce more CO from CO_2 reduction than the neutral and positive NCs between -0.7 V and -1.3 V vs RHE. The activity of $\text{Au}_{25}(\text{SR})_{18}^-$ for CO_2 reduction was computationally attributed to the stabilization of co-adsorbed CO_2 and H^+ reactants more favorably than on $\text{Au}_{25}(\text{SCH}_3)_{18}^q$ ($q = 0, +1$). Such a stabilization is expected due to the electrostatic interactions between the negatively charged NC and the proton. The presence of ligand-removed NCs, due to the very negative potentials applied, was not

considered in this work, neither the detailed reaction path. In a latter study, Alfonso et al. used DFT to investigate CO₂ reduction to CO on fully ligand-protected Au₂₅(SCH₃)₁₈⁻ and partially ligand-removed Au₂₅(SCH₃)₁₇⁻ [60]. The authors identified that the COOH species, an important intermediate in CO₂ reduction, was more stabilized on Au₂₅(SCH₃)₁₇⁻ ($\Delta G[*\text{COOH}]$: 0.34 eV) than on Au₂₅(SCH₃)₁₈⁻ ($\Delta G[*\text{COOH}]$: 2.04 eV). The stabilization of the COOH intermediate, was attributed to its interaction with exposed Au atoms from the thiol ligand-removed site [60]. The investigation of ligand-removed Au₂₅(SCH₃)₁₇⁻ was supported using work by Wu et al. in which the authors observed an enhancement in CO conversion over the Au₂₅(SC₂H₄Ph)₁₈ NC when thiol-based ligands were removed from the NC [57].

Results to date illustrate that there is no consensus on the identity of active sites on ligand-protected Au nanocatalysts. Some studies have proposed that under reaction conditions these catalysts remain fully ligand-protected [48, 54, 59, 61, 62] while others have stated that some ligand removal is necessary for activity to be observed [55, 57, 63–68]. Additionally, there are competing claims on whether Au nanocatalysts are more selective towards CO [48, 58, 69] or H₂ [46, 70] under CO₂ reduction conditions. This lack of agreement on the selectivity of Au nanocatalysts, in addition to the elusive active sites under electrocatalytic conditions, make it very difficult to identify chemical strategies for the design and synthesis of thiolated Au NCs that efficiently reduce CO₂.

Although theoretical studies can give valuable insights into the reaction mechanisms and reveal active catalytic sites, there are presently very few studies that have investigated the CO₂ reduction behavior on these ligand-protected NCs [48, 59, 60, 63]. DFT can be used to systematically determine how the the NC charge state and ligand-removal concertedly influence the reaction energetics of the CO₂ reduction and H₂ evolution reactions. DFT calculations can elucidate the active sites on the NC catalyst surface for CO₂ reduction and provide insight into the mechanisms of their generation that would lead to the design of more efficient CO₂ electroreduction catalysts.

2.0 CO₂ ACTIVATION ON BIMETALLIC COPPER-NICKEL NANOPARTICLES

The content of this chapter is taken from Austin, N., Butina, B. and Mpourmpakis, G., "CO₂ Activation on Bimetallic CuNi Nanoparticles", *Prog. Nat. Sci.: Mater. Int.*, 26, 487-492 (2016) [71].

2.1 COMPUTATIONAL METHODS

In this work we use computational tools to investigate CO₂ adsorption and activation on CuNi bimetallic NPs of different compositional decorations and their monometallic counterparts. We used the BP86 functional [72, 73], the resolution of the identity(RI) approximation [74, 75], and the def2-SV(P) [76, 77] basis set as implemented in the TURBOMOLE 7.02 computational program package [78]. Dispersion corrections have been taken into account in the calculations using the D3 method [79, 80]. The total electronic energies of icosahedral 55-atom monometallic and bimetallic NPs composed of Cu and Ni were determined by geometry optimizations. Specifically, these structures include monometallic (Cu₅₅ and Ni₅₅), decorated (Cu₄₃Ni₁₂ and Cu₁₂Ni₄₃), and core-shell (Cu₄₂Ni₁₃ and Cu₁₃Ni₄₂) combinations of Cu and Ni atoms. Multiple spin states were considered in our calculations and the lowest in energy were selected for further analysis. Furthermore, all the optimized structures were verified as minima with frequency calculations (absence of any imaginary modes). The cohesive energy (binding energy per metal atom, BE/n) [81] was calculated using Equation 2.1:

$$\frac{BE}{n} = \frac{E_{Cu_{55-x}Ni_x} - (55-x)E_{Cu} - (x)E_{Ni}}{55} \quad (2.1)$$

where x is the number of Ni atoms in the NP ($x=0, 12, 13, 42, 43$, and 55) and $E_{Cu_{55-x}Ni_x}$, E_{Cu} , and E_{Ni} are the total energies of the $Cu_{55-x}Ni_x$ NPs, Cu atom, and Ni atom, respectively. Using Equation 2.2 we calculated the excess energy (E_{exc}) [82, 83], a descriptor for the stability of the bimetallic NPs relative to their monometallic counterparts:

$$E_{exc} = \frac{E_{Cu_{55-x}Ni_x} - \frac{55-x}{55}E_{Cu_{55}} - \frac{x}{55}E_{Ni_{55}}}{55} \quad (2.2)$$

where $E_{Cu_{55}}$ and $E_{Ni_{55}}$ are the total energies of the Cu_{55} and Ni_{55} NPs. The E_{exc} indicates if the formation of the bimetallic systems will be favorable (negative total energy) or unfavorable. Equation 2.3 was used to calculate CO_2 adsorption (binding energy, BE) on the metal NPs.

$$BE = E_{NP-CO_2} - E_{NP} - E_{CO_2} \quad (2.3)$$

Adsorption was assessed with CO_2 oriented towards one of the equivalent corner sites (coordination number 6, CN6) on the surface of the NPs, in two different adsorption configurations, horizontal and vertical to the NP surface. In the case of $Cu_{12}Ni_{43}$, CO_2 adsorption was also investigated with CO_2 oriented towards the edge site (CN8) of the NP where Ni atoms are located (vide-infra analysis). During CO_2 optimization, the coordinates of the NPs were kept frozen at their optimized positions and the CO_2 molecule was allowed to relax. The calculated adsorption states were further verified as minima with frequency calculations (absence of imaginary modes on CO_2). Natural bond orbital (NBO) analysis was used to calculate charge distribution on all the systems. Molecular orbital plots were visualized using TmoleX [84], a graphical user interface for TURBOMOLE.

2.2 RESULTS AND DISCUSSION

2.2.1 Structural and Electronic Properties of $Cu_{55-x}Ni_x$ Nanoparticles

The lowest energy structures of the six NPs studied in this work are shown in Figure 2.1. The icosahedral shape, which is the lowest energy structure for monometallic Cu_{55} and Ni_{55} [85],

was also maintained for the bimetallic systems. The conservation of the icosahedral geometry can be attributed to the similar atomic radius of Cu (1.28 Å) [86] and Ni (1.25 Å) [86] atoms. The calculated BE/n and E_{exc} of the systems are shown in Table 2.1. The BE/n trend from the largest (most negative value) to lowest value is as follows: $\text{Ni}_{55} > \text{Cu}_{12}\text{Ni}_{43} > \text{Cu}_{13}\text{Ni}_{42} > \text{Cu}_{42}\text{Ni}_{13} > \text{Cu}_{43}\text{Ni}_{12} > \text{Cu}_{55}$. Thus, we find that as the Ni fraction in $\text{Cu}_{55-x}\text{Ni}_x$ increases, the BE/n also increases. This observation agrees with the melting points of the metals, with Ni (1728 K) [86] having higher melting point than Cu (1358 K) [86], and as a result, the average bond strength of their alloys shows larger values with higher Ni content. Furthermore we found that the BE/n trend of the monometallics followed that of experimental bulk (Cu 3.49 eV/atom and Ni 4.44 eV/atom) [86], where in this case the more positive BE/n represents the more stable system. The E_{exc} trend describes the stability of the bimetallic NPs

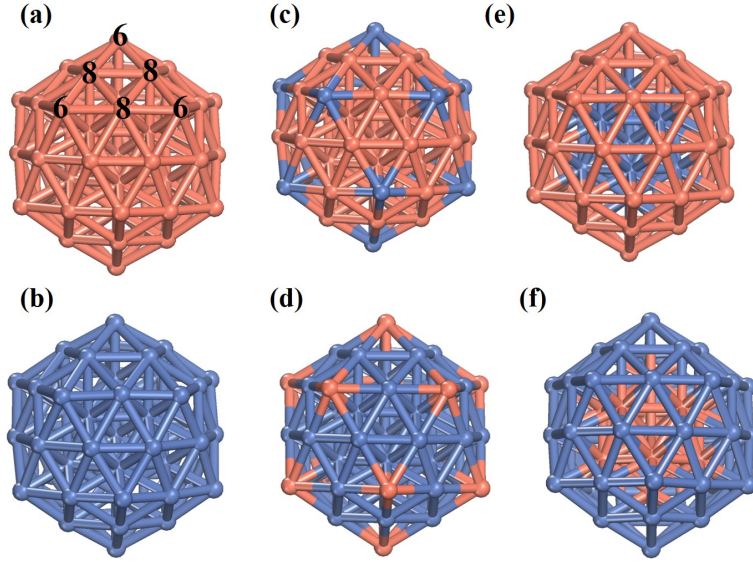


Figure 2.1: Optimized geometries of 55-atom NPs: monometallic (a) Cu_{55} and (b) Ni_{55} , decorated (c) $\text{Cu}_{43}\text{Ni}_{12}$ and (d) $\text{Cu}_{12}\text{Ni}_{43}$ NP with 12 heteroatoms located at the corner (CN6) sites of the NP, and core-shell (e) $\text{Cu}_{13}\text{Ni}_{42}$ and (f) $\text{Cu}_{42}\text{Ni}_{13}$ with 13 metal atoms located in the core and 42 heteroatoms in the shell. The equivalent CN6 and CN8 sites on the NPs are illustrated in (a). The Cu atoms are colored brown and the Ni blue.

relative to the monometallic parents. The E_{exc} trend from most stable to least stable is as follows: $\text{Cu}_{42}\text{Ni}_{13} > \text{Cu}_{12}\text{Ni}_{43} > \text{Cu}_{43}\text{Ni}_{12} > \text{Cu}_{13}\text{Ni}_{42}$. Overall we found that the core-

shell structure, $\text{Cu}_{42}\text{Ni}_{13}$, is the most energetically favorable formation for the bimetallic NPs. In theoretical work by Yang et al. the icosahedral $\text{Cu}_{42}\text{Ni}_{13}$ NP was also found to be energetically favorable [31]. The E_{exc} trends can be attributed to the surface energy (Cu 1170 ergs $\cdot\text{cm}^{-2}$ and Ni 2240 ergs $\cdot\text{cm}^{-2}$) [87] and bulk cohesive energy of monometallic Cu and Ni. The surface and cohesive energy values show that, in general, Cu prefers to reside on the surface and Ni prefers to be in the core of the NP. This core-shell preference has been shown to be present in nanoscale systems in the recent work by Wang et al. [88], calculating segregation energies of doped transition metal systems. In particular it was found that the Ni atom preferred to reside in the core than on the surface of a 55-atom cuboctahedral Cu_{54}Ni . Due to the energetic preference of Cu for the surface and Ni for the core of the NPs, we find that the core-shell $\text{Cu}_{42}\text{Ni}_{13}$ is more energetically favorable than the corresponding $\text{Cu}_{13}\text{Ni}_{42}$ NP, and the decorated $\text{Cu}_{12}\text{Ni}_{43}$ is more favorable than the corresponding $\text{Cu}_{43}\text{Ni}_{12}$ NP. Overall the results show that the most energetically favorable NPs have Cu (lower cohesive and surface energy) on the lowest coordinated, surface sites, and Ni (higher cohesive and surface energy) on the highest coordinated, bulk sites of the NP.

Table 2.1: Calculated BE/n and E_{exc} of the $\text{Cu}_{55-x}\text{Ni}_x$ NPs. The negative values indicate exothermicity.

	BE/n (eV/atom)	E_{exc} (eV/atom)
Cu_{55}	-3.266	-
Ni_{55}	-4.155	-
$\text{Cu}_{43}\text{Ni}_{12}$	-3.413	0.0560
$\text{Cu}_{12}\text{Ni}_{43}$	-3.980	-0.0218
$\text{Cu}_{42}\text{Ni}_{13}$	-3.535	-0.0692
$\text{Cu}_{13}\text{Ni}_{42}$	-3.849	0.113

2.2.2 CO_2 Adsorption on $\text{Cu}_{55-x}\text{Ni}_x$ Nanoparticles

Previous theoretical work on adsorption of small molecules, such as CO, on the surface of NPs showed that the stronger adsorption was observed on surface NP sites exhibiting low CNs (e.g. corners, edges) [89]. In turn, in the CO_2 adsorption studies [13, 15, 18], strong adsorption of the CO_2 molecule on the metal surface results to its activation. Thus, we

primarily investigated the CO₂ adsorption on the corner (CN6) site (the lowest coordinated site in our systems) of the Cu_{55-x}Ni_x NPs. As shown in Figure 2.1(a), since all the CN6 sites are equivalent (same with the CN8 edge sites) due to the Ih symmetry of the NPs, we studied the CO₂ adsorption on one of these sites. The lowest energy structures for CO₂ adsorption are shown in Figure 2.2. We calculated the adsorption energy for two orientations of the CO₂ molecule: (i) horizontal CO₂, where the C atom of CO₂ was interacting with the corner site and (ii) vertical CO₂, where an O atom of CO₂ was interacting with the corner site. The horizontal orientation was found to be the most preferred adsorption configuration of CO₂ on all the metal NPs in our study. Consistent with literature [13, 16–18, 20], we found that the systems that activate CO₂ always show strong adsorption and charge transfer from the metal NP to CO₂, which results in a linear to bent transition of the CO₂ molecule, and elongation of the C=O bonds. Specifically from Table 2.2 we found strong CO₂ adsorption on Ni₅₅, Cu₄₃Ni₁₂, Cu₁₂Ni₄₃, and Cu₁₃Ni₄₂ and weak adsorption on Cu₅₅ and Cu₄₂Ni₁₃. In addition, as shown in Table 2.2 the systems with strong CO₂ adsorption had more than -0.6|e| transferred to the CO₂ molecule while in the weakly adsorbed systems there was no significant charge transfer. The geometric properties of gas phase CO₂ and CO₂ interacting with the metal NPs are also shown in Table 2.2. Compared to gas phase (non-interacting) CO₂, the O1-C-O2 angle of the strongly adsorbed CO₂ decreased (<150°) and the C=O bonds elongated (>1.2 Å) which indicates the activation of the CO₂ molecule. In the weakly adsorbed systems the bond angles and bond distances of CO₂ remained similar to gas phase CO₂. The deviations of average bond lengths (black squares) and angles (blue circles) between adsorbed and gas phase CO₂ as a function of CO₂ BE are illustrated in Figure 2.3. It is clear that both the CO₂ bond distances and angles are affected in a similar way with the CO₂ BE. To demonstrate this interdependence between the CO₂ angle and bond distance deviation (from CO₂ gas) we plotted these geometric properties in the inset of Figure 2.3 and we observe a linear trend. Overall, Figure 2.3 shows that the bending of the CO₂ molecule and the elongation of its bonds show the same behavior and they are enhanced (increased activation) with stronger adsorption on the NP surface. In Figure 2.4 we demonstrate the CO₂ BE as a function of the total charge transferred to the CO₂ molecule. We notice that bimetallic systems with Ni atoms being on the surface of the NP transfer significant charge to CO₂. In turn, this results

in strong CO_2 adsorption, while for the $\text{Cu}_{42}\text{Ni}_{13}$ system, where Ni is at the core of the NP and inaccessible to CO_2 , significant charge transfer is not observed, resulting to weak CO_2 adsorption. It should be noticed that so far, our discussion on the activation of the CO_2 molecule is entirely focused on the structural and electronic observations made on the CO_2 molecule itself and not involving properties of the nanoparticle.

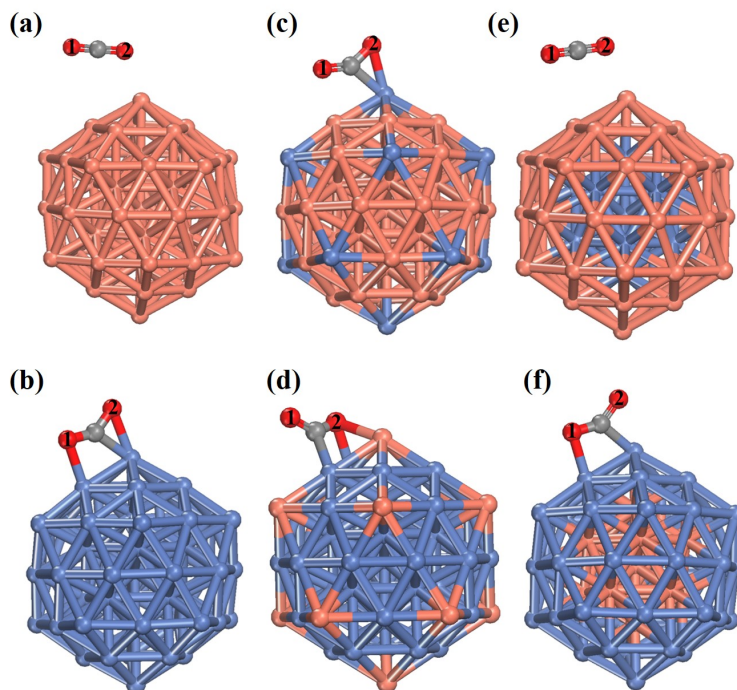


Figure 2.2: CO_2 adsorption on the (a-b) monometallic, (c-d) decorated, and (e-f) core-shell Cu-Ni NPs. The color code is as depicted in Figure 1 with the addition of CO_2 (C colored grey and oxygen colored red).

Table 2.2: CO₂ binding energies on the NPs, total charge (NBO) transferred to CO₂, and geometric properties of gas phase CO₂ (non-interacting) and CO₂ interacting with the NPs. Binding energies are in eVs. Bond lengths of C-O1 and C-O2 are in angstroms, Å. Bond angle of O1-C-O2 are in degrees, °.

	BE (eV)	e	C-O1 (Å)	C-O2 (Å)	O1-C-O2 (°)
CO ₂ (gas)	--	--	1.175	1.175	180.000
Cu ₅₅	-0.368	0.00825	1.169	1.183	179.406
Ni ₅₅	-0.665	-0.658	1.243	1.238	141.610
Cu ₄₃ Ni ₁₂	-0.919	-0.604	1.245	1.230	143.465
Cu ₁₂ Ni ₄₃	-0.803	-0.810	1.216	1.309	132.070
Cu ₄₂ Ni ₁₃	-0.391	0.00207	1.183	1.170	178.989
Cu ₁₃ Ni ₄₂	-0.891	-0.652	1.231	1.255	140.476

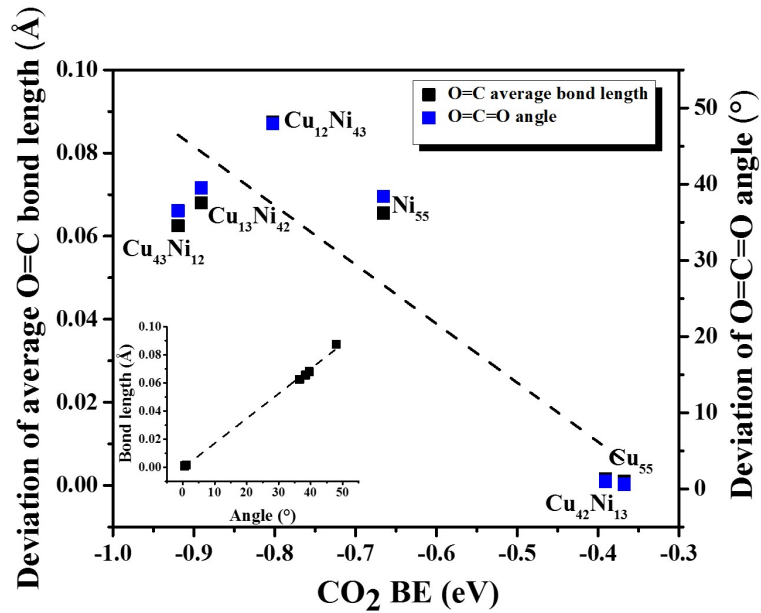


Figure 2.3: Deviation of adsorbed CO₂ average C=O bond length (left ordinate) and O=C=O bond angle (right ordinate) from gas phase CO₂ as functions of CO₂ BE. The inset figure at the bottom left shows a linear relationship between average C=O bond length and O=C=O bond angle.

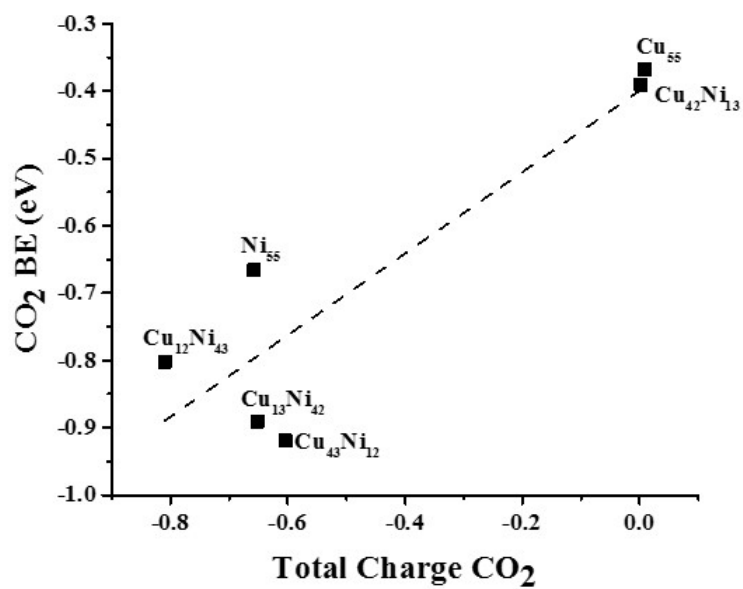


Figure 2.4: CO₂ BE as a function of total charge on CO₂. The dashed black line in serves as a guide to the eye.

2.2.3 Descriptors for CO₂ Adsorption on Cu_{55-x}Ni_x Nanoparticles

From a catalyst design perspective, we need to identify a property of the metal NPs that could correlate with the observed activation. As a result, we made an effort to rationalize the CO₂ adsorption behavior using the d-band center (d_C) model by Hammer and Norskov [90, 91]. We calculated the local d_C on a single metal site of CO₂ adsorption (Cu or Ni) on the Cu_{55-x}Ni_x NPs. In Figure 2.5, the CO₂ adsorption values are plotted as a function of the local site d_C of the NPs. The observed linear trend indicates that there is an increase in CO₂ adsorption with decrease in the d_C , shifting towards the energy level of the CO₂ Lowest Unoccupied Molecular Orbital (LUMO), which is located at -0.35 eV (blue dashed line). The Cu₄₃Ni₁₂ showed the highest local d_C and strongest BE, while the Cu₅₅ showed the lowest d_C and the weakest BE. Notice that the Cu₄₃Ni₁₂ positions its local-site d_C at the energy level of CO₂ LUMO, showing the strongest adsorption. It is important to note that for Cu₁₂Ni₄₃ we did not observe strong adsorption when CO₂ interacted directly with the corner Cu sites of the NP. Even the presence of Ni atoms in the neighboring positions (edge sites), did not enhance CO₂ adsorption on the corner site compared to the Cu₅₅ system. However, since surface Ni is responsible for enhancing the CO₂ adsorption (compare CO₂ adsorption on Cu₅₅ vs. Cu₄₃Ni₁₂), we calculated the adsorption energy of CO₂ on an edge site (CN8) of the Cu₁₂Ni₄₃, where the Ni atoms are located. In this case we observe a strong CO₂ adsorption on Cu₁₂Ni₄₃ which was 0.4 eV lower in energy than the case where the CO₂ interacted with the Cu atoms of the NP. This shows that the presence of Ni atoms on the surface of the NP significantly enhances CO₂ adsorption.

To further rationalize the effect of the metals d-orbital density and the charge transfer on the CO₂ activation, we plotted the Highest Occupied Molecular Orbitals (HOMO) of Cu₅₅, Ni₅₅, Cu₄₃Ni₁₂ and Cu₁₂Ni₄₃ NPs as shown in Figure 2.6. These are the monometallic parents (Cu₅₅ and Ni₅₅), the bimetallic showing the strongest CO₂ adsorption (Cu₄₃Ni₁₂) among the NPs studied, and the bimetallic NP that shows strong CO₂ adsorption and favorable E_{exc} (Cu₁₂Ni₄₃). It has been shown that charge transfer from the metal to CO₂ occurs when the d-orbitals of the metal NP significantly interacts with the $2\pi_u$ antibonding orbital (LUMO) of CO₂ [17]. In Figure 2.6 we assessed the presence of d-orbital character in the HOMO

orbitals of the aforementioned NPs. Figures 2.6(a) and 2.6(b) illustrate the HOMO orbital distribution on monometallic Cu₅₅ and Ni₅₅ respectively. From the shape of the orbitals we observe primarily s-orbital localization on Cu₅₅, while there is mainly d-orbital localization on Ni₅₅. By quantifying the orbital character through the atomic orbital coefficients of the HOMO, we found that there is a much greater fraction of d-orbital character in the HOMO of Ni₅₅, which shows strong binding to CO₂ than in Cu₅₅, which weakly adsorbs CO₂. The bimetallic systems Cu₄₃Ni₁₂ and Cu₁₂Ni₄₃ show high fractions d-orbital character with Cu₁₂Ni₄₃ having the highest. Cu₄₃Ni₁₂ has a lower fraction of d-orbital character than Cu₁₂Ni₄₃ because of the lower fraction of Ni atoms in Cu₄₃Ni₁₂ than in Cu₁₂Ni₄₃. It should also be noticed that the d-orbitals are localized on surface CN6 atoms of the Cu₄₃Ni₁₂, whereas, on the CN8 of the Cu₁₂Ni₄₃. In other words, the surface sites where the Ni atoms are located show strong CO₂ adsorption. Overall we demonstrate that adding Ni on the surface of Cu NPs increases the presence of d-orbital character, which in turn, results in a favorable interaction of the NP with CO₂, and subsequent activation of the CO₂ molecule. Although we found that Cu₄₃Ni₁₂ binds CO₂ the strongest, the most promising NP from our study is the Cu₁₂Ni₄₃ because in addition to the strong CO₂ adsorption (BE = -0.8 eV) and activation, it shows favorable energetics for its synthesis ($E_{\text{exc}} = -0.02$ eV/atom). This study highlights that in bimetallic catalyst design it is important to achieve a balance between catalyst stability (the most stable CuNi NPs prefer Cu to be on the surface) and interaction strength of the catalyst with adsorbates (CO₂ strongly adsorbs and is being activated on surface Ni). Although computational studies like this one identify bimetallic NPs that are stable and promising for CO₂ activation, there is a synthetic challenge in forming nanostructures with (in-silico) predefined architecture. Recent experimental advances on the controlled synthesis of bimetallic NPs with atomic precision can pave the way towards achieving this goal [92,93].

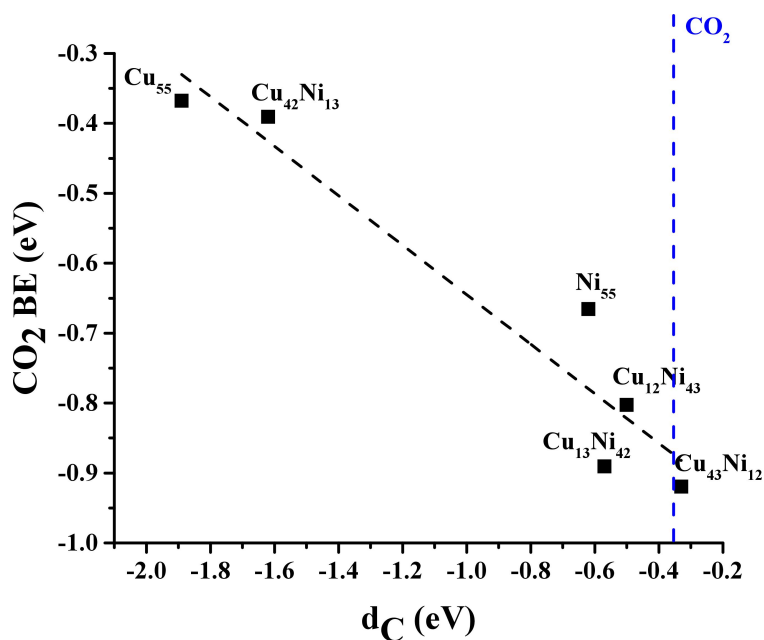


Figure 2.5: CO_2 BE as a function of local d_C of the $Cu_{55-x}Ni_x$ NPs. The dashed black line serves as a guide to the eye. In (b) the vertical blue line represents the LUMO orbital energy of the CO_2 molecule.

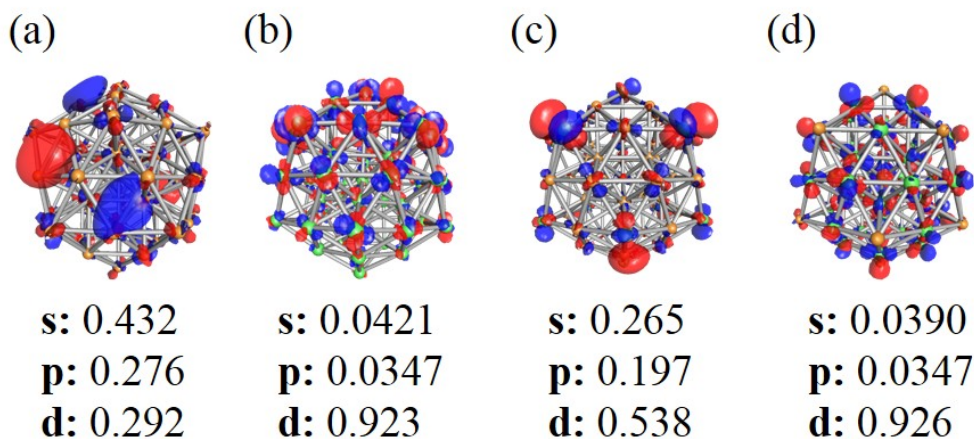


Figure 2.6: Visual representation of the HOMO orbitals and fractional distribution of the HOMO orbital character of the (a) Cu_{55} , (b) Ni_{55} , (c) $Cu_{43}Ni_{12}$, (d) $Cu_{12}Ni_{43}$ NPs.

2.3 CONCLUSIONS

In summary, we performed a DFT investigation on the structural, electronic and CO₂ adsorption properties of Cu_{55-x}Ni_x (x=0, 12, 13, 42, 43, and 55) NPs with a monometallic, core-shell, and decorated distribution of Cu and Ni atoms. We found that the BE/n of the bimetallic systems was a linear combination of the BE/n of the monometallic systems. We also calculated the excess energy (E_{exc}) of the bimetallic NPs with respect to the monometallic NPs and showed that the formation of decorated Cu₁₂Ni₄₃ and core-shell Cu₄₂Ni₁₃ NPs were energetically favorable, while the formation of core-shell Cu₁₃Ni₄₂ and decorated Cu₄₃Ni₁₂ were less favorable. These trends rationalize the preference of Cu to be located at the surface of the NPs rather than Ni. CO₂ adsorption calculations revealed weak interaction (physisorption) with the monometallic Cu₅₅ and core-shell Cu₄₂Ni₁₃, while the monometallic Ni₅₅, decorated Cu₁₂Ni₄₃ and Cu₄₃Ni₁₂, and core-shell Cu₁₃Ni₄₂ chemisorbed CO₂. In the chemisorbed cases we found strong adsorption of CO₂ on the corner sites of all NPs except Cu₁₂Ni₄₃ where strong CO₂ adsorption was found on the edge sites. The sites of strong adsorption on the NPs were always surface sites which were occupied by Ni atoms. Thus, the location of Ni on the NP plays an important role in the resulting adsorption behavior. The chemisorption behavior on the NPs was attributed to charge transferred from the metal NPs to CO₂ which led to the activation of the molecule. Additionally, we calculated the local-site d-band center (d_C) and we found a linear relationship between the d_C and CO₂ adsorption energy. The sites of strong adsorption localize HOMO orbitals with increased d-character. Overall this study demonstrates that the presence of surface Ni on CuNi bimetallic NPs can significantly enhance CO₂ adsorption, resulting in the activation of the CO₂ molecule. Furthermore, among the different nanostructures in this study we identified the Cu₁₂Ni₄₃, which can be potentially experimentally synthesized and activate CO₂ for dissociation and hydrogenation reactions due to its exothermic E_{exc} and strong adsorption behavior towards CO₂, respectively.

3.0 CO₂ ACTIVATION ON BIMETALLIC COPPER-ZIRCONIUM NANOPARTICLES

The content of this chapter is taken from Austin, N., Ye, J. and Mpourmpakis, G., "CO₂ on Cu-based Zr-decorated nanoparticles", *Catal. Sci. Technol.*, 7, 2245-2251 (2017) [94].

3.1 COMPUTATIONAL METHODS

In this work we use electronic structure calculations to examine the adsorption, activation, and reaction of CO₂ on 55-atom Cu NPs, with select surface Cu atoms being replaced by Zr atoms to generate Zr-decorated Cu NPs. All DFT calculations in this work were performed using the Quickstep program in the computational package, CP2K [95]. The calculations implemented the revised PBE (revPBE) functional [96] and the double- ζ plus polarization (DZVP) basis set [97] in combination with the Goedecker, Teter, and Hutter (GTH) pseudopotentials [98] with a 400 Ry cutoff. Grimme's DFT-D3 method [80] was used to account for dispersion interactions. Icosahedral 55-atom Cu NPs decorated with Zr atoms, Cu_{55-x}Zr_x (x=0, 1, 2, 4, 6, 8, 10, 12), with and without adsorbed CO₂ were optimized in nonperiodic 30 x 30 x 30 Å³ cubic cells until forces were less than 0.02 eV/Å. Optimized structures were verified as ground states with frequency calculations (absence of imaginary modes). Equation 3.1 was used to determine the core or shell preference of Zr in the Cu₅₄Zr NP. This preference is defined as the segregation energy (SE) of a single heteroatom (Zr) from the core to the surface of the host NP (Cu), where negative values indicate Zr preference for the surface.

$$SE = E(Cu_{54}Zr(surface)) - E(Cu_{54}Zr(core)) \quad (3.1)$$

Where $E(\text{Cu}_{54}\text{Zr}(\text{surface}))$ is the total electronic energy of the fully optimized Cu_{54}Zr NP in which one Cu atom is replaced by one Zr atom on the surface of Cu_{55} , and $E(\text{Cu}_{54}\text{Zr}(\text{core}))$ is the corresponding electronic energy for the core atom replacement. As shown in Figure 3.1 there are two distinct surface sites on the NP: coordination number (CN) 6, which is a corner site, and CN8, which is an edge site. The Zr atom in $\text{Cu}_{54}\text{Zr}(\text{core})$ is placed in the very central core atom of the NP which is a CN12 site. Equation 3.2 was used to calculate CO_2 adsorption (binding energy, BE) on the $\text{Cu}_{55-x}\text{Zr}_x$ NPs

$$BE = E_{NP_CO_2} - E_{NP} - E_{CO_2} \quad (3.2)$$

Where $E_{NP_CO_2}$, E_{NP} , and E_{CO_2} are the total energies of NP with adsorbed CO_2 , the isolated NP, and isolated CO_2 molecule, respectively. For all CO_2 adsorption cases, we considered parallel and perpendicular adsorption configurations (see Figure A1 of Appendix A.1 for illustrations of the adsorption configurations considered).

The climbing image nudged elastic band (CI-NEB) method [99] was used to identify potential barriers towards CO_2 activation on the NPs. Transition states determined from the CI-NEB calculations were further verified by frequency calculations which identified a single imaginary mode along the reaction coordinate. The convergence criterion for the maximum force was set to 0.1 eV/Å. Bader [100] charge analysis was further employed to quantify the charge transferred from the NPs to the CO_2 molecule.

3.2 RESULTS AND DISCUSSION

3.2.1 Zr Doping of Cu Nanoparticles

The thermodynamic preference for the surface enrichment of metal A over metal B in an AB alloy can be determined using the segregation energy (SE) of a single impurity (heteroatom) in a host system [88, 101]. In order to determine the SE using Equation 3.1, we placed a Zr atom on three sites of the NP as shown in Figure 3.1. Specifically, we replaced one Cu atom in the 55-atom Cu NP at the core, edge, and corner sites, with CNs 12, 8, and 6,

respectively. We identified that Zr prefers to reside on the surface of the NP as indicated by the negative SE values for the CN6 and CN8 Zr-decorated structures (compared to the energy of the central core position) shown below the NPs in Figure 3.1. Additionally, we determined that the CN6 site with a SE of -1.88 eV is the most preferred surface site for Zr to reside compared to CN8 which has a SE of -1.78 eV. The preference of Zr on the NP surface can be attributed to the larger atomic radius of Zr (1.60 Å) [86] compared to that of Cu (1.28 Å) [86]; Zr resides on the surface to minimize strain effects on the NP. Our calculated SE preference for Zr on the Cu NP surface agrees with the determined SE preference for Zr on the surface of Cu(111) [101].

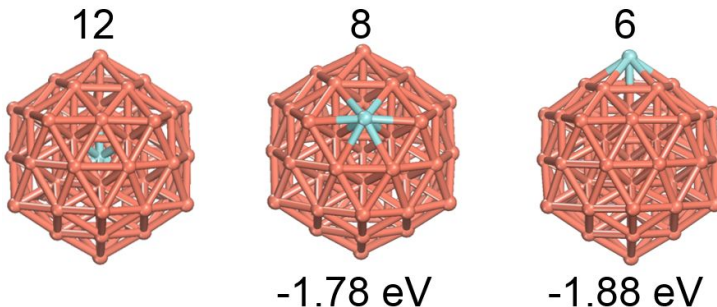


Figure 3.1: 55-atom Cu NP decorated with Zr at the three coordination sites (CN = 6, 8, 12) listed above the NP. The SE values for Zr residing on the CN8 and CN6 sites of the NP are listed below the NP. The Cu atoms are colored brown and the Zr atoms are in light blue.

3.2.2 CO₂ Adsorption and Activation on Cu₅₄Zr and Cu₅₅ Nanoparticles

CO₂ can interact with TM systems in a physisorbed state, where it retains the geometric properties of gas phase CO₂, and in a chemisorbed state, where it becomes bent (activated) [16, 18, 71]. We performed geometry optimizations of CO₂ adsorbed on Cu₅₄Zr starting with CO₂ at a physisorbed (~ 3.5 Å) and chemisorbed distance (~ 2.0 Å) from the NP surface. The most preferential adsorption site we found in both states was CO₂ interacting parallel to the edge of the Cu₅₄Zr NP near the Zr atom (see Figure 3.2(a)). The physisorption and chemisorption energies were calculated to be -0.13 and -1.29 eV, respectively. The physisorbed state retained the geometric properties of gas phase CO₂ (average C=O bond

length: 1.18 Å and O=C=O bond angle: 179.3°) while the chemisorbed state significantly deviated from gas phase CO₂ (average C=O bond length: 1.29 Å and O=C=O bond angle: 126.5°). We also assessed the transition from the physisorbed to chemisorbed state to identify any potential barriers towards activation given the enhanced thermodynamic stability of CO₂. As shown in Figure 3.2(a), the physisorbed and chemisorbed structures served as inputs to a CI-NEB calculation, with 6-8 replicas, which revealed that CO₂ activation on Cu₅₄Zr NP is barrierless. In the absence of surface Zr, the adsorption of CO₂ in an activated state on the Cu₅₅ NP was found to be +0.45 eV which is unfavorable compared to the weak physisorption of CO₂ on Cu₅₅ (-0.059 eV). Weak adsorption of CO₂ on monometallic Cu surfaces has also been observed in previous experimental and theoretical studies [13, 16, 29]. Figure 3.2(b) shows that the transition from physisorbed CO₂ to the activated state of CO₂ is barrierless but endothermic. These results indicate that surface Zr on Cu NPs can be an active site for CO₂ adsorption and activation, whereas, surface Cu sites are not.

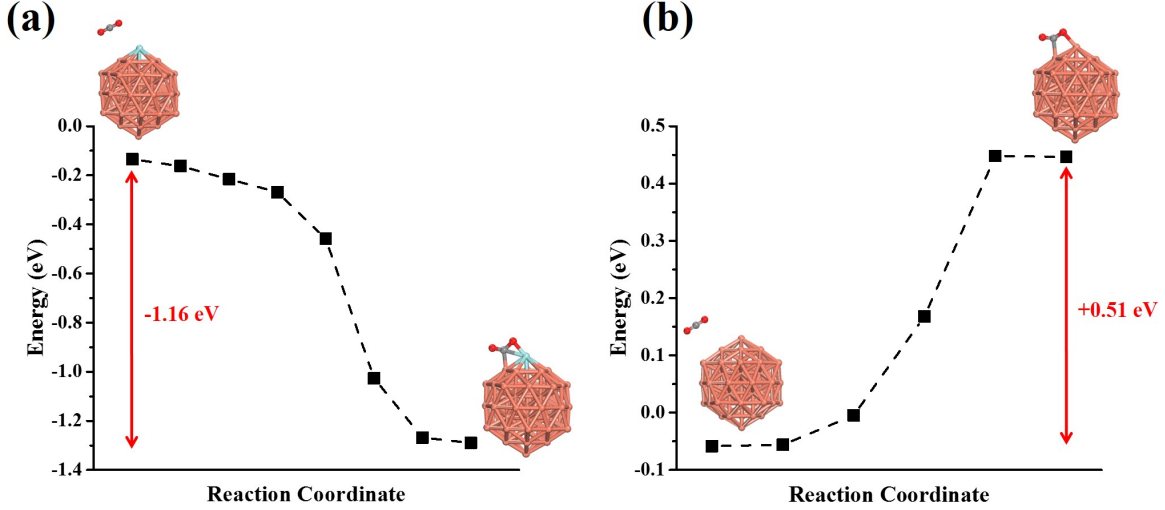


Figure 3.2: CI-NEB calculations for the physisorbed to activated state of CO_2 on the (a) Cu_{54}Zr and (b) Cu_{55} NP. The values in red in (a) and (b) is the change in energy (ΔE) from the physisorbed to activated state of CO_2 ($\Delta E = E_{\text{activated}} - E_{\text{physisorbed}}$). The negative (red) value in (a) represents an exothermic step, whereas, the positive value in (b) represents an endothermic step. The color code on the structure is as in Figure 3.1 with the addition of C and O (from CO_2) colored grey and red, respectively.

3.2.3 CO_2 Adsorption and Activation on $\text{Cu}_{55-x}\text{Zr}_x$ ($x = 2, 4, 6, 8, 10, 12$) Nanoparticles

Following the observed adsorption and activation of CO_2 on the Cu_{54}Zr NP we investigated the CO_2 adsorption behavior on CuZr NPs with an increasing surface fraction of Zr atoms. We generated the CuZr NPs by systematically replacing Cu with Zr at all CN6 sites of the 55-atom icosahedral NP. We selected CN6 as the site for Zr doping based on our SE analysis which showed that Zr preferred to reside on the CN6 site of the Cu_{54}Zr NP. As shown in Figure 3.3(a) we gradually replaced 2-12 Cu atoms with Zr atoms in the NP in a symmetric manner to investigate the effects of increasing concentration of Zr in a Cu-based NP. CO_2 hydrogenation studies on Cu/ ZrO_2 have shown that Cu sites are favorable for H_2 dissociation and ZrO_2 is necessary for the activation of CO_2 [102, 103]. Thus, from

a catalyst design perspective, our model for Zr doping of the Cu NP with the Zr atoms being at maximum separation, maximizes the available Zr sites for CO₂ activation, while keeping neighboring Cu sites for H₂ dissociation. We do note however that there may be more stable forms of Cu_{55-x}Zr_x decoration other than decoration on the CN6 sites (see Figure A2 and Figure A3 of Appendix A.1 for the case of Cu₅₃Zr₂ and corresponding CO₂ binding, respectively). Figure 3.3(b) illustrates CO₂ BE as a function of surface fraction of Zr in the 55-atom NP. The observed CO₂ BE does not change significantly with the addition of 2-6 Zr atoms on the NP surface (BE range: -1.39 eV to -1.42 eV). In contrast, we observe a significant enhancement in the CO₂ BE with increasing Zr content when 8-12 Zr atoms are added on the NP surface (BE range: -1.52 eV to -1.80 eV). As shown in Figure 3.4(a), for each Cu_{55-x}Zr_x NP we observed activation of CO₂ by elongation of the C=O bonds and decrease in the O=C=O angle. Figure 3.4(a) also demonstrates that the largest deviation of the geometrical features of CO₂ compared to the gas phase occurs on the NPs exhibiting the strongest BEs. The activation of CO₂ has been attributed to the charge transferred from the d-orbitals of the TM system to the anti-bonding orbitals of the CO₂ molecule. [17, 18]. Therefore in Figure 3.4(b) we plotted the CO₂ BE as a function of the total charge located on the activated CO₂ bound to the Zr-decorated Cu NPs. We found that for each NP case more than 0.9 |e| charge was transferred to the CO₂ molecule from the NP. It should be noted that to verify that the activated (chemisorbed) state of CO₂ remains barrierless on the NPs with the high Zr content, we performed CI-NEB calculations on the Cu₄₃Zr₁₂ NP, which has the highest composition of Zr in our study and found that indeed, the CO₂ chemisorption remains barrierless and exothermic.

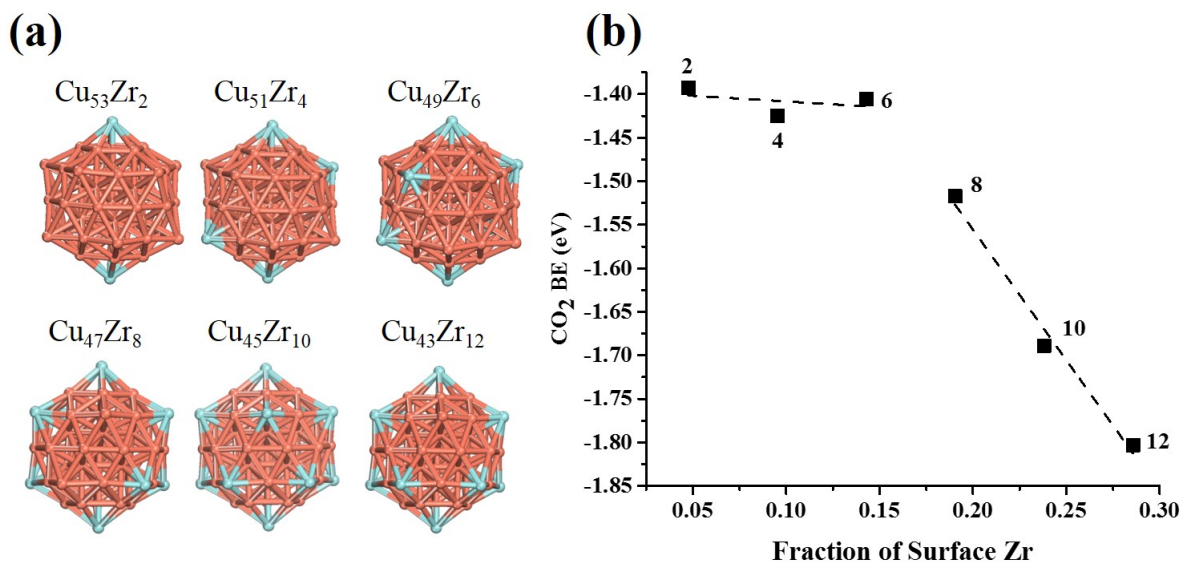


Figure 3.3: (a) Cu_{55-x}Zr_x ($x = 2, 4, 6, 8, 10, 12$) decoration on the 55-atom NPs. (b) CO₂ adsorption as a function of surface fraction of Zr on the Cu_{55-x}Zr_x NPs. The dashed lines serve as a guide to the eye. The color code on the structure is as in Figure 3.1.

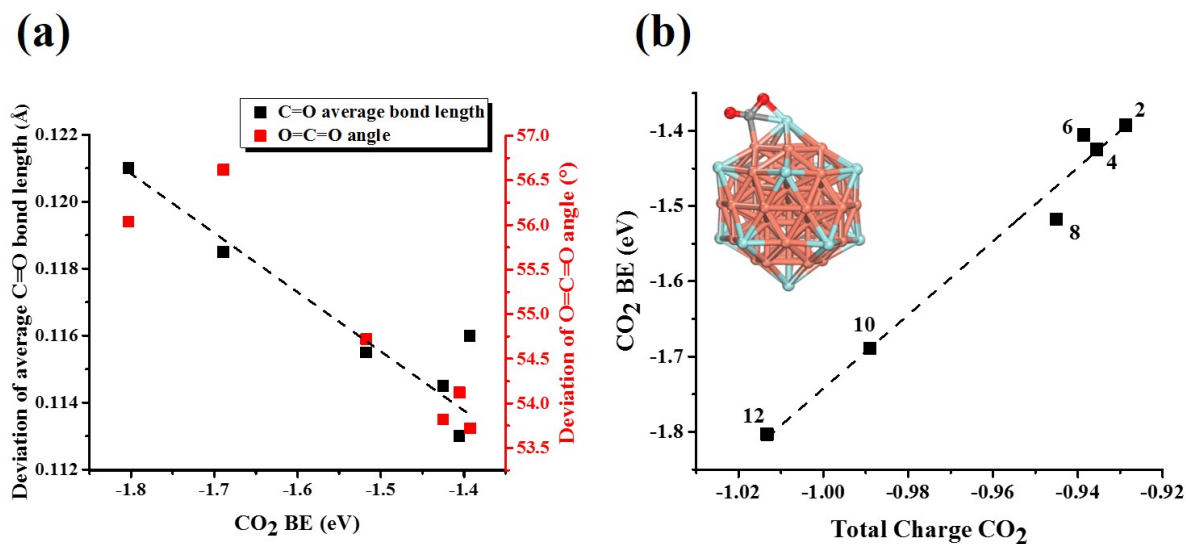


Figure 3.4: (a) Deviation of adsorbed CO₂ geometric properties from gas phase CO₂ (b) CO₂ BE as a function of total charge on CO₂ for each Cu_{55-x}Zr_x ($x = 2, 4, 6, 8, 10, 12$) NP. The inset figure shows chemisorbed CO₂ on Cu₄₃Zr₁₂. The dashed lines in (a) and (b) serve as a guide to the eye. The color code on the structure is as in Figure 3.2.

3.2.4 Electronic Properties of CuZr Nanoparticles

An understanding of the underlying catalyst properties responsible for CO₂ activation is important for developing catalysts with enhanced CO₂ conversion activity. Therefore, we assessed the d-band center (d_C) and ionization potential (IP) as NP descriptors for our observed adsorption trends. Hammer and Norkov have shown that the d_C of a metal catalyst can be correlated with the adsorbate BE [90,91]. In addition, we have previously shown that the IP of a catalyst (or equivalently work function) is a good descriptor for adsorption [104] especially for systems involving charge transfer (case of CO₂ interaction as shown in Figure 3.4(b)). In Figure 3.5(a) we identified a correlation between the CO₂ BE and the localized d_C of the Zr atom interacting with CO₂ for each Cu_{55-x}Zr_x NP (see inset in Figure 3.4(b)). In Figure A4 of Appendix A.1, we illustrate the PDOS used to determine the d_C for each NP. It is important to note that for Cu_{55-x}Zr_x NPs with 2-6 Zr atoms on the surface we observe a negligible change in the d_C of the site, which in turn results to a practically unaffected CO₂ BE as shown in Figure 3.3(a). Conversely, for Cu_{55-x}Zr_x NPs with 8-12 Zr atoms the d_C varied more significantly and in turn, there were significant variations in the CO₂ BE. We also observe from Figure 3.5(a) that as we increase the Zr composition, the d_C shifts closer to the fermi level (i.e. a shift closer to zero in 3.5(a)) which is responsible for the increasing adsorption strength of CO₂. Overall, the local d_C appears to be a good descriptor for the observed CO₂ adsorption behavior. In Figure 3.5(b) we present the relationship between the CO₂ BE and the IP of the NP. As the IP decreases we observe a stronger CO₂ BE. Given that the IP represents the ability of the NP to donate electrons, we believe that the IP is the catalyst property responsible for the degree of charge transfer to the CO₂ molecule resulting in the activation of the molecule. In addition, Figure 3.5(b) demonstrates a way to tune CO₂ chemisorption: increasing the surface Zr composition (experimental parameter) decreases the IP of the NP, and in turn, the CO₂ adsorption becomes stronger. As shown in Figure A4 of Appendix A.1, increasing the Zr composition, shifts the HOMO (Highest Occupied Molecular Orbital) towards the LUMO of CO₂ (Lowest Unoccupied Molecular Orbital) and closer to the Fermi level of the NP. This in turn, results to decreasing the catalyst IP and increasing the interaction energy of CO₂.

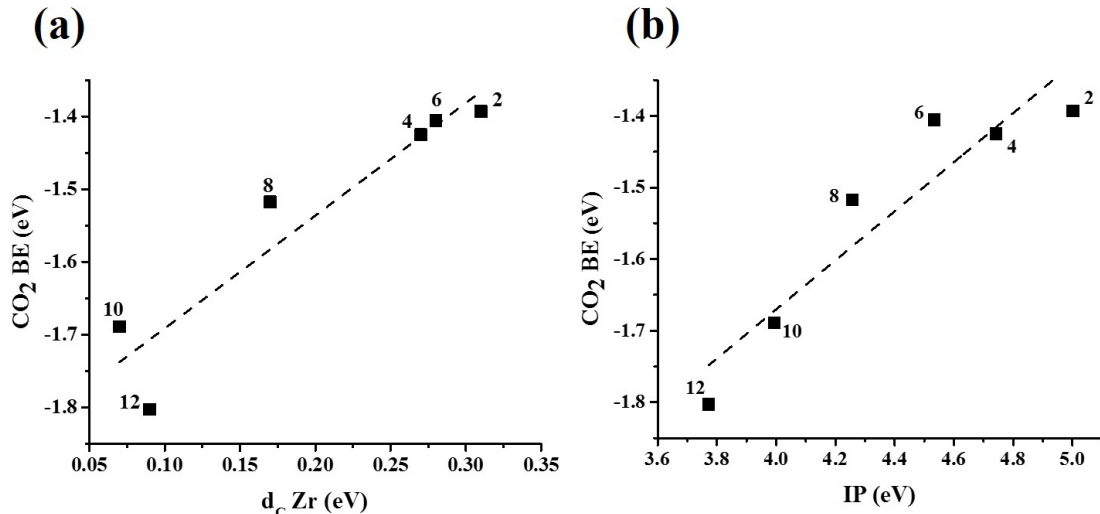


Figure 3.5: (a) Cu_{55-x}Zr_x ($x = 2, 4, 6, 8, 10, 12$) decoration on the 55-atom NPs. The color code is as in Figure 1. (b) CO₂ adsorption as a function of surface fraction of Zr on the Cu_{55-x}Zr_x NPs. The dashed lines serve as a guide to the eye. The color code on the structure is as in Figure 3.2.

3.2.5 CO₂ Dissociation to CO on Cu₅₄Zr and Cu₅₅ Nanoparticles

The facile chemisorption of CO₂ on the Cu_{55-x}Zr_x NPs indicates that the NPs could serve as favorable CO₂ reduction catalysts compared to monometallic Cu NPs alone. As a preliminary analysis, for our ongoing CO₂ reaction studies, we compared the CO₂ dissociation barriers on Cu₅₄Zr and Cu₅₅ and found that Cu₅₄Zr dissociated CO₂ at a significantly lower barrier than Cu₅₅. Specifically, Figure 3.6(a) illustrates the dissociation of CO₂ into adsorbed CO and O on both the Cu₅₅ and Cu₅₄Zr NPs relative to the isolated CO₂ molecule and the NP. We found that the transition state (TS) energy value and bond length for C-O bond breaking on Cu₅₅ and Cu₅₄Zr are 0.93 eV and 1.87 Å, and 0.20 eV and 1.73 Å, respectively. The second TS in the Cu₅₄Zr pathway, which has a small barrier of 0.05 eV represents the diffusion of O from a top site to a slightly more stable hollow site configuration. The Cu₅₄Zr system exhibits the second TS because the direct transition of O into the hollow site from CO₂ dissociation through a single TS (as was for Cu₅₅) was not favorable. The corresponding structures for each state of the energy diagram are shown in Figure 3.6(b). The facile dissociation of CO₂

observed in this study and the oxophilic nature of Zr suggests that under reaction conditions CuZr NPs can be oxidized as is supported by previous studies [102, 105–107]. Thus in our recent study we investigated CO₂ adsorption behavior on Cu₅₄ZrO_x NPs [108]. Notably, we observed barrierless chemisorption of CO₂ on all of the oxidized Cu₅₄Zr systems studied (see supporting information Figures A5 and A6 in Appendix A.1). This is an important observation as it shows that surface Zr sites on doped Cu NPs can adsorb and activate CO₂ regardless of their degree of oxidation [108].

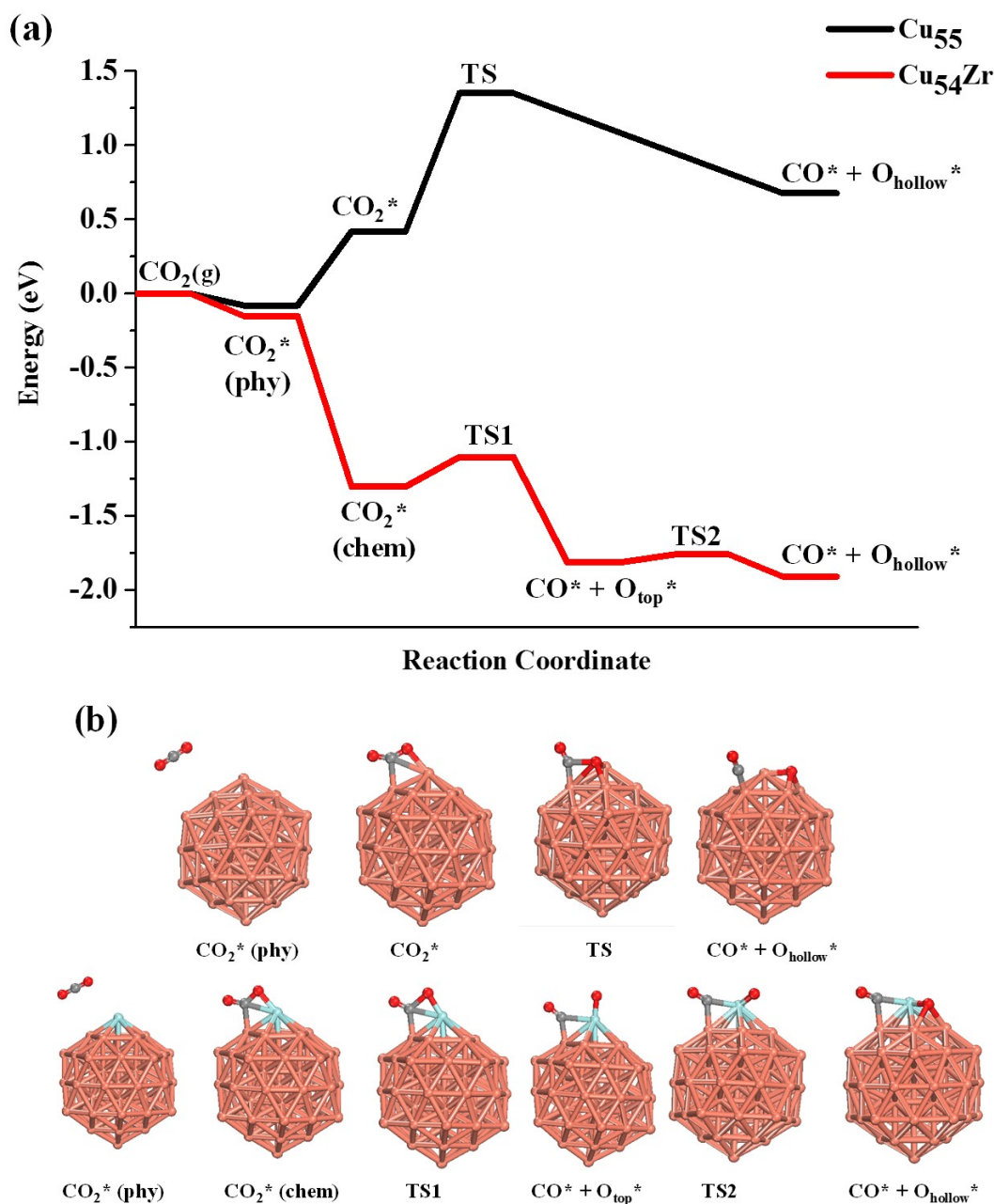


Figure 3.6: (a) CO_2 dissociation reaction path on Cu_{55} (black line) and Cu_{54}Zr (red line). For Cu_{55} , TS represents breaking of a C-O bond, with a C-O bond length of 1.87 Å. For Cu_{54}Zr , TS1 represents the breaking of a C-O bond, with a C-O bond length of 1.73 Å and TS2 represents the diffusion of O from a top site to hollow site configuration. (b) Optimized structures for the CO_2 dissociation to CO and O on the Cu_{55} (top row) and Cu_{54}Zr (bottom row) NPs. The color code on the structure is as in Figure 3.2.

3.2.6 Experimental Observations for CO₂ Adsorption on CuZr Catalysts

In our recent work we qualitatively verified the computational observation that the presence of surface Zr on Cu NPs results in the strong adsorption of CO₂ [108]. We synthesized CuZr bimetallic catalysts and evaluated their CO₂ adsorption by using TPD. The catalysts were prepared by a simple wet impregnation approach and were characterized thoroughly to confirm the presence of a mixed CuZrO₃ phase, pure Cu, and ZrO₂ phases on the catalyst surface [108]. The presence of both phase-separated pure Cu and ZrO₂ particles, was as expected from the tendency of Cu and Zr to phase segregate (see segregation energy values in Figure 3.1). TPD analysis verified that pure Cu only physisorbed CO₂ while both bimetallic CuZr and pure ZrO₂ showed strong adsorption of CO₂ as indicated by desorption peaks (see supporting information Figure A7 in Appendix A.1 for the TPD analysis). Thus our experimental results qualitatively confirmed the major computational results that is: i) Cu NPs do not adsorb CO₂, ii) Cu and Zr metals have a strong tendency to segregate, iii) Zr has high propensity to oxidize, and iv) even if the Zr sites are oxidized (to form a mixed copper zirconium oxide), they are still able to adsorb CO₂ effectively.

3.3 CONCLUSIONS

In summary, we investigated the electronic and CO₂ adsorption properties of Cu_{55-x}Zr_x (x=0, 1, 2, 4, 6, 8, 10, 12) NPs. These Cu-based NPs, which consist of 55-atoms, have a decorated distribution of Zr atoms on the surface. Segregation energy analysis identified that Zr prefers to reside on the surface of the NPs, especially at the lower coordinated sites. Adsorption calculations revealed that the Zr site at the NP surface is the most favorable site for CO₂ adsorption. The CO₂ binding energy varies slightly when the decorated Zr increases from 2 to 6 atoms on the Cu NP surface. However, a significant increase in the CO₂ binding energy was observed when we decorated 8-12 Zr atoms on the Cu NP surface. Furthermore, the elongation of C=O bond lengths and the bending of O=C=O bond angles were observed for all CO₂ adsorption cases on the Cu_{55-x}Zr_x NPs, which indicates that CO₂ is activated

when it adsorbs on $\text{Cu}_{55-x}\text{Zr}_x$ NPs (compared to the linear gaseous CO_2). We found the chemisorption of CO_2 on the Zr-decorated Cu NPs to be barrierless and exothermic, while it is endothermic on monometallic Cu_{55} NP. This chemisorption behavior was attributed to a strong charge transfer from the CuZr NPs to CO_2 , resulting in the activation of CO_2 . We further identified two descriptors for CO_2 adsorption: the d-band center (d_C) localized on the Zr atom interacting with CO_2 and the ionization potential (IP) of the whole NP. Both descriptors correlate with the CO_2 adsorption energies. The latter descriptor is significant since it can be experimentally measured and, as we demonstrate in this work, it can be tuned with the Zr content (composition variation) on the NP surface.

To assess the effectiveness of CuZr NPs as catalysts for CO_2 conversion, we investigated the CO_2 dissociation to CO and O on Cu_{54}Zr and Cu_{55} . We found that the barriers towards CO_2 dissociation on the Cu_{54}Zr NP were much lower than that on the Cu_{55} NP. Our work demonstrates that Zr-decorated Cu-based NPs enhance the adsorption and activation of CO_2 , which in turn, results in lower barriers towards the dissociation of CO_2 . As a result of the highly exothermic adsorption of CO_2 on Zr-doped Cu NPs relative to monometallic Cu and the oxophilicity of Zr, we further investigated CO_2 adsorption on oxidized Cu-Zr NPs. We observed chemisorption of CO_2 on the oxidized Zr sites on each NP investigated.

These computational observations were confirmed qualitatively by performing experiments on a mixed CuZr catalyst. The catalysts showed the presence of both pure (i.e., phase-segregated) Cu and ZrO_2 phases (in agreement with the computational prediction that Cu and Zr have a high segregation energy), as well as a mixed CuZrO_3 phase. Although pure Cu was not able to adsorb any CO_2 , the mixed CuZrO_3 phase showed strong CO_2 adsorption.

Overall, our computational and experimental results suggest that Zr-doped Cu NPs can adsorb and activate CO_2 strongly, even if the surface Zr sites become oxidized. The resulting bimetallic system could be a promising material for CO_2 utilization by hydrogenation.

4.0 INFLUENCE OF ATOMIC-LEVEL GOLD CATALYST MORPHOLOGY ON CO₂ ELECTROREDUCTION

The content of this chapter is taken from Zhao, S., Austin, N., Li, M., Song, Y., House, S. D., Bernhard, S., Yang, J. C., Mpourmpakis, G., and Jin, R., "Influence of Atomic-Level Morphology on Catalysis: The Case of Sphere and Rod-Like Gold Nanoclusters for CO₂ Electroreduction", *ACS Catal.*, 8, 4996-5001 (2018) [63]

4.1 COMPUTATIONAL METHODS

In this work, we investigated two types of Au nanoclusters (NCs) of identical size (i.e., 25 atoms) but distinctly different atomic packing structures or morphology (i.e., Au₂₅ nanosphere and Au₂₅ nanorod) as electrocatalysts for CO₂ reduction. DFT calculations were performed using the PBE [73] functional and the double- ζ plus polarization (DZVP) basis set [97] with a 500 Ry cutoff in combination with the Goedecker, Teter, and Hutter (GTH) pseudopotentials [98] as implemented in the computational package CP2K [95]. The thiol ligands in the nanosphere and nanorod clusters, were simulated with methylthiols resulting to Au₂₅(SCH₃)₁₈ and Au₂₅Cl₂(SCH₃)₅(PH₃)₁₀ NCs. This R-group simplification of the ligands is a commonly used approach to reduce computational cost, without affecting the interfacial bond strength (i.e. Au-SR) of the NCs [48, 59, 60, 64, 109]. The nanosphere and nanorod exist in -1 and +2 charge states, respectively. To simulate realistic systems, counterions were added to the NCs which results in overall neutral systems. Specifically, one NH₄⁺ ion was added to the nanosphere and two SbF₆⁻ ions were added to the nanorod. Bader [100] charge analysis was used to verify the charge state on the NCs in the presence of the coun-

terions. The initial geometries of the NCs in the presence of the counterions were generated from experimentally-derived crystallographic data of the NCs. The geometries were optimized until forces were less than $0.02 \text{ eV}/\text{\AA}^{-1}$. The ligand(s) considered for removal from the nanosphere is SCH_3 and from the nanorod are SCH_3 , $-\text{Cl}$, and PH_3 . The free energies for ligand removal and COOH^* formation were calculated using thermodynamic methods where the zero-point energy (ZPE), heat capacity (CP), and entropic (TS) terms were added to the electronic energy (E) as shown in Equation 4.1:

$$\Delta G = \Delta E + \Delta \text{ZPE} + \int CPdT - T\Delta S \quad (4.1)$$

In addition, the computational hydrogen electrode model (CHE) [42] was applied to treat the free energy of a proton(H^+)–electron(e^-) pair in electrochemical reduction reactions as equivalent to the free energy of one-half of molecular hydrogen. Thus the free energy of the pair with consideration of an applied potential (U) is defined as $G(\text{H}^+ + \text{e}^-) = G(\frac{1}{2} \text{H}_2) - n\text{eU}$ where n is the number of electrons transferred and e is the electronic charge. In this study we report energetics at 0 V vs RHE (U = 0, no applied potential). Thus, the ΔG for ligand removal of $-\text{SCH}_3$ and $-\text{Cl}$, treated as a reduction reaction using hydrogen, is as shown in the following Equation 4.2 example for $-\text{SCH}_3$ removal from the nanosphere (with counterions):

$$\begin{aligned} \Delta G_{\text{thiol-removal}} = & G[(\text{Au}_{25}(\text{SCH}_3)_{17}\text{NH}_4)^0] + G[\text{HSCH}_3] - G[(\text{Au}_{25}(\text{SCH}_3)_{18}\text{NH}_4)^0] \\ & - \frac{1}{2}G[\text{H}_2] \end{aligned} \quad (4.2)$$

Where $G[(\text{Au}_{25}(\text{SCH}_3)_{17}\text{NH}_4)^0]$, $G[\text{HSCH}_3]$, $G[(\text{Au}_{25}(\text{SCH}_3)_{18}\text{NH}_4)^0]$, and $G[\text{H}_2]$ are the gas phase free energies of the isolated nanosphere with a removed thiol, the HSCH_3 molecule, the fully-protected nanosphere, and the H_2 molecule, respectively. Removal of a PH_3 ligand from the nanorod (with counterions) was calculated as a ligand desorption (non-reduction) step using the following Equation 4.3:

$$\Delta G_{\text{PH}_3\text{-removal}} = G[\text{Au}_{25}\text{Cl}_2(\text{SCH}_3)_5(\text{PH}_3)_9] + G[\text{PH}_3] - G[\text{Au}_{25}\text{Cl}_2(\text{SCH}_3)_5(\text{PH}_3)_{10}] \quad (4.3)$$

Where $G[\text{Au}]$ are the gas phase free energies of the isolated nanorod with a PH_3 ligand removed, the PH_3 molecule, and the fully protected nanorod, respectively. The ΔG for $^*\text{COOH}$ formation ($\Delta G^*\text{COOH}$) on each NC of interest is calculated using Equation 4.4 as shown:

$$\Delta G^*_{\text{COOH}} = G[^*\text{COOH}] + G[\text{NC}] - \frac{1}{2}G[\text{H}_2] - G[\text{CO}_2] \quad (4.4)$$

Where $G[^*\text{COOH}]$, $G[\text{NC}]$, $G[\text{H}_2]$, $G[\text{CO}_2]$ are the gas phase free energies of the isolated $^*\text{COOH}$ adsorbed on a NC, the bare NC, the H_2 molecule, and the CO_2 molecule, respectively.

4.2 RESULTS AND DISCUSSION

4.2.1 Experimental Observations for CO_2 Reduction on Au_{25} Nanoclusters

The Au_{25} nanosphere and nanorod clusters were synthesized following reported protocols [110, 111] in the lab of Professor Rongchao Jin at Carnegie Mellon University. The Au_{25} NCs, supported by carbon black, were then evaluated for the electrocatalytic reduction of CO_2 . Higher catalytic performance was observed on the Au_{25} nanosphere compared to the Au_{25} nanorod as shown by analysis of the total current density (see Figure A8(a) of Appendix A.2). In Figure A8(b) of Appendix A.2, the better catalytic performance of the Au_{25} nanosphere was more distinct under high voltages where the Au_{25} nanosphere cluster exhibited a CO Faradiac Efficiency (FE) of 73.7% at -0.57 V, which is 1.63 times higher than that of the Au_{25} nanorod cluster (CO FE \sim 28.0%). At -0.67 V, a CO FE difference of 30% (i.e., 69.3% vs 39.7%) between the two clusters was also prominent. Catalyst selectivity in CO_2 reduction is crucial in practical applications due to the competing water reduction generating H_2 as well as the formation of CO_2 reduction products other than CO. As for the distribution of carbon-containing products, Au_{25} NCs exhibit excellent selectivity for the CO product [48] than other carbon-containing products. Only CO and H_2 were detected in these experiments, which is consistent with previous results [48, 58, 59]. Analysis of FE showed that both the nanosphere and nanorod were more selective towards CO than H_2 .

However, in Figure A8(b-c) of Appendix A.2, the Au₂₅ nanosphere exhibited a much higher CO selectivity with smaller FE toward H₂ (H₂ FE 24.9%) compared to the Au₂₅ nanorod (H₂ FE 41.2%) around -1.0 V. The Au₂₅ nanosphere also formed CO at higher rate than that of the Au₂₅ nanorod (see Figure A8(d) in Appendix A.2). Thus the larger FE for CO as well as higher CO formation rates over Au₂₅ nanosphere consistently demonstrated its higher catalytic performance for CO₂ reduction compared to the Au₂₅ nanorod.

4.2.2 Computational Analysis of CO₂ Reduction on Au₂₅ Nanoclusters

Our experiments clearly show the Au₂₅ nanosphere possesses higher CO₂ reduction activity and selectivity for CO product than the Au₂₅ nanorod. To further understand their different catalytic behavior, DFT calculations were performed. In recent work, Alfonso et al. assessed CO₂ reduction to CO on the fully protected Au₂₅(SCH₃)₁₈⁻ spherical NC as well as the partially ligand-removed Au₂₅(SCH₃)₁₇⁻ spherical NC [60]. They determined that the Au₂₅(SCH₃)₁₇⁻ species would promote CO₂ reduction more favorably, compared to the Au₂₅(SCH₃)₁₈⁻, because the Au₂₅(SCH₃)₁₇⁻ species stabilized the *COOH intermediate on the exposed Au atoms of the ligand-removed site. Therefore, the removal of one ligand from the NCs is critical for generating active sites for CO₂ reduction. As a result, herein we first compare the ability of the two NCs to partially release ligands and expose Au active sites, from the different sites of the nanosphere and nanorod.

Figure 4.1(a) illustrates the two NCs and sites from which ligands are removed. For the nanosphere, removal of a single SCH₃ is considered, whereas for the nanorod, removal of SCH₃, -Cl, or PH₃ is considered. The SCH₃ and -Cl ligands are removed as reduction reaction steps using hydrogen while the removal of PH₃ is considered as a desorption step. Figure 4.1(b) shows the ΔG values for removing different ligands from the nanosphere and nanorod at 0 V vs reversible hydrogen electrode (RHE). Of note, the removal of the PH₃ is not included in Figure 4.1(b) due to different pathways (reduction versus desorption steps). The desorption of PH₃ from the nanorod is calculated to be ΔG: 0.54 eV which is equivalent to the removal of -Cl (green line, ΔG: 0.54 eV) as shown in Figure 4.1(b). For the nanorod, the removal of PH₃ and -Cl is more favorable than the removal of SCH₃ (blue line, ΔG:

0.95 eV). Comparing ligand removal from the nanorod to the nanosphere, the removal of SCH₃ is less endergonic from the nanosphere (red line, ΔG : 0.49 eV) than from the nanorod. It is observed that ligand removal from the nanosphere is slightly more favored than the ligand removal from the nanorod. Therefore, the ligand removal to release active sites on the nanosphere cluster is more energetically favorable than the nanorod cluster.

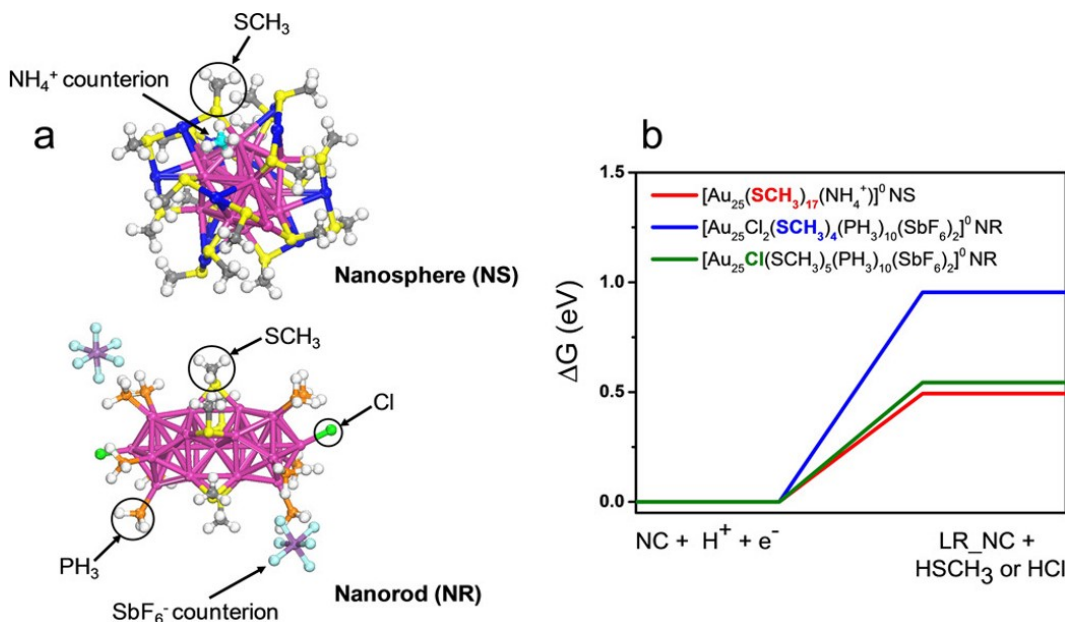


Figure 4.1: (a) Structures for the nanorod and the nanosphere in the presence of the NH₄⁺ and SbF₆⁻ counterions, respectively. Au atoms are shown in pink, S atoms shown in yellow, C atoms shown in grey, H atoms shown in white, N atoms shown in bright blue, Sb shown in purple, and F shown in light blue. The circled regions on the NCs demonstrate sites of ligand removal on the nanosphere (-SCH₃) and nanorod (SCH₃, -Cl, and PH₃) (b) ΔG values for ligand removal (in eV) from the NCs at 0 V vs RHE, where LR_NC represents "ligand-removed nanocluster", NS is nanosphere, and NR is nanorod. The blue and green lines represent removing a SCH₃ and -Cl from the nanorod with SbF₆⁻ counterions, respectively and the red line represents removing SCH₃ from the nanosphere with a NH₄⁺ counterion. All ligand removal steps are treated as electrochemical reduction steps.

After the ligand removal, gold active sites on the nanosphere and nanorod are revealed for CO₂ reduction catalysis. We then calculated the energetics for CO₂ reduction to CO at 0 V vs RHE on the ligand-removed (i.e., active sites) of the NCs. The formation of *COOH (ΔG_{*COOH}) has been shown to be an important intermediate in CO₂ reduction to CO on Au [46, 47, 60]. Figure 4.2 illustrates that *COOH is more stabilized on the Au₂₅(SCH₃)₁₇NH₄ (SCH₃ removed) nanosphere (0.43 eV) than on any of the ligand-removed systems of the nanorod (ΔG_{*COOH}), SCH₃ removed: 0.65 eV, -Cl removed: 0.56 eV, and PH₃ removed: 1.15 eV). Illustrations of the adsorbed *COOH and *CO structures are provided in Figures A9 and A10 of Appendix A.2, respectively. It should be noted that even though PH₃ and -Cl can be removed from the nanorod at a comparative ΔG to SCH₃ removal from the nanosphere, the resulted active species do not stabilize *COOH comparatively as shown in Figure 4.2. Therefore, the energetically favorable removal of SCH₃ from the nanosphere to release active sites as well as the stabilization of *COOH over the obtained Au₂₅(SCH₃)₁₇ species contribute to the higher catalytic performance of the Au₂₅ nanosphere over the Au₂₅ nanorod.

Kauffman et al. previously investigated CO₂ reduction on the Au₂₅(SCH₃)₁₈^q nanosphere in three charge states (q = +1, 0, -1) [59]. The negatively charged Au NC was found to promote CO₂ reduction more significantly, compared to the neutral and positively charged NCs, by stabilizing the reaction intermediates. To verify the role of NCs charge on CO₂ reduction, we performed Bader charge analysis calculations and determined that, in the presence of counterions, the nanosphere remained negatively charged (q = -0.77), whereas the nanorod positively charged (q = +1.94). Thus, the negative charge that the nanosphere possesses contributes to its higher activity in CO₂ reduction observed in experiments compared to the nanorod. Thus, overall, the negative charge and the favorable exposure of an active site on the nanosphere stabilize the important *COOH intermediate, which, in turn, contribute to enhanced activity of the nanosphere than the nanorod. Although we have not investigated multiple ligand removal steps from the surface of the NCs, in the Supporting Information we report a preliminary analysis on removing 1 and 2 additional ligands from the NCs (see Figure A11 of Appendix A.2) and find that additional ligand removal remains endothermic, but still probable under the experimentally applied potentials.

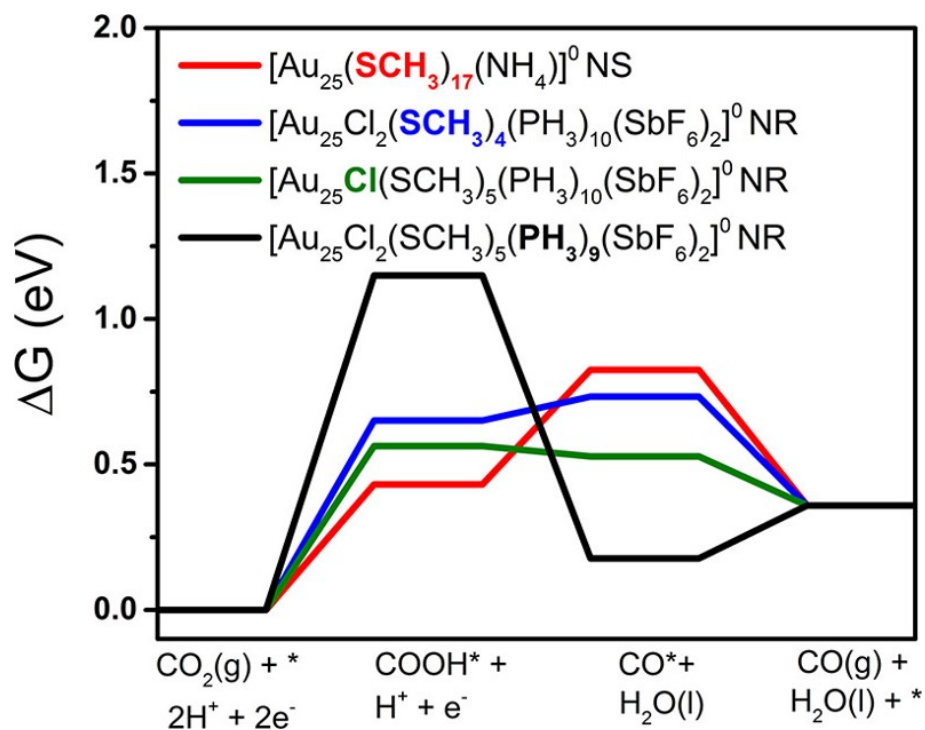


Figure 4.2: Free energy diagrams (ΔG) for CO_2 reduction to CO on the ligand-removed NCs at 0 V vs RHE. The black, blue, green, and red lines represent CO_2 reduction to CO on the nanorod with PH_3 removed, the nanorod with SCH_3 removed, the nanorod with $-\text{Cl}$ removed, and on the nanosphere with SCH_3 removed, respectively.

4.3 CONCLUSIONS

In this combined experimental and theoretical study we have investigated the atomic-level morphology effect of Au₂₅ NCs (sphere vs rod) as electrocatalysts for CO₂ reduction. The distinctly different atomic-level morphology and charge states render the Au₂₅ nanosphere more active for CO₂ reduction than the Au₂₅ nanorod. At -0.67 V, the nanosphere cluster exhibits a higher FE (69.3% for CO) than that of the nanorod cluster (39.7%). We have further performed DFT calculations based on their X-ray crystallographic structures and obtained mechanistic insights for the observed difference in catalytic performance. It is revealed that the negative charge state of the nanosphere as well as the energetically favorable removal of -SCH₃ from the nanosphere to expose active sites contribute to the higher catalytic features due to the stabilization of the important *COOH intermediate. This work explicitly demonstrates that the atomic-level morphology and electronic properties can greatly influence the catalytic performance; thus, the attainment of atomic structures of NCs is of critical importance in order to elucidate the fundamentals of catalytic reactions. The distinct morphology dependence of NCs and the obtained mechanistic insights are expected to provide some guidelines for future design of advanced catalysts for CO₂ reduction.

5.0 ELUCIDATING THE ACTIVE SITES FOR CO₂ ELECTROREDUCTION ON LIGAND-PROTECTED GOLD NANOCLUSTERS

The content of this chapter is taken from Austin, N., Zhao, S., McKone, J. R., and Mpourmpakis, "Elucidating the Active Sites for CO₂ Electroreduction on Ligand-protected Au₂₅ Nanoclusters", *Catal. Sci. Technol.*,(2018). Accepted, DOI: 10.1039/C8CY01099D.

5.1 COMPUTATIONAL METHODS

Using computational tools, we investigated the electrochemical reduction of CO₂ and the competing H₂ evolution reaction on ligand-protected Au₂₅ nanoclusters (NCs) of different charge states. DFT calculations were performed using the PBE [73] functional and the double- ζ plus polarization (DZVP) basis set [97] with a 500 Ry cutoff in combination with the Goedecker, Teter, and Hutter (GTH) pseudopotentials [98] as implemented in the computational package CP2K [95]. This combination of DFT parameters (functional, pseudopotentials, and basis set) has been successfully used to investigate reaction energetics on Au-based catalysts [112–116]. The initial geometries of the NCs were generated from experimentally-derived crystallographic data of the Au₂₅(SC₂H₄)₁₈[−] [117]. The ligands of the Au₂₅ NC were represented by methylthiolate groups (-SCH₃) generating the Au₂₅(SCH₃)₁₈ NC. Simplification of the ligands, from -SC₂H₄Ph to -SCH₃, is a typical approach used to reduce computational cost while maintaining the structural integrity of the NCs [48, 59, 60, 64, 109]. As shown in Figure 5.1, the Au₂₅(SCH₃)₁₈^q NC is composed of a Au₁₃ icosahedral core protected by a shell network of six Au₂(SCH₃)₃ units. The geometries of the NCs were op-

timized in a $30 \times 30 \times 30 \text{ \AA}^3$ non-periodic cell until the forces were less than 0.02 eV/\AA . All systems with an even number of electrons had a singlet multiplicity and all systems with an odd number of electrons in this study had a doublet multiplicity (see Table A1 in Appendix A.3 for more details). The energetics for ligand removal, CO_2 reduction, and H_2 evolution were calculated using thermodynamic methods where the zero-point energy (ZPE), heat capacity (CP), and entropic (TS) terms were added to the electronic energy (E) as follows: $\Delta G = \Delta E + \Delta \text{ZPE} + \int \text{CP dT} - T\Delta S$. Additionally, the computational hydrogen electrode model (CHE) [42, 118] was applied to represent the free energy of a proton (H^+) and electron (e^-) pair in reduction reactions and thereby, calibrate the calculated free energy on an electrochemical scale. Thus, the total free energy for a proton-electron pair where an applied potential (U) is defined as $G(\text{H}^+ + \text{e}^-) = G(\frac{1}{2}\text{H}_2) - neU$ where n is the number of electrons transferred and e is the electronic charge. Gas phase corrections as calculated by Peterson et al., were also applied to the electronic energies of the gaseous molecules [42]. For the free energies of the adsorbates the vibrational components of the heat capacity and entropic terms were considered. The vibrational modes of the adsorbates were determined by keeping the optimized NC fixed and computing the frequencies of the adsorbate within the harmonic oscillator approximation. This approach has been successfully applied using DFT in electrocatalysis [49, 60, 119, 120] including to the $\text{Au}_{25}(\text{SCH}_3)_{18}$ NC. The computationally predicted limiting potential (U_L) [42, 121] was calculated as the applied potential required for the rate determining step, to become thermoneutral ($\Delta G = 0$).

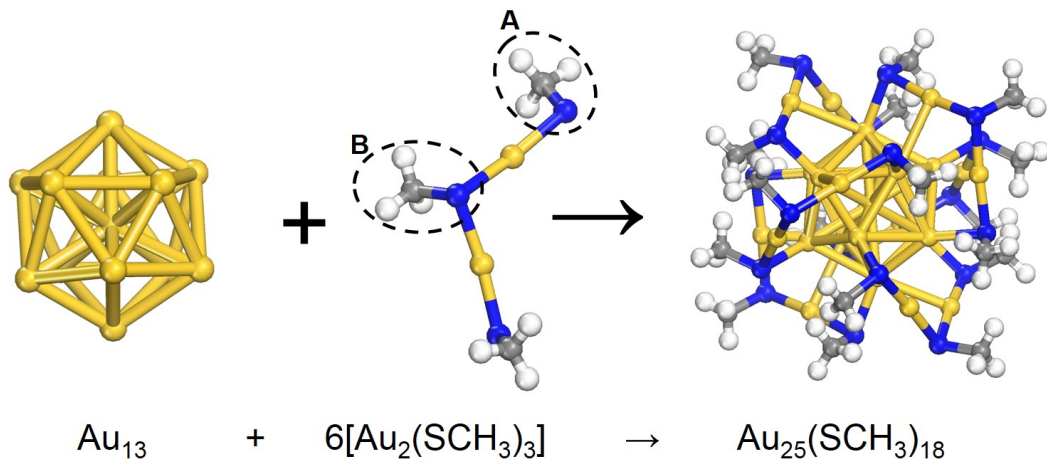


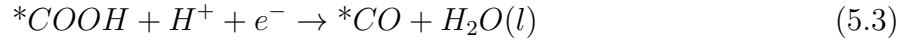
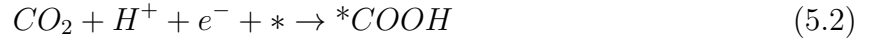
Figure 5.1: Schematic of the fully-ligand protected $\text{Au}_{25}(\text{SCH}_3)_{18}$ NC. The system is composed of a Au_{13} icosahedral core protected by a shell network of six $\text{Au}_2(\text{SR})_3$. The Au, S, C, and H atoms are colored yellow, blue, grey, and white, respectively. The labels A and B on the $\text{Au}_2(\text{SR})_3$ shell network represent the two distinct types of coordinated sulfur in the NC shell.

The Au_{25}^q NC which has been stably synthesized in multiple charge states ($q = -1, 0, +1$) [122–124] has also been used for catalysis in each of the charge states [59]. In the supporting information (see Table A2 in Appendix A.3) we assess the relative stability of the Au_{25} NC in relation to the charge states using adiabatic electron affinity (AEA, $\text{Au}_{25}(\text{SCH}_3)_x^0 + e^- \rightarrow \text{Au}_{25}(\text{SCH}_3)_x^-$) and adiabatic ionization potential (AIP, $\text{Au}_{25}(\text{SCH}_3)_x^0 \rightarrow \text{Au}_{25}(\text{SCH}_3)_x^+ + e^-$) [125, 126]. Studies have also suggested that under reaction conditions, the Au_{25} NC can partially lose ligands [57, 60]. Therefore we calculate the energy required to remove ligands from the $\text{Au}_{25}(\text{SCH}_3)_{18}$ NC. We initially focus on the removal of -SR (-SCH₃) from the $6[\text{Au}_2(\text{SCH}_3)_3]$ shell of the fully ligand-protected NC in each different charge state. The removal of a -SR ligand would expose an Au atom and enable interaction with adsorbates. However, theoretical studies on CO₂ reduction on Ni-Fe-S Cubanes [119] and MoS₂ [127] catalysts have shown that the COOH intermediate can be stabilized more favorably on the S atoms of the catalysts compared to other available sites. Thus, we also considered removal of -R (-CH₃) from the Au_{25} NCs to expose an S atom to the reaction intermediates for CO₂ reduction to CO.

The ΔG for ligand removal of -SR from $\text{Au}_{25}(\text{SCH}_3)_{18}$ was calculated as an electrochemical reduction step, using Equation 5.1, which was derived according to the following reduction reaction: $\text{Au}_{25}(\text{SCH}_3)_{18}^q + \text{H}^+ + \text{e}^- \rightarrow \text{HSCH}_3 + \text{Au}_{25}(\text{SCH}_3)_{17}^q$.

$$\Delta G_{\text{methylthiol-removal}} = G[\text{Au}_{25}(\text{SCH}_3)_{17}^q] + G[\text{HSCH}_3] - G[\text{Au}_{25}(\text{SCH}_3)_{18}^q] - \frac{1}{2}G[\text{H}_2] \quad (5.1)$$

Where $G[\text{Au}_{25}(\text{SCH}_3)_{17}]$, $G[\text{HSCH}_3]$, $G[\text{Au}_{25}(\text{SCH}_3)_{18}]$, and $G[\text{H}_2]$ are the gas phase free energies of the isolated NC with a removed thiol, the HSCH_3 molecule, the fully ligand-protected NC, and the H_2 molecule, respectively. The ΔG for removal of -R was calculated in the same manner as for -SR with $G[\text{Au}_{25}(\text{SCH}_3)_{17}]^q$ and $G[\text{HSCH}_3]$ in Equation 5.1 being replaced by $G[\text{Au}_{25}\text{S}(\text{SCH}_3)_{17}]^q$ and $G[\text{CH}_4]$, respectively. An overview of the potential states of the Au_{25}^q NC under reaction conditions that we consider in this study are shown in Figure 5.2 (shown for - SCH_3 removal). Prior studies have suggested [42, 47, 60] that CO_2 reduction and hydrogen evolution can take place through the following steps:



An example for determining reaction energetics using the first step of CO_2 reduction on the NCs (Equation 5.2), is calculated as follows in Equation 5.7:

$$\Delta G_{* \text{COOH}} = G[* \text{COOH}] + G[\text{NC}] - G[\text{CO}_2] - \frac{1}{2}G[(\text{H}_2)] + neU \quad (5.7)$$

Where $G[\text{COOH}^*]$, $G[\text{NC}]$, $G[\text{CO}_2]$, $G[\text{H}_2]$ are the gas phase free energies of the COOH adsorbed on a NC, the NC, the CO_2 molecule, and the H_2 molecule, respectively. In the supporting information (see Figure A12 in Appendix A.3) we also assessed CO_2 adsorption on the NCs and observed only physisorbed CO_2 as previously reported [48].

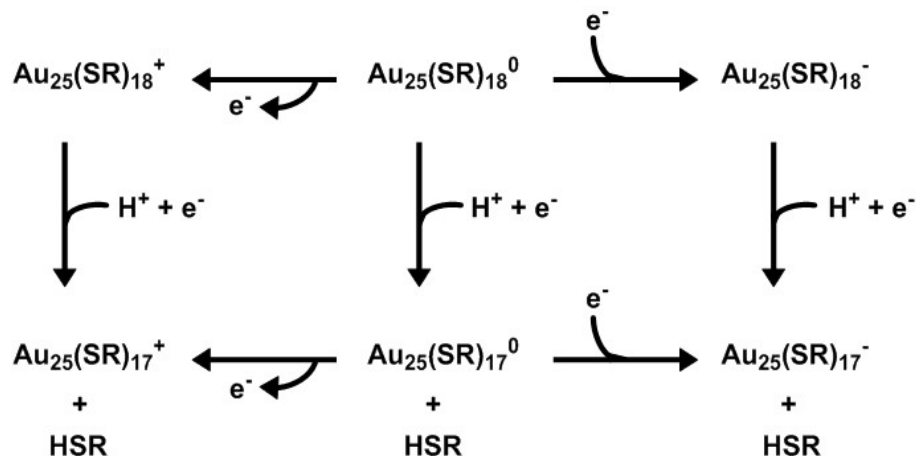


Figure 5.2: A cycle which illustrates potential states of the Au_{25} NC under reaction conditions. The top and bottom rows, show electron transfer to form the fully ligand-protected and partially ligand removed NCs in each charge state, respectively. The vertical steps indicate ligand removal from $\text{Au}_{25}(\text{SR})_{18}^q$ to form $\text{Au}_{25}(\text{SR})_{17}^q$.

5.2 RESULTS AND DISCUSSION

5.2.1 CO_2 Reduction and H_2 Evolution on Fully Ligand-Protected Nanoclusters

DFT geometry optimizations illustrated that the final structures of the fully ligand-protected $\text{Au}_{25}(\text{SR})_{18}^q$ ($q = -1, 0, +1$) NCs are nearly structurally identical to the experimental crystal structure [59, 122, 124, 128]. The calculated free energy diagrams for CO_2 reduction and H_2 evolution on the fully ligand-protected $\text{Au}_{25}(\text{SCH}_3)_{18}^q$ NCs ($q = -1, 0, +1$), at $U=0$ V (solid lines) are shown in Figure 5.3. The ΔG values of the reactions were also evaluated at an applied potential of -1.0 V vs RHE ($U = -1.0$ V, dashed lines in Figure 5.3), the potential at which peak production of CO was observed in experimental studies on the NCs [48, 58]. As shown in Figure 5.3(a), CO_2 reduction to CO on the fully ligand-protected NCs $\text{Au}_{25}(\text{SCH}_3)_{18}$ in each charge state, appears to be unfavorable due to the largely endergonic step for COOH stabilization ($\Delta G > 1.82$ eV). The observed unfavorable ΔG (*COOH), agrees with previous computational observations by Alfonso et al., for CO_2 reduction on the $\text{Au}_{25}(\text{SCH}_3)_{18}^-$ NC

[60]. Although for the hydrogen evolution reaction at $U=0$ V, the H adsorption step is also endergonic (5.3(b)), the ΔG for H adsorption (Equation 5.5) is more favorable than the COOH adsorption (Equation 5.2). Furthermore, at $U = -1.0$ V, the hydrogen evolution reaction becomes exergonic on the $\text{Au}_{25}(\text{SCH}_3)_{18}^q$ ($q = 0, +1$) NCs. Overall, the large positive ΔG values for CO_2 reduction on the fully ligand-protected NCs suggest that the production of CO is not feasible on these NCs. Thus, we focused on partially ligand-removed NCs, which have been experimentally shown to be active catalysts [57, 64–68].

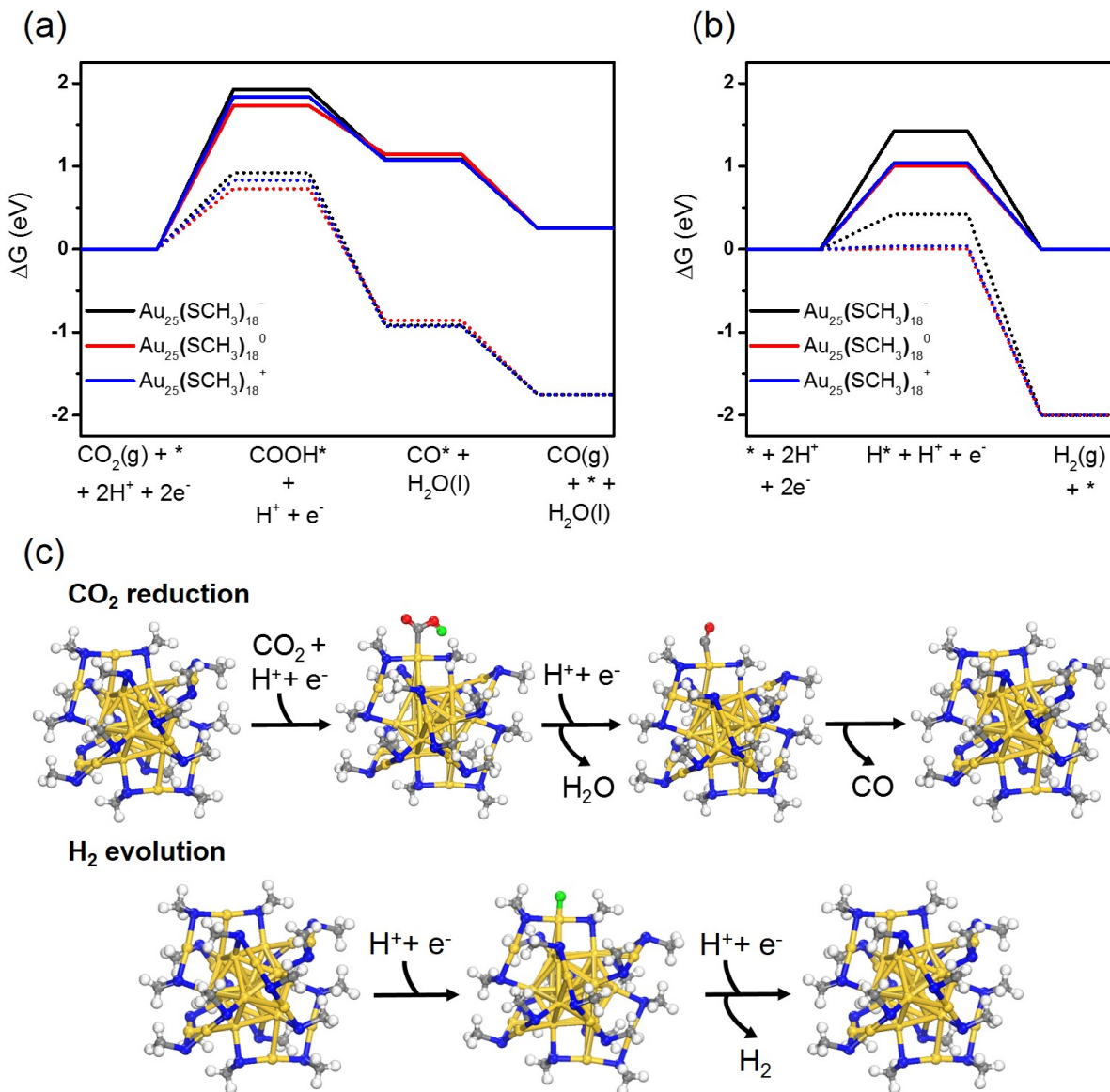


Figure 5.3: Free energy diagrams (ΔG) for the (a) reduction of CO_2 to CO and (b) hydrogen evolution on the fully ligand-protected $\text{Au}_{25}(\text{SCH}_3)_{18}^q$ ($q = -1, 0, +1$) NCs. The black, red, and blue lines represent the energy diagrams generated using a NC in the -1, 0, and +1 charge states, respectively. The solid lines illustrate the energy diagrams at $U = 0$ V, while the dashed lines represent the energy diagrams at an applied potential of $U = -1.0$ V. (c) Illustrations of the CO_2 reduction and the hydrogen evolution reactions. The Au, S, C, and O, atoms are colored yellow, blue, grey, and red, respectively. The H atoms are white, except for H on the carboxyl (in CO_2 reduction) and the adsorbed H (in hydrogen evolution) which are colored lime green for clarity.

5.2.2 CO₂ reduction and H₂ Evolution on Partially Ligand-Removed Nanoclusters

Figure 5.4(a) illustrates partial ligand-removal from the Au₂₅(SCH₃)₁₈ NC via a reduction reaction. We focus on removing one -SCH₃ ligand, connected to a core Au atom of the NC (labeled in Figure 5.1 as site "A" and also shown in Figure 5.4(a)), as has been done in previous studies [60]. It should be noted that removing -SCH₃ from site "A" in Figure 5.4 is more energetically favorable than from site "B" (see Figure A13 in the supporting information Appendix A.3). In the resulting partially ligand-removed Au₂₅(SCH₃)₁₇ NC, the Au atom of the shell, which was previously bound to the removed -SCH₃ ligand, is now connected to an Au atom of the core. According to our geometry optimization calculations, aside from the site where the -SCH₃ ligand was removed, the Au₂₅(SCH₃)₁₇^q NCs remain geometrically similar to the Au₂₅(SCH₃)₁₈^q NC. To assess the ability of the Au₂₅(SCH₃)₁₈^q NCs to release a -SCH₃ ligand, we calculated the ΔG for the electrochemical step of Au₂₅(SCH₃)₁₇^q formation from Au₂₅(SCH₃)₁₈^q as shown in Figure 5.4(b). The observed trend in ΔG for removing a ligand from Au₂₅(SCH₃)₁₈^q at U = 0 V and -1.0 V is as follows (from most favorable to least favorable): Au₂₅(SCH₃)₁₈⁰ < Au₂₅(SCH₃)₁₈⁺ < Au₂₅(SCH₃)₁₈⁻. This trend follows the order of increasing stability of the fully ligand-protected NCs as depicted on the increasing HOMO - LUMO gaps, calculated by Akola et al [129]. At U = 0 V the formation of the partially ligand-removed Au₂₅(SCH₃)₁₇^q NCs is less endergonic than the COOH adsorption on the fully ligand-protected Au₂₅(SCH₃)₁₈^q NCs. Interestingly, at U = -1.0 V, the ΔG for Au₂₅(SCH₃)₁₇ formation becomes exergonic in each charge state, as shown by the dashed lines in Figure 5.4(b). Thus, under reaction conditions (-1.0 V vs. RHE) calculations clearly predict the formation of partially ligand-removed catalysts.

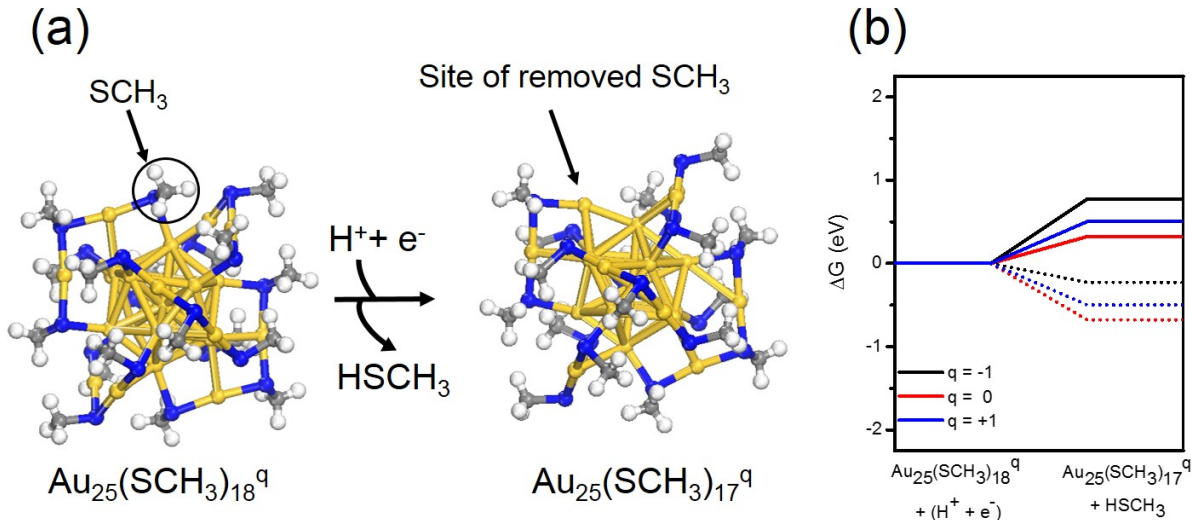


Figure 5.4: (a) Schematic for reduction of the fully ligand-protected NCs ($\text{Au}_{25}(\text{SCH}_3)_{18}^q$) to partially ligand-removed, $\text{Au}_{25}(\text{SCH}_3)_{17}^q$. (b) Free energy diagram for removing one $-\text{SCH}_3$ from the NC. As described in Figure 5.3, the colored, solid, and dashed lines represent the different charge states and energetics at $U = 0$ V and at $U = -1.0$ V, respectively.

Following the observation of exergonic ΔG for $\text{Au}_{25}(\text{SCH}_3)_{17}^q$ formation at $U = -1.0$ V, we assessed CO_2 reduction and H_2 evolution on the $\text{Au}_{25}(\text{SCH}_3)_{17}^q$ NCs ($q = -1, 0, +1$). As shown in Figure 5.5(a), we found that the partially ligand-removed NCs better stabilized the COOH intermediate ($\Delta G < 1.42$ eV) relative to the fully ligand-protected NCs ($\Delta G > 1.82$ eV). Thus, in each charge state the presence of ligand-removed sites on the NCs enhances COOH surface stabilization compared to the fully ligand-protected NCs. The lower $\Delta G(^*\text{COOH})$ observed on the $\text{Au}_{25}(\text{SCH}_3)_{17}^q$ NCs suggests that ligand removal is important for the Au NCs to become active, as highly endergonic free energies were observed on the fully ligand-protected NCs even with an applied potential ($U = -1.0$ V). The $\text{Au}_{25}(\text{SCH}_3)_{17}^-$ NC had the least endergonic $\Delta G(^*\text{COOH})$ compared to $\text{Au}_{25}(\text{SCH}_3)_{17}^q$ ($q = 0, +1$) at $U = 0$ V, which is conceptually consistent with the Lewis acidity of CO_2 . Thus, we would expect the partially ligand-removed NCs to be most active in a negative charge state. Given the exergonic $\Delta G(^*\text{H})$ shown in Figure 5.5(b), we would also expect competition with H_2 evolution on partially ligand-removed NCs. It should be noted that adsorbate interactions can be influenced by solvation [121]. Thus, in the supporting information (see Figure A14

in Appendix A.3) we assessed the H_2O solvent effect on CO_2 reduction and H_2 evolution energetics on the $\text{Au}_{25}(\text{SCH}_3)_{17}^-$ NC. The results showed an enhancement in stabilizing the COOH^* intermediate in the presence of H_2O . Additionally, the trends observed without solvation (i.e. competition with H_2 evolution), remained in the solvated case studied.

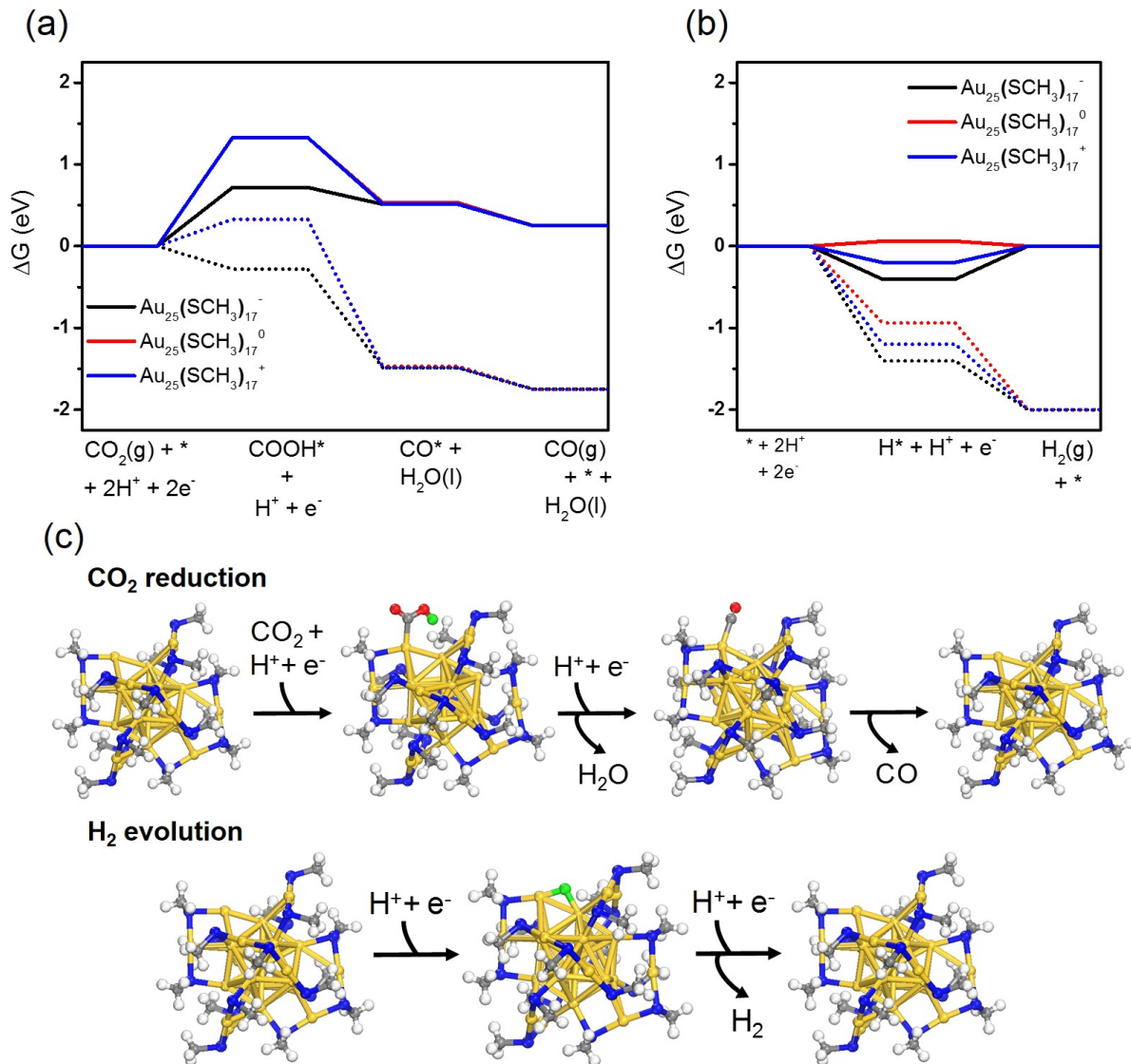


Figure 5.5: Free energy diagrams (ΔG) for the (a) reduction of CO_2 to CO and the (b) hydrogen evolution reaction on the $\text{Au}_{25}(\text{SCH}_3)_{17}^q$ ($q = -1, 0, +1$) NCs (with a ligand removed). (c) Illustrations of CO_2 reduction and H_2 evolution reaction steps. The color code for the diagrams is as described in Figure 5.3.

Having shown that the ligand removal on the NCs can generate active sites for CO₂ electroreduction and knowing that catalysts with surface sulfur atoms, such as Ni-Fe-S Cubanes [119] and MoS₂ [127], stabilize the COOH intermediate in CO₂ reduction, we investigated the removal of -CH₃ from the Au₂₅(SCH₃)₁₈ NC to generate a surface sulfur site instead of a bare Au site (Figure 5.6(a)). Similarly, to -SCH₃ removal, we focus on removing -CH₃ from site A as indicated in Figure 5.1, in each charge state of the Au₂₅ NC. The observed trend for removing a -CH₃ from Au₂₅(SCH₃)₁₈^q (see Figure 5.6(b)) at U = 0 V and -1.0 V is the same as removing -SCH₃ from Au₂₅(SCH₃)₁₈^q: Au₂₅(SCH₃)₁₈⁰ < Au₂₅(SCH₃)₁₈⁺ < Au₂₅(SCH₃)₁₈⁻ (from most favorable to least favorable). Remarkably, unlike the endergonic ΔG observed for -SCH₃ removal at U = 0 V, the ΔG for -CH₃ removal is exergonic in each charge state. Thus, under reaction conditions (-1.0 V vs. RHE) calculations predict that bare Au sites (due to -SCH₃ removal) and S sites (due to -CH₃ removal) may coexist. We note that we have not assessed here the free energies for ligand removal associated with an experimentally utilized ligand (i.e. -SC₂H₄Ph) due to computational constraints. However, in the supporting information (see Figure A15 in Appendix A.3) we present an energy analysis comparing -SC₂H₄Ph removal to -C₂H₄Ph removal in the negatively charged state of the Au₂₅ NC. These results indicate that under reaction conditions the formation of the partially-ligand removed NCs is still plausible.

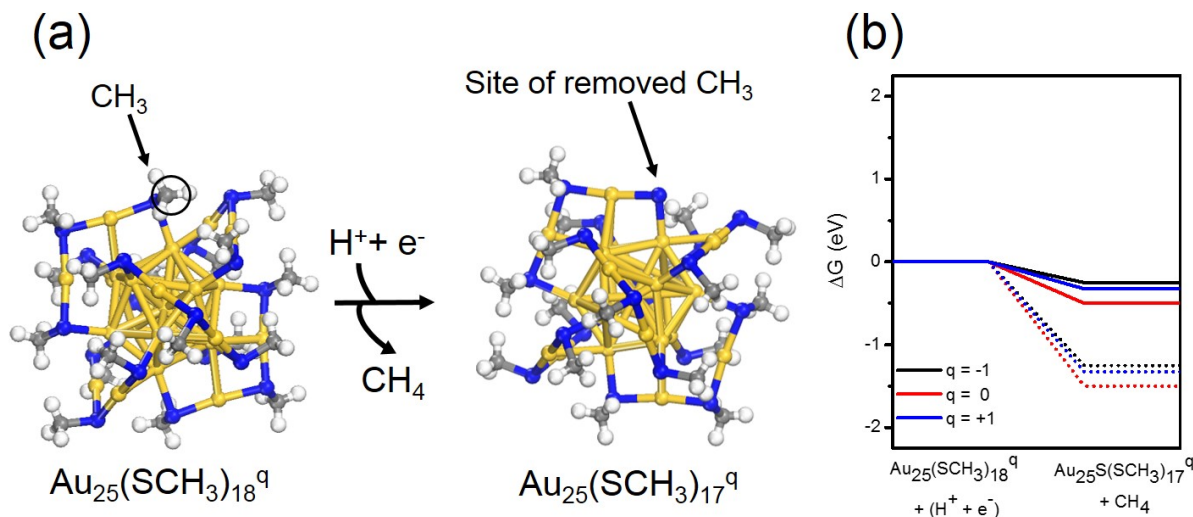
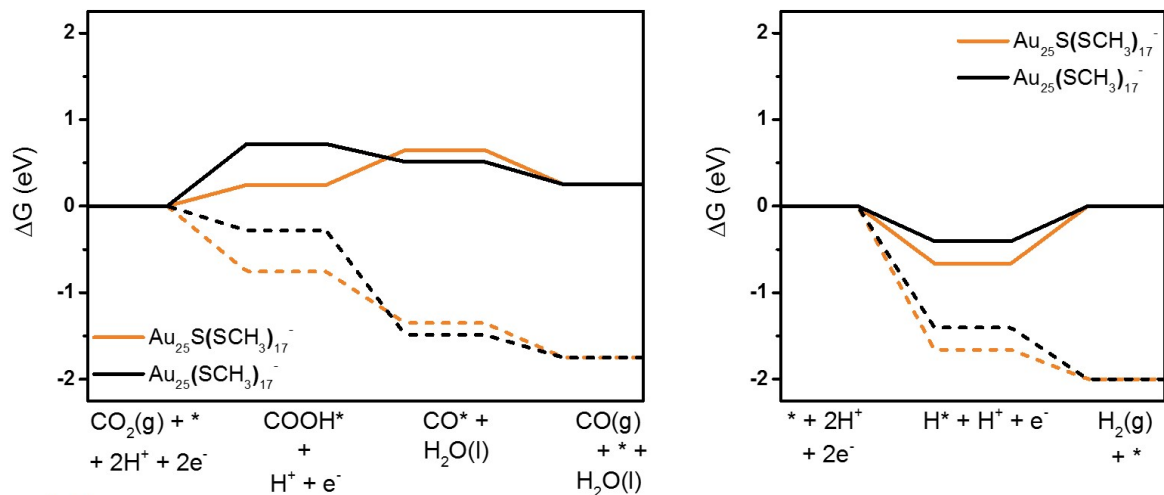


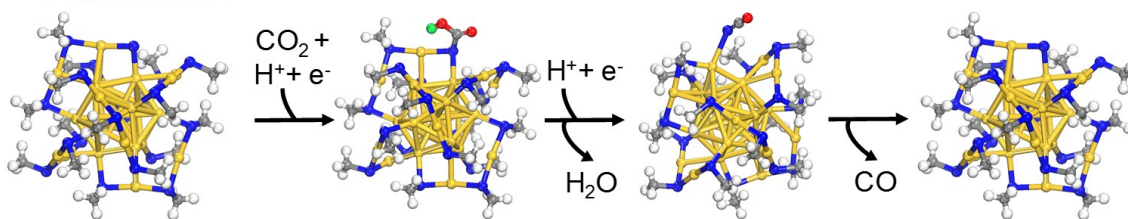
Figure 5.6: (a) Schematic for reduction of the fully ligand-protected NC ($\text{Au}_{25}(\text{SCH}_3)_{18}^q$) to one with $-\text{CH}_3$ removed, $\text{Au}_{25}\text{S}(\text{SCH}_3)_{17}^q$. (b) Free energy diagram for removing one $-\text{CH}_3$ from the NC. As described in Figure 5.3, the colored, solid, and dashed lines, represent the charge states, the energetics at $U = 0$ V and at $U = -1.0$ V, respectively.

Due to the preferable $\Delta G(^*\text{COOH})$ on $\text{Au}_{25}(\text{SCH}_3)_{17}^-$ relative to $\text{Au}_{25}(\text{SCH}_3)_{17}^q$ ($q = 0, +1$), we examine CO_2 reduction and H_2 evolution on the $\text{Au}_{25}\text{S}(\text{SCH}_3)_{17}^-$ NC ($-\text{CH}_3$ removed) and compare the energetics to the $\text{Au}_{25}(\text{SCH}_3)_{17}^-$ NC ($-\text{SCH}_3$ removed). As shown in Figure 5.7(a), we found that $\text{Au}_{25}\text{S}(\text{SCH}_3)_{17}^-$ stabilizes COOH more favorably ($\Delta G(^*\text{COOH}) = 0.33$ eV) relative to $\text{Au}_{25}(\text{SCH}_3)_{17}^-$ NC ($\Delta G(^*\text{COOH}) = 0.81$ eV). This enhanced COOH adsorption could be attributed to the larger negative charge on the exposed S site of the $\text{Au}_{25}\text{S}(\text{SCH}_3)_{17}^-$ NC compared to the exposed Au site of the $\text{Au}_{25}(\text{SCH}_3)_{17}^-$ NC (see Figure A16 in Appendix A.3). In addition, the exposed S site of the $\text{Au}_{25}\text{S}(\text{SCH}_3)_{17}^-$ NC contributes to increased electron density near the Fermi level of the $\text{Au}_{25}\text{S}(\text{SCH}_3)_{17}^-$ NC compared to the fully protected NC, $\text{Au}_{25}(\text{SCH}_3)_{18}^-$, which in turn contributes to the reactivity of the NC (see Figure A17 in Appendix A.3). However, in Figure 5.7(b), we also observe that H adsorption at $U = 0$ V is more exergonic on $\text{Au}_{25}\text{S}(\text{SCH}_3)_{17}^-$ than on $\text{Au}_{25}(\text{SCH}_3)_{17}^-$. This indicates that H_2 evolution would compete with CO_2 reduction on $\text{Au}_{25}\text{S}(\text{SCH}_3)_{17}^-$ NCs.



(c)

CO₂ reduction



H₂ evolution

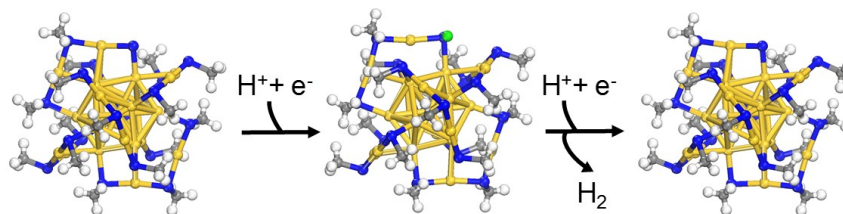


Figure 5.7: Free energy diagrams (ΔG) for the (a) reduction of CO_2 to CO and the (b) hydrogen evolution on the $-\text{CH}_3$ removed $\text{Au}_{25}\text{S}(\text{SCH}_3)_{17}^-$ NC and on the $-\text{SCH}_3$ removed $\text{Au}_{25}(\text{SCH}_3)_{17}^-$ NC. The orange and black lines represent the energy diagrams for the $\text{Au}_{25}\text{S}(\text{SCH}_3)_{17}^-$ and $\text{Au}_{25}(\text{SCH}_3)_{17}^-$ NCs, respectively. The solid lines illustrate the energy diagrams at $U = 0$ V, while the dashed lines represent the energy diagrams at an applied potential of $U = -1.0$ V. The color code for (c) the illustrations of CO_2 reduction and H_2 evolution are as described in Figure 5.3.

5.2.3 CO vs H₂ Product Selectivity

Determining the selectivity between CO₂ reduction and hydrogen evolution would typically require an in depth kinetic analysis. However, to give a qualitative estimate of the selectivity we determine the difference between the limiting potentials for CO₂ reduction and H₂ evolution ($U_L(\text{CO}_2) - U_L(\text{H}_2)$) [127,130,131]. The more positive $U_L(\text{CO}_2) - U_L(\text{H}_2)$ corresponds to a higher selectivity towards CO₂ reduction relative to the set of NCs. As shown in Table 5.1, on the Au₂₅(SCH₃)₁₈^q and Au₂₅(SCH₃)₁₇^q NCs, the limiting step which determines $U_L(\text{CO}_2)$ is the COOH formation step. However, on the Au₂₅S(SCH₃)₁₇⁻ NC, the limiting step is CO (and H₂O) formation, which results in the smallest $|U_L(\text{CO}_2)|$ amongst all of the NCs in this study. H adsorption is the limiting step that determines $U_L(\text{H}_2)$ on the Au₂₅(SCH₃)₁₈^q and the Au₂₅(SCH₃)₁₇⁺ NCs, while the formation of H₂(g) is the limiting step responsible for $U_L(\text{H}_2)$ on the Au₂₅(SCH₃)₁₇^q (q = +1, -1) and Au₂₅S(SCH₃)₁₇⁻ NCs due to the exothermic H adsorption on the NCs. In Figure 5.8, the calculated $U_L(\text{CO}_2) - U_L(\text{H}_2)$ shows that the negatively charged species, Au₂₅(SCH₃)₁₈⁻, Au₂₅(SCH₃)₁₇⁻, and Au₂₅S(SCH₃)₁₇⁻ are the least selective towards H₂ production relative to the set of NCs. Although our results show that only the partially-ligand removed clusters, Au₂₅(SCH₃)₁₇⁻ and Au₂₅S(SCH₃)₁₇⁻, are most active for CO₂ reduction, it is only the Au₂₅S(SCH₃)₁₇⁻ NC which is selective to CO₂ reduction over H₂ evolution (positive value of $U_L(\text{CO}_2) - U_L(\text{H}_2)$). Therefore, the exposure of S atoms, within the NCs are important to tune selectivity towards CO₂ reduction. In experiments, the conditions that control the selectivity of the Au₂₅ catalyst towards CO include applied potentials, CO₂ flow rate, catalyst loading, and concentration of the electrolyte [58,132]. These Au₂₅ catalysts are also clearly active toward H₂ evolution. Shuo et al., showed that an Au₂₅/MoS₂ system enhanced the hydrogen evolution reaction activity compared to MoS₂ alone [133]. This enhanced activity was attributed to the electronic interactions at the Au-MoS₂ interface. Therefore, these Au NCs can display exceptional but different catalytic behavior depending on the chemical environment. The observed differences in catalytic behavior with changes to NC structure (fully-protected vs partially-ligand removed) shown in this study can be connected to the frontier orbitals HOMO-LUMO of the clusters (see supporting information Figure A18 in Appendix A.3). As shown in Figure

A18(b), the HOMO-LUMO gap of the NCs with a removed ligand becomes much smaller compared to the fully protected NC. In addition, the electron density observed on the ligand removed sites of $\text{Au}_{25}(\text{SCH}_3)_{17}^-$ and $\text{Au}_{25}\text{S}(\text{SCH}_3)_{17}^-$ becomes more localized and directional compared to $\text{Au}_{25}(\text{SCH}_3)_{18}^-$ which is important because changes in orbital localization and directionality has been shown to contribute to the reactivity of Au clusters [89, 134].

Table 5.1: Limiting step and potential of the Au_{25} NCs. $\text{H}^+ + \text{e}^-$ omitted for simplicity.

	CO_2	$U_L(\text{CO}_2)$	H_2	$U_L(\text{H}_2)$
$\text{Au}_{25}(\text{SCH}_3)_{18}^-$	$\text{CO}_2 + * \rightarrow * \text{COOH}$	-2.01 V	$* \rightarrow * \text{H}$	-1.38 V
$\text{Au}_{25}(\text{SCH}_3)_{18}^0$	$\text{CO}_2 + * \rightarrow * \text{COOH}$	-1.82 V	$* \rightarrow * \text{H}$	-0.96 V
$\text{Au}_{25}(\text{SCH}_3)_{18}^+$	$\text{CO}_2 + * \rightarrow * \text{COOH}$	-1.92 V	$* \rightarrow * \text{H}$	-1.00 V
$\text{Au}_{25}(\text{SCH}_3)_{17}^-$	$\text{CO}_2 + * \rightarrow * \text{COOH}$	-0.81 V	$* \text{H} \rightarrow \text{H}_2(\text{g}) + *$	-0.44 V
$\text{Au}_{25}(\text{SCH}_3)_{17}^0$	$\text{CO}_2 + * \rightarrow * \text{COOH}$	-1.42 V	$* \rightarrow * \text{H}$	-0.02 V
$\text{Au}_{25}(\text{SCH}_3)_{17}^+$	$\text{CO}_2 + * \rightarrow * \text{COOH}$	-1.42 V	$* \text{H} \rightarrow \text{H}_2(\text{g}) + *$	-0.24 V
$\text{Au}_{25}\text{S}(\text{SCH}_3)_{17}^-$	$* \text{COOH} \rightarrow * \text{CO} + \text{H}_2\text{O}(\text{l})$	-0.42 V	$* \text{H} \rightarrow \text{H}_2(\text{g}) + *$	-0.70 V

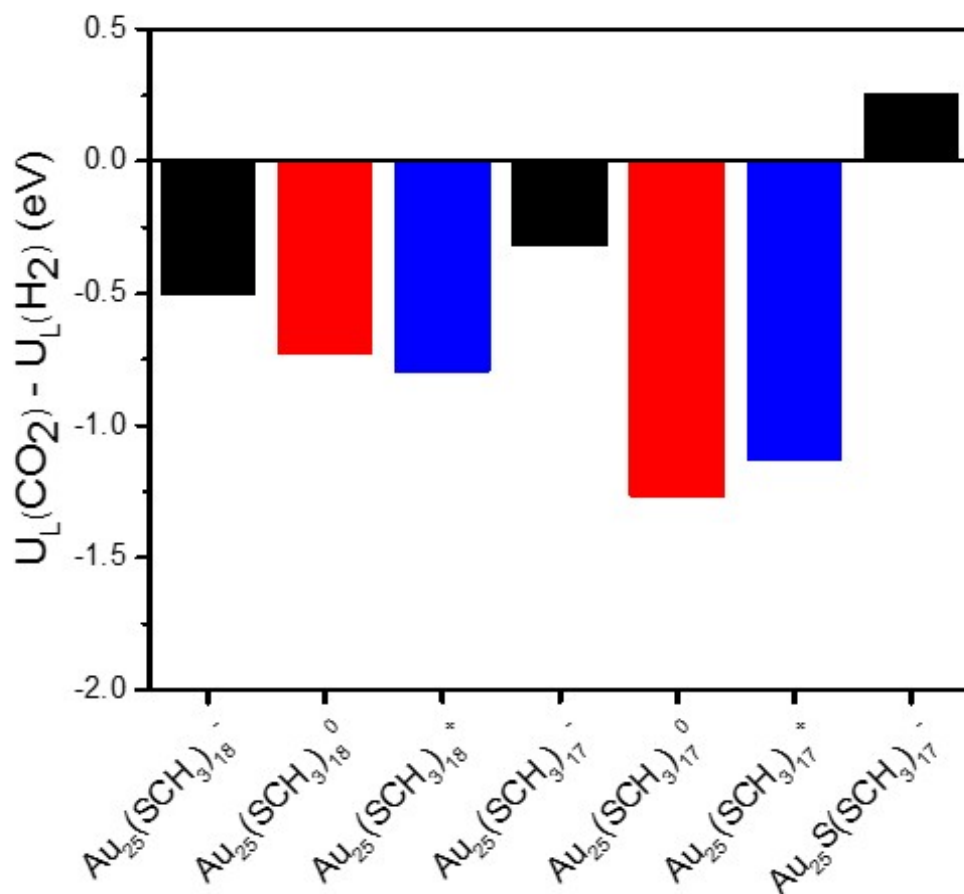


Figure 5.8: (a) Difference in limiting potentials of CO_2 reduction and hydrogen evolution ($U_L(\text{CO}_2) - U_L(\text{H}_2)$). The color code represents the three charge states of the Au_{25} NC (black: negative, red: neutral, blue: positive).

As a final note, although our results rationalize a series of experimental observations, they are solely based on thermodynamic viewpoints and do not take into consideration kinetic limitations in the form of activation barriers. Barriers for proton-electron transfer in CO₂ reduction to CH₄ and CH₃OH have been calculated on Pt, Cu, and Au surfaces [135, 136]. The calculated barriers for the steps relevant to this study (see Equations 5.2 and 5.3) were less than 1 eV which is surmountable under room temperature at experimentally applied potentials ($U = -1.0$ V). Thus, we would expect the proton-electron transfer barriers for CO₂ reduction on the Au NCs to be thermally accessible at room temperature. Furthermore, assuming the activation energies for the proton-electron transfer steps scale with ΔG_{rxn} , as in the Brønsted-Evans-Polanyi relationship, we would expect the lowest barriers to be observed on the ligand removed NCs [135].

5.3 CONCLUSIONS

In this work, we applied *Ab initio* electronic structure calculations to assess CO₂ reduction and H₂ evolution on fully ligand-protected (Au₂₅(SR)₁₈^q) and partially ligand-removed (removal of -SR and -R) NCs in three charge states $q = -1, 0$, and $+1$. Our results demonstrate that regardless of charge state, the Au₂₅(SR)₁₈^q NC is inactive for CO₂ reduction due to the relative instability of the associated COOH intermediate. On the contrary, our calculations showed that the formation of partially-ligand removed NCs, Au₂₅(SR)₁₇^q ($q = -1, 0, +1$) and Au₂₅S(SR)₁₇^q, are feasible under reaction conditions. Moreover, Au₂₅(SR)₁₇^q NCs and the Au₂₅S(SR)₁₇⁻ NC stabilized the COOH intermediate more favorably than the Au₂₅(SR)₁₈^q NCs. We therefore conclude that partially-ligand removed clusters, which expose Au and S sites, are the most active for CO₂ reduction under experimentally applied potentials. We found that hydrogen evolution likely competes with CO₂ reduction over the entire potential range of interest. By assessing selectivity, we determined that only the active Au₂₅(SR)₁₇⁻ NC would be selective towards CO₂ reduction over H₂ evolution. Overall, this work elucidates NC charge state and generation of active surface sites during electrocatalysis as responsible for the stabilization intermediates in CO₂ reduction to CO.

6.0 FUTURE WORK

6.1 KINETIC ANALYSIS FOR LIGAND REMOVAL

In the work detailed in Chapters 4 and 5 we focused on thermodynamic analysis of ligand removal from the Au_{25} NCs. However, an understanding of the kinetic barriers towards ligand removal would further verify the feasibility of this process under reaction conditions. To this end, we generated and optimized a $\text{Au}_{25}(\text{SEthPh})_{18}$ NC surrounded by 158 H_2O molecules using CP2K as shown in Figure 6.1, to study the ligand removal process. We performed *Ab initio* Molecular Dynamics calculations with the PBE [73] functional, the DZVP basis set [97] in combination with the GTH pseudopotentials [98] with a 500 Ry cutoff. Grimme’s D3 method [80] was used to account for dispersion interactions. The calculations were carried out in the NVT ensemble with a timestep of 0.5 fs at 300K. The Nosé-Hoover thermostat [137, 138] was used for temperature control. The system reached equilibrium within 6000 steps (3 ps). In future work CI-NEB and Metadynamics calculations will be performed on the $\text{Au}_{25}(\text{SEthPh})_{18}$ NC with 158 H_2O molecules to identify transition states for ligand removal of the solvated system.

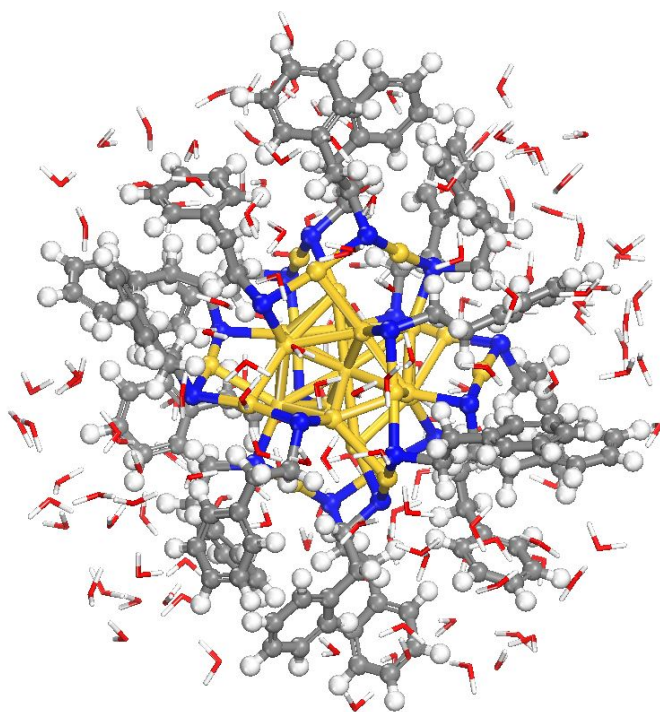


Figure 6.1: Optimized geometry of the solvated $\text{Au}_{25}(\text{SEthPh})_{18}$ NC with 158 H_2O .

APPENDIX

SUPPORTING INFORMATION

A.1 CO₂ ACTIVATION ON CU-BASED ZR-DECORATED NANOPARTICLES

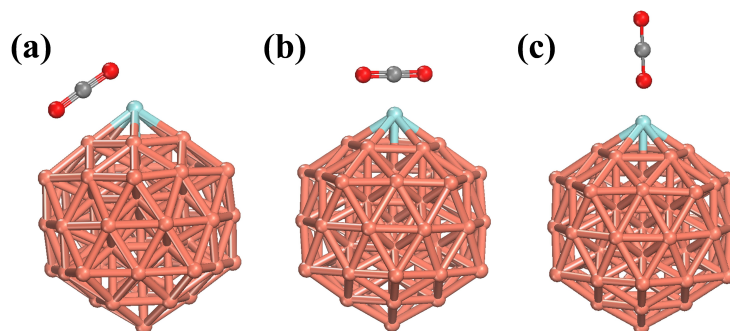


Figure A1: Three initial adsorption configurations of CO₂ on the Cu₅₄Zr NP were considered: (a) CO₂ molecule parallel to the Cu-Zr bond, (b) CO₂ adsorption to the NP with C of CO₂ interacting with Zr on the NP, and (c) perpendicular CO₂ adsorption with the O atom pointing to Zr.

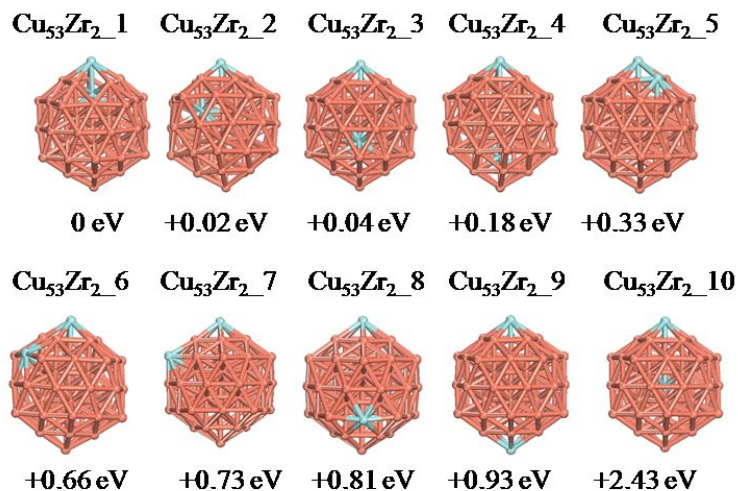


Figure A2: Different dopant sites of two Zr atoms in the 55-atom $\text{Cu}_{53}\text{Zr}_2$ NP. The value below each NP is the stability of the NPs relative to the most stable structure found ($\text{Cu}_{53}\text{Zr}_2_1$).

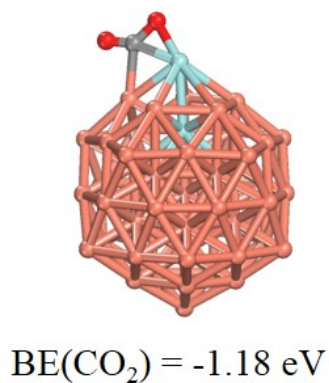


Figure A3: Chemisorbed CO_2 on $\text{Cu}_{53}\text{Zr}_2_1$ (most stable $\text{Cu}_{53}\text{Zr}_2$ NP as shown in Figure A2). The binding energy of CO_2 has been calculated to be -1.18 eV, which is strong and comparable to the segregated case of Zr.

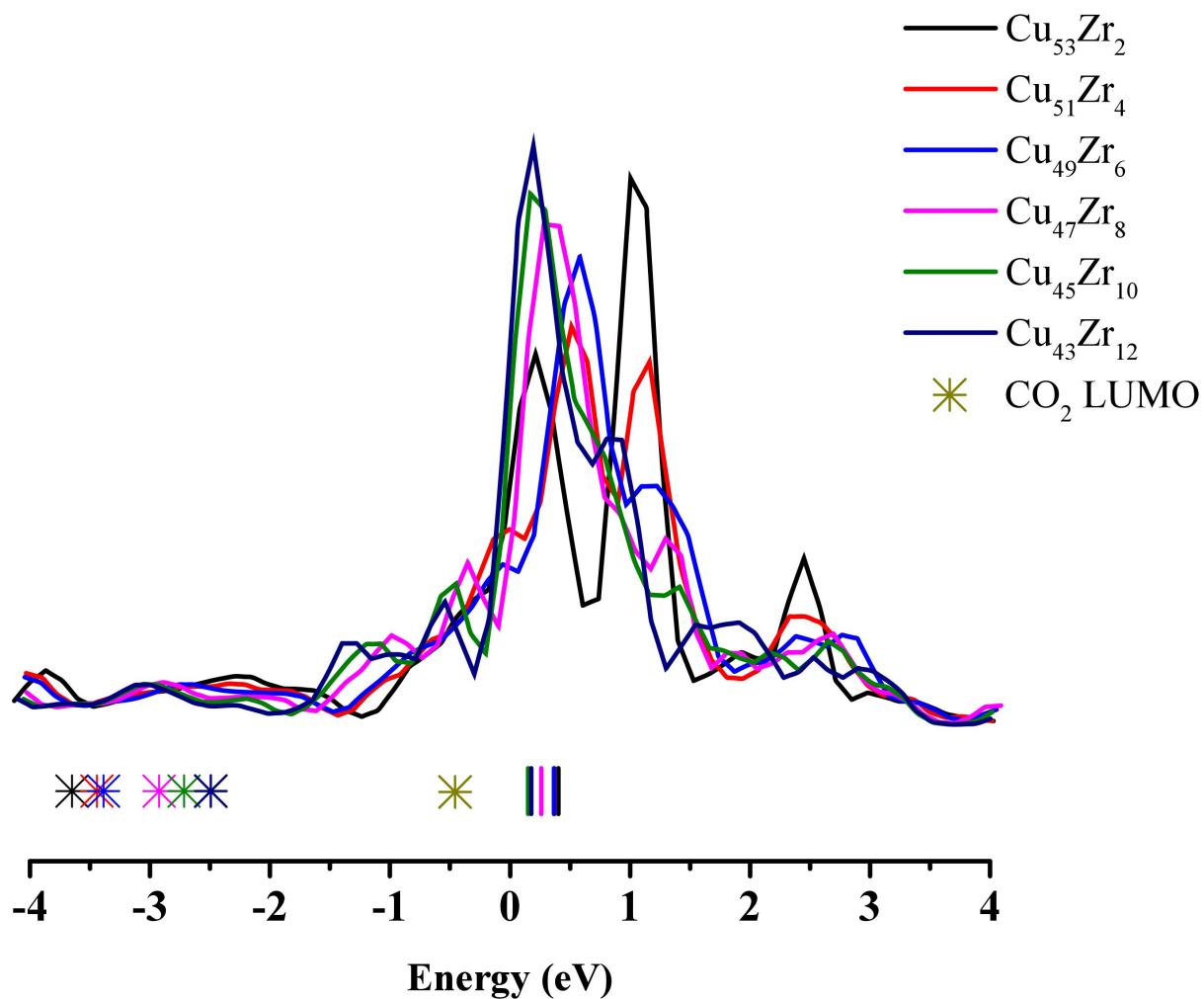


Figure A4: Local partial density of states (PDOS) of the d electrons for the $\text{Cu}_{55-x}\text{Zr}_x$ NPs. The asterisks and the solid lines below the PDOS represent the HOMO orbital energies and d_C of the $\text{Cu}_{55-x}\text{Zr}_x$ NPs. ($x = 2-12$), respectively. The green asterisk corresponds to the LUMO orbital of the CO_2 molecule. It should be noticed that the increasing Zr content brings the NP HOMO orbitals closer to the CO_2 LUMO, resulting to stronger CO_2 adsorption. The IP correlations presented in Figure 5(b) of the manuscript are relevant to the energy of the HOMO orbitals (HOMO energy can approximate the IP).

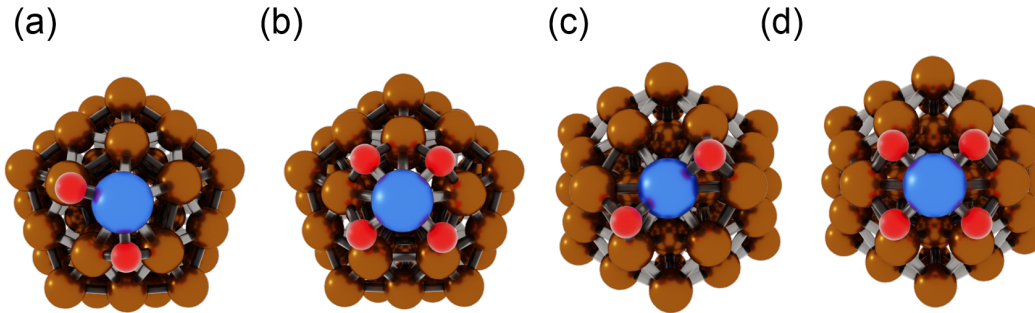


Figure A5: Surface oxidation configurations for the studied Cu_{54}Zr NPs, for which the Zr atom is oxidized with either two or four oxygen atoms: a) $\text{Cu}_{54}\text{ZrO}_2$ with Zr on a CN=6 site before oxidation. One oxygen atom bridges a Zr-Cu bond, and the other is on a hollow-site position between Cu and Zr. b) $\text{Cu}_{54}\text{ZrO}_4$ with Zr on a CN=6 site before oxidation. All four oxygen atoms occupy hollow-site positions between Cu and Zr. c) $\text{Cu}_{54}\text{ZrO}_2$ with Zr on a CN=8 site before oxidation. Both oxygen atoms are on hollow sites between Cu and Zr. d) $\text{Cu}_{54}\text{ZrO}_4$ with Zr on a CN=8 site before oxidation. All four oxygen atoms are on hollow sites between Cu and Zr.

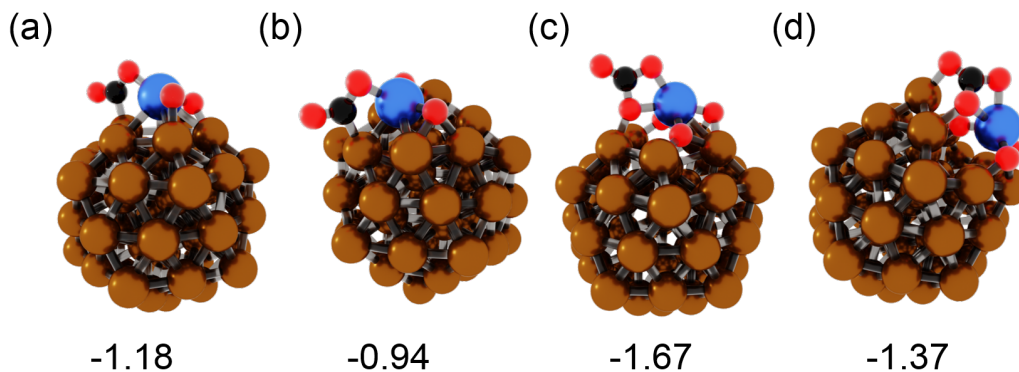


Figure A6: Lowest-energy adsorption configurations of CO_2 on $\text{Cu}_{54}\text{ZrO}_2$ with Zr in a) CN=6 and b) CN=8 adsorption sites before oxidation and $\text{Cu}_{54}\text{ZrO}_4$ with Zr in c) CN=6 and d) CN=8 before oxidation

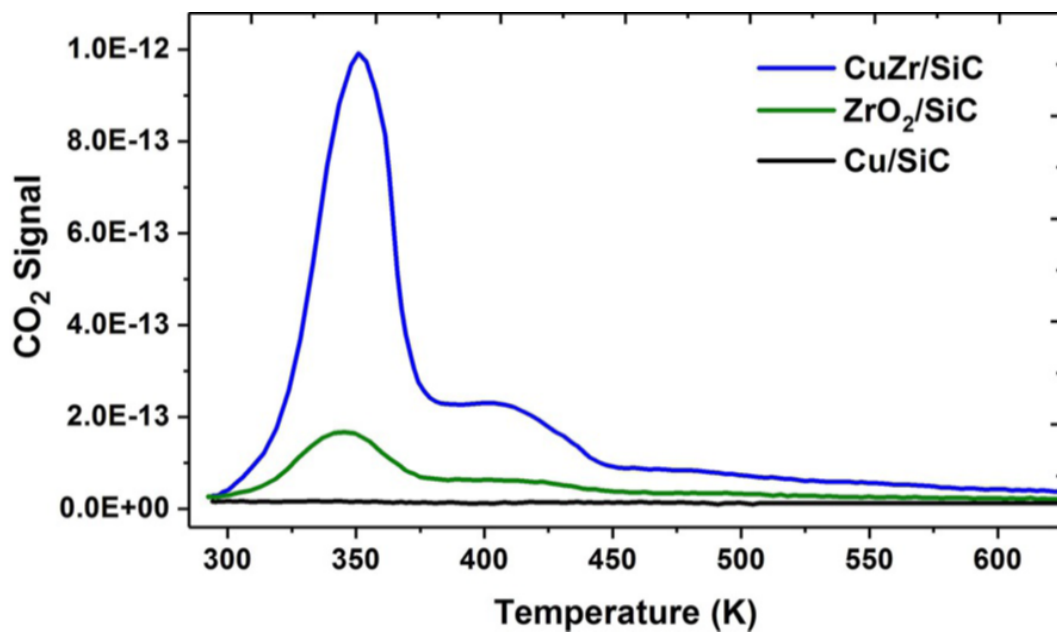


Figure A7: CO₂-TPD profiles of CuZr/SiC, Cu/SiC, and ZrO₂/SiC

A.2 INFLUENCE OF ATOMIC-LEVEL GOLD CATALYST MORPHOLOGY ON CO₂ ELECTROREDUCTION

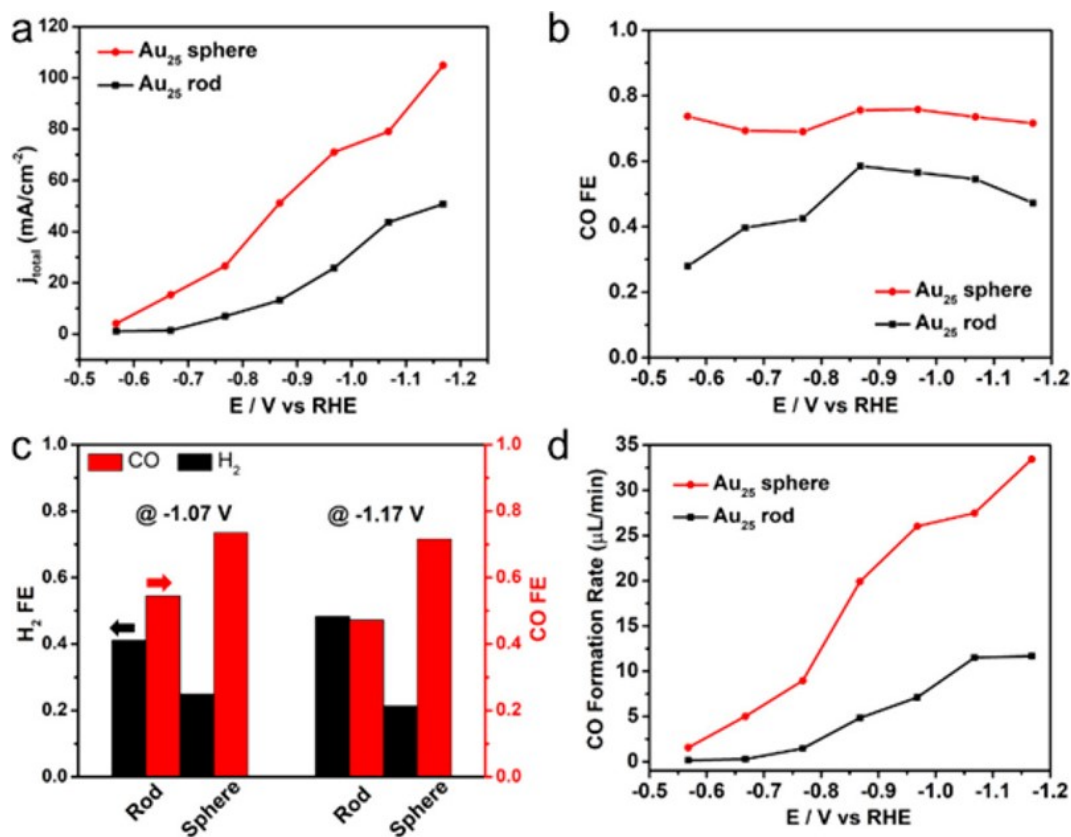


Figure A8: Electrocatalytic CO₂ reduction performance of the two Au₂₅ NCs. (a) Total current density of CO₂ reduction, (b) Faradaic Efficiency (FE) for CO production over Au₂₅ nanosphere and nanorod catalysts, (c) FEs for CO and H₂ at the potential of -1.07 and -1.17 V over Au₂₅ nanosphere and nanorod, respectively. (d) CO formation rates over Au₂₅ nanosphere and nanorod.

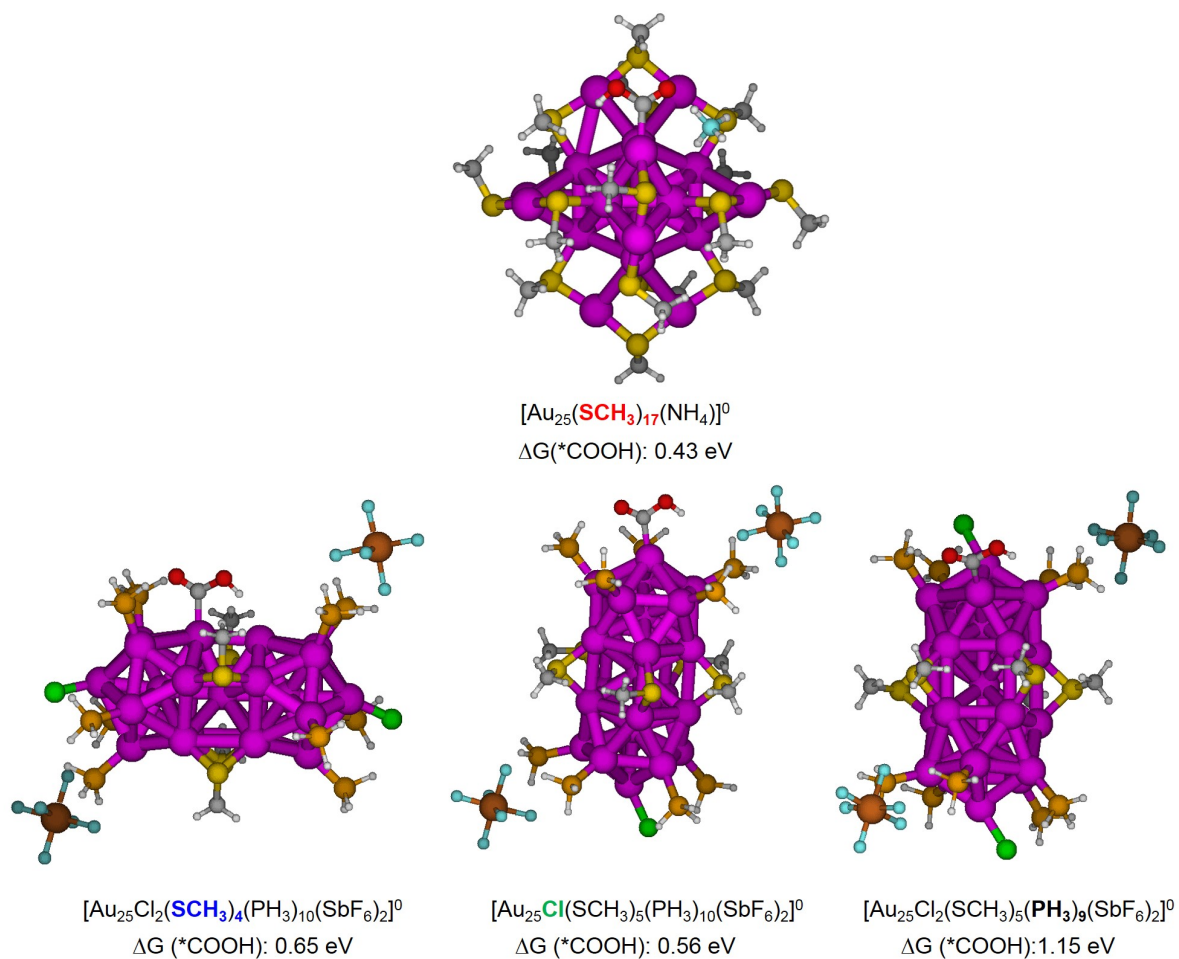


Figure A9: Different structures and associated free energies (ΔG) for the $*\text{COOH}$ formation step (with respect to our reference state) on the surface of the NCs with a ligand removed.

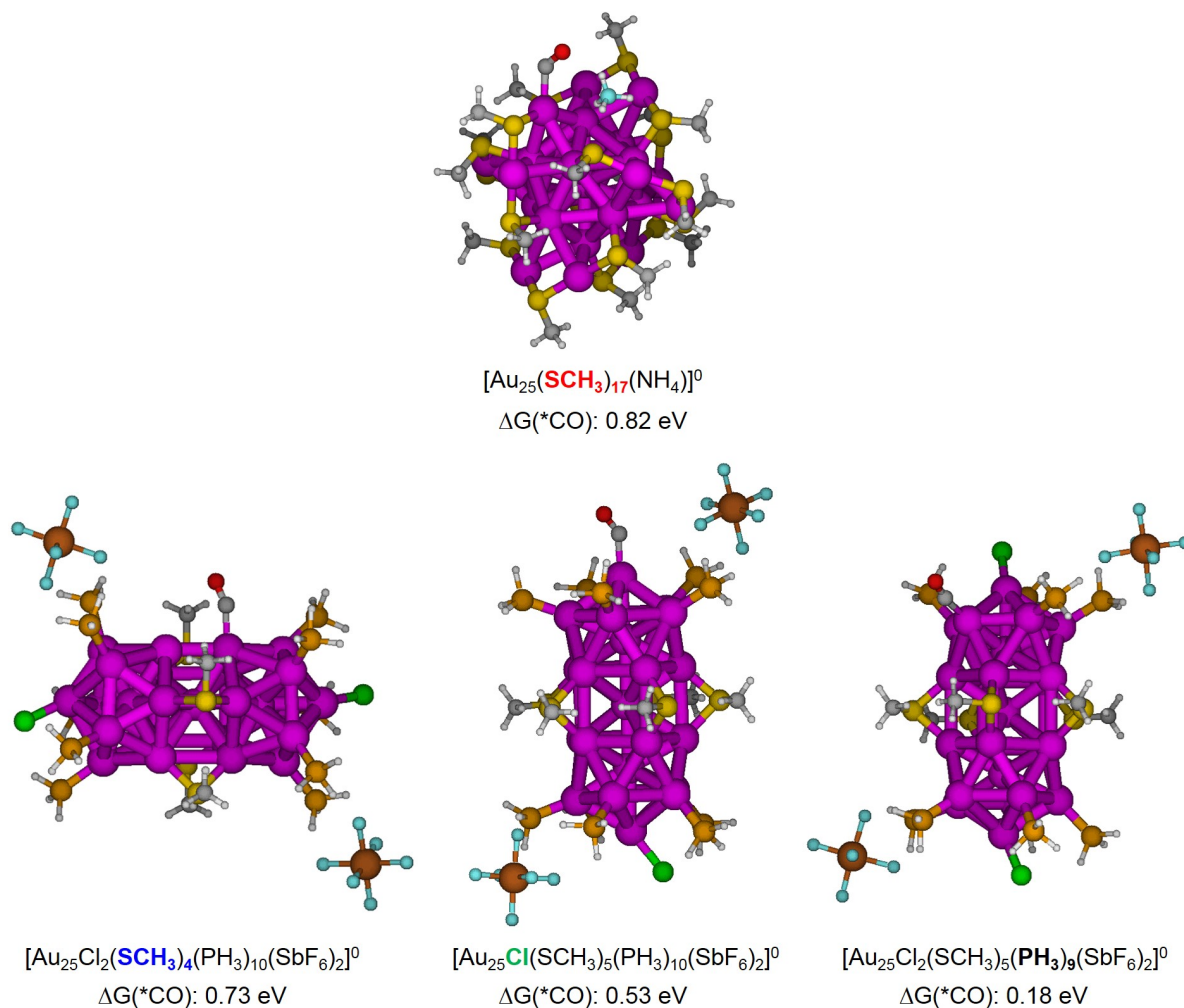
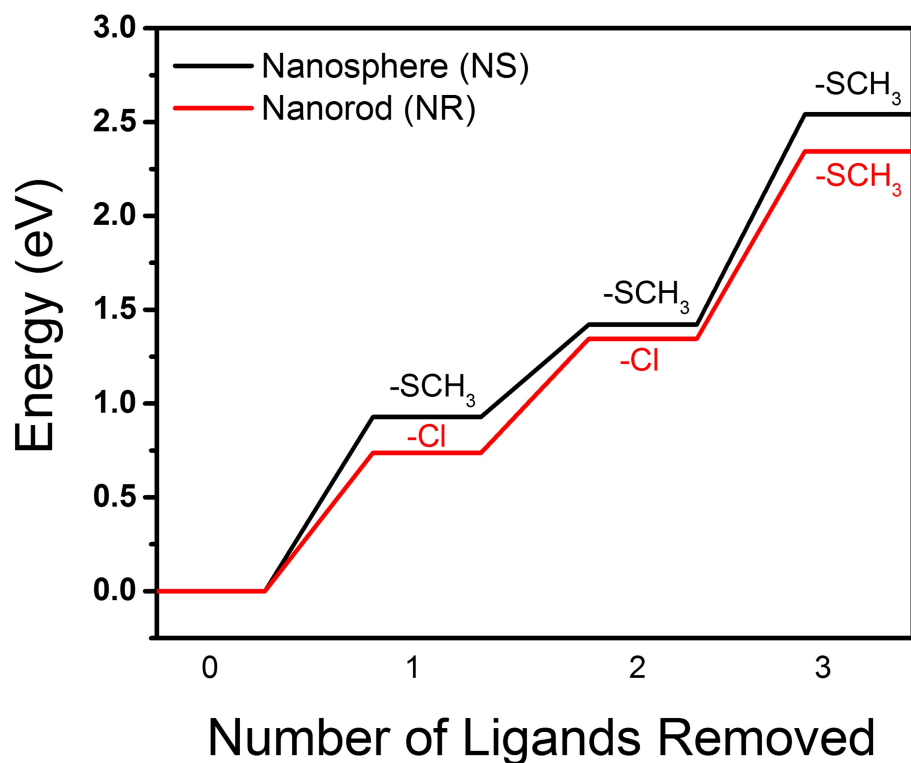
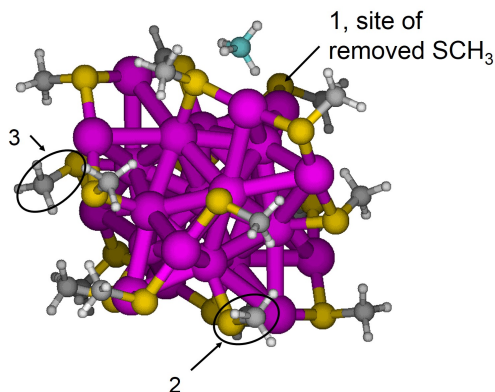


Figure A10: Different structures and associated free energies (ΔG) for the CO (and H_2O) formation step (with respect to our reference state) on the surface of the NCs with a ligand removed.

(a)



(b)



(c)

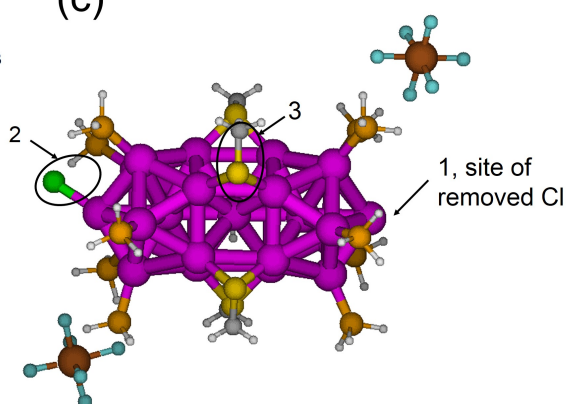


Figure A11: (a) Electronic energies in eV for ligand removal from the nanosphere (black line) and the nanorod (red line). The text on the lines refers to the type of ligand that was removed. From the nanosphere, -SCH₃ ligands were removed from the numbered sites shown in (b). Note that site 1 is where -SCH₃ was removed from in the manuscript. From the nanorod, ligands were removed from the numbered sites shown in (c). Note that site 1 is where -Cl was removed from in the manuscript.

A.3 ELUCIDATING THE ACTIVE SITES FOR CO₂ ELECTROREDUCTION ON LIGAND-PROTECTED GOLD NANOCLUSTERS

Table A1: Relative energies (to the lowest energy system) in eV of the Au₂₅ nanoclusters optimized with different multiplicities.

	M1	M3	M5
Au ₂₅ (SCH ₃) ₁₈ ⁻	0	0.96	1.88
Au ₂₅ (SCH ₃) ₁₈ ⁺	0	0.13	1.15
Au ₂₅ (SCH ₃) ₁₇ ⁰	0	0.53	1.51
Au ₂₅ S(SCH ₃) ₁₇ ⁰	0	0.38	1.43
	M2	M4	M6
Au ₂₅ (SCH ₃) ₁₈ ⁰	0	0.98	1.96
Au ₂₅ (SCH ₃) ₁₇ ⁻	0	0.93	2.03
Au ₂₅ S(SCH ₃) ₁₇ ⁻	0	0.95	1.98
Au ₂₅ (SCH ₃) ₁₇ ⁺	0	0.60	1.80
Au ₂₅ S(SCH ₃) ₁₇ ⁺	0	0.44	1.60

Table A2: Computed adiabatic electron affinities (AEA) and adiabatic ionization potentials (AIP) of Au₂₅(SCH₃)₁₀⁰, Au₂₅(SCH₃)₁₇⁰, and Au₂₅S(SCH₃)₁₇⁰ in eV.

	AEA	AIP
Au ₂₅ (SCH ₃) ₁₈ ⁰	-2.90	5.10
Au ₂₅ (SCH ₃) ₁₇ ⁰	-2.41	5.20
Au ₂₅ S(SCH ₃) ₁₇ ⁰	-2.63	5.29

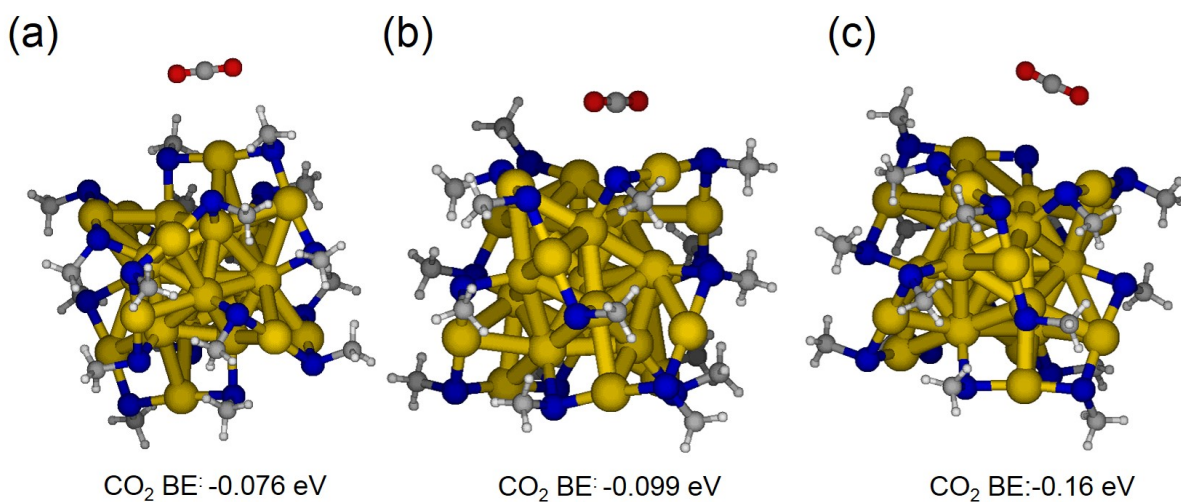


Figure A12: CO₂ adsorption on the negatively charged nanoclusters (a) Au₂₅(SCH₃)₁₈⁻, (b) Au₂₅(SCH₃)₁₇⁻, (c) Au₂₅S(SCH₃)₁₇⁻. Note that physisorption was observed on all the nanoclusters in this study (range: -0.07 to -0.16 eV).

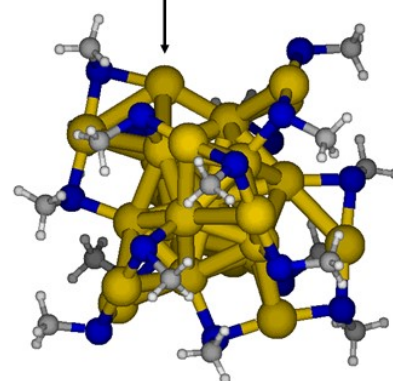
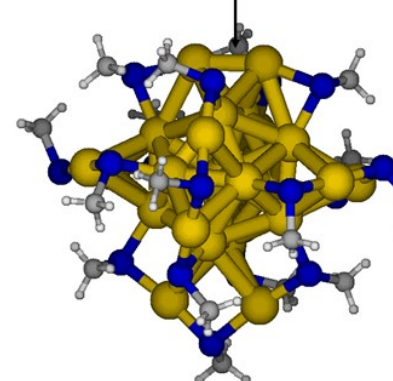
	Site A of removed SCH ₃	Site B of removed SCH ₃
		
$\Delta E(-)$	1.11	1.37
$\Delta E(0)$	0.65	1.30
$\Delta E(+)$	0.75	1.47

Figure A13: Changes in electronic energy (ΔE) for the reaction step of SCH₃ removal from Site A and Site B (shown in manuscript) of the Au₂₅(SCH₃)₁₈⁻ NC (values are in eV).

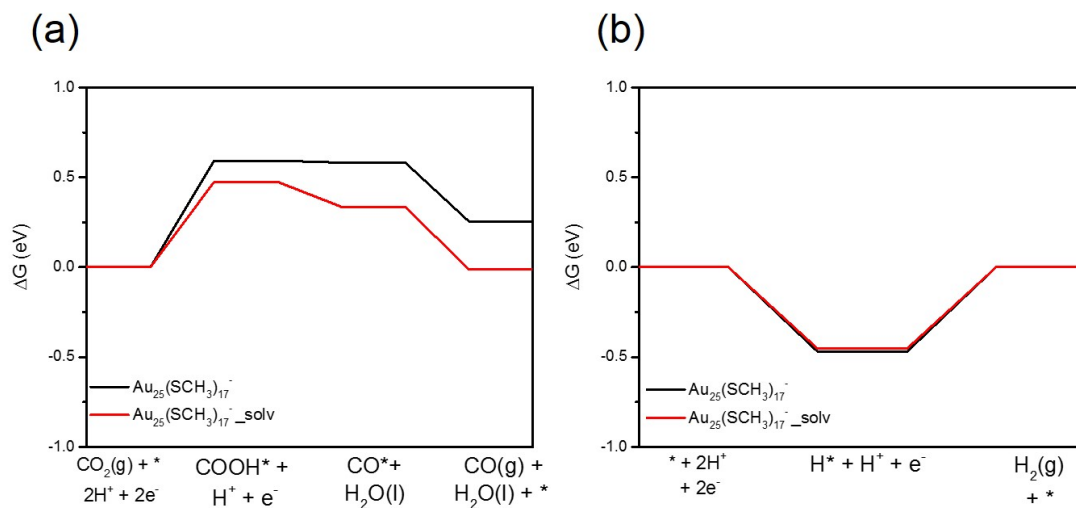


Figure A14: Free energy diagrams (ΔG) for the (a) reduction of CO_2 to CO and the (b) hydrogen evolution reaction on the $\text{Au}_{25}(\text{SCH}_3)_{17}^-$ NC with and without solvation effects in red and black, respectively. The $\text{Au}_{25}(\text{SCH}_3)_{17}^-$ NC and all reaction species were reoptimized with and without solvation in Turbomole using PBE/TZVP to utilize the implicit solvation model, COSMO.

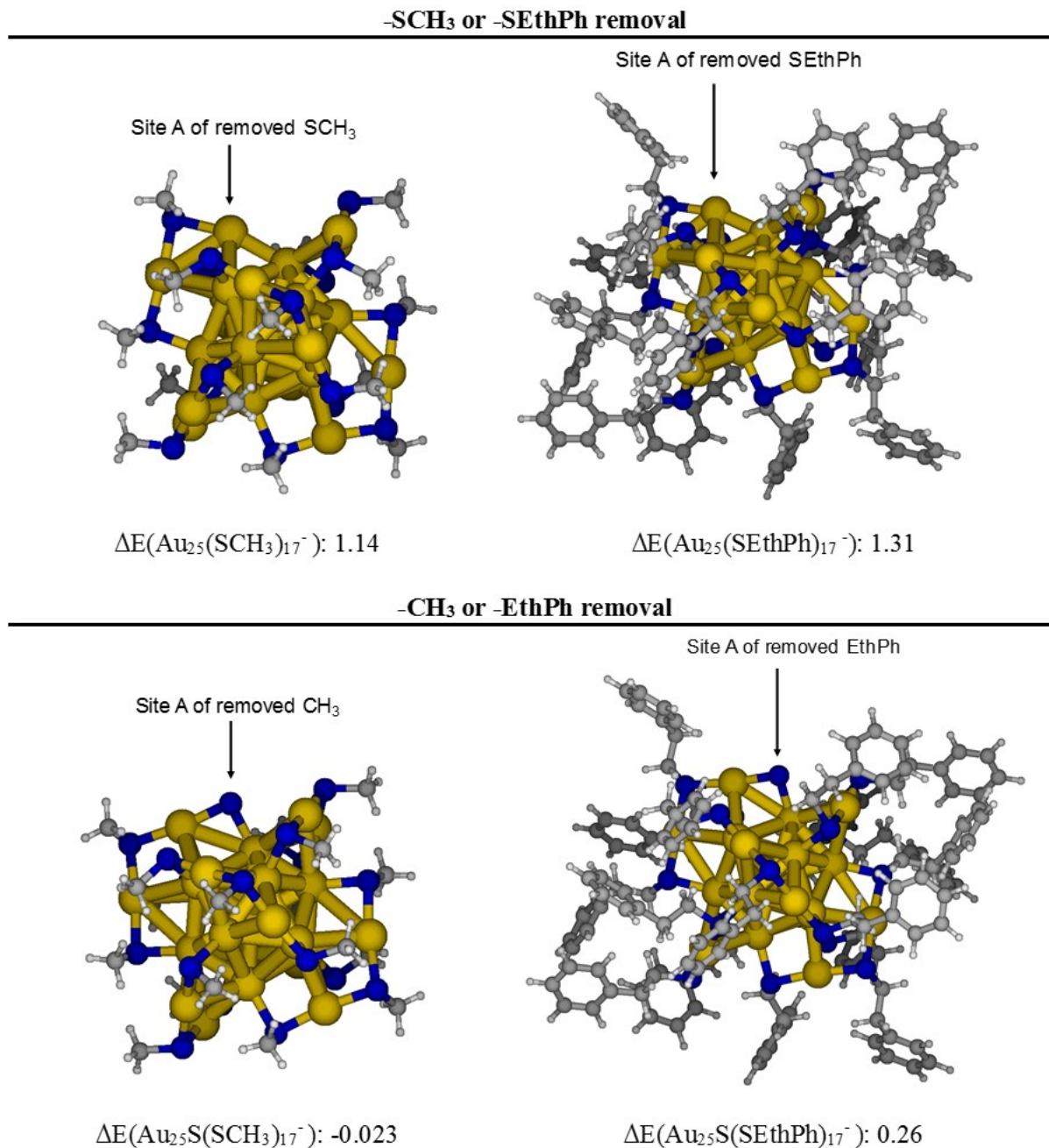


Figure A15: Electronic energy comparison for the reaction step of -SR and -R removal from $\text{Au}_{25}(\text{SCH}_3)_{18}^-$ and $\text{Au}_{25}(\text{EthPh})_{18}^-$. The similar magnitude of the electronic energies between ligand removal on $\text{Au}_{25}(\text{SCH}_3)_{18}^-$ and $\text{Au}_{25}(\text{EthPh})_{18}^-$ suggests that similar trends would hold for free energies, as electronic energies capture the majority of enthalpic contributions. This indicates that under reaction conditions removal of experimentally utilized ligands (-SEthPh) is possible.

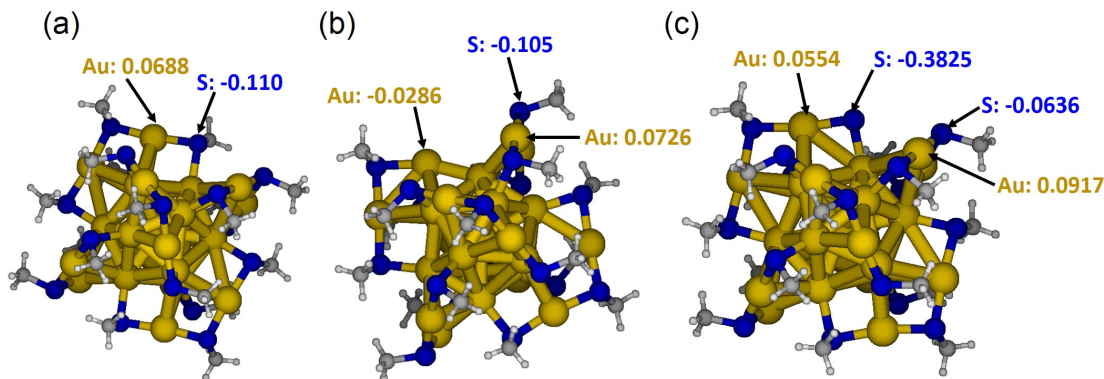


Figure A16: Bader charge analysis of select atoms from the negatively charged nanoclusters

(a) $\text{Au}_{25}(\text{SCH}_3)_{18}^-$, (b) $\text{Au}_{25}(\text{SCH}_3)_{17}^-$, (c) $\text{Au}_{25}\text{S}(\text{SCH}_3)_{17}^-$.

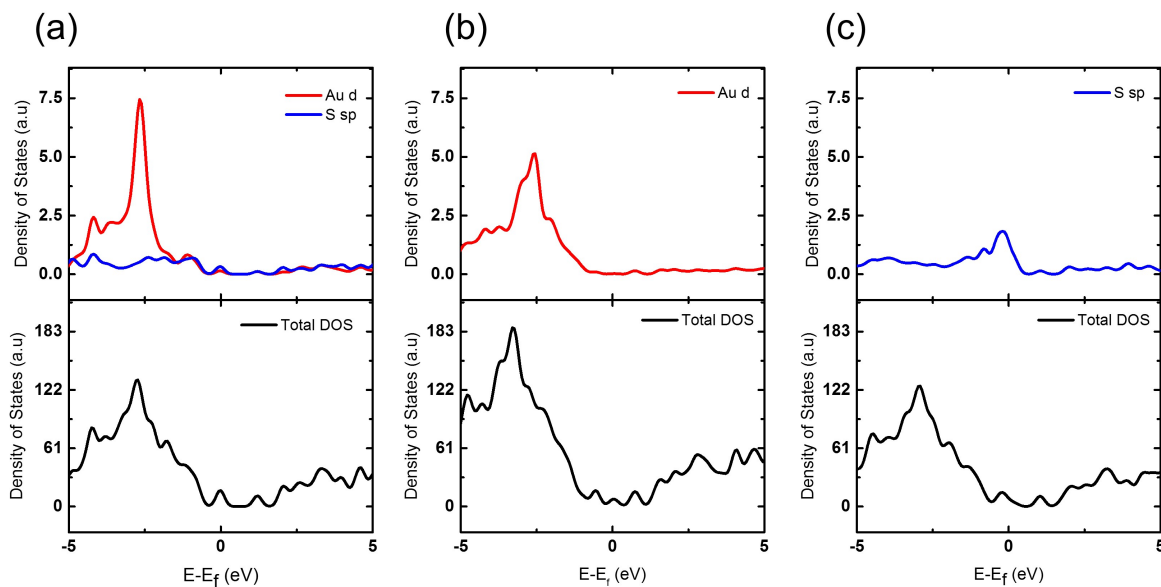


Figure A17: The projected density of states, PDOS (top graphs) for a ligand Au atom and a S atom of (a) $\text{Au}_{25}(\text{SCH}_3)_{18}^-$, the exposed Au atom of (b) $\text{Au}_{25}(\text{SCH}_3)_{17}^-$, and the exposed S atom of (c) $\text{Au}_{25}\text{S}(\text{SCH}_3)_{17}^-$. Comparison of the exposed S atom PDOS (s and p states) to the S atom PDOS of the fully protected NC, shows an increase in the electron density near the Fermi level (0 eV) of the $\text{Au}_{25}\text{S}(\text{SCH}_3)_{17}^-$ NC which contributes to the reactivity of the NC. The total density of states for the (a) $\text{Au}_{25}(\text{SCH}_3)_{18}^-$, (b) $\text{Au}_{25}(\text{SCH}_3)_{17}^-$, (c) $\text{Au}_{25}\text{S}(\text{SCH}_3)_{17}^-$ NCs are shown in the bottom graphs.

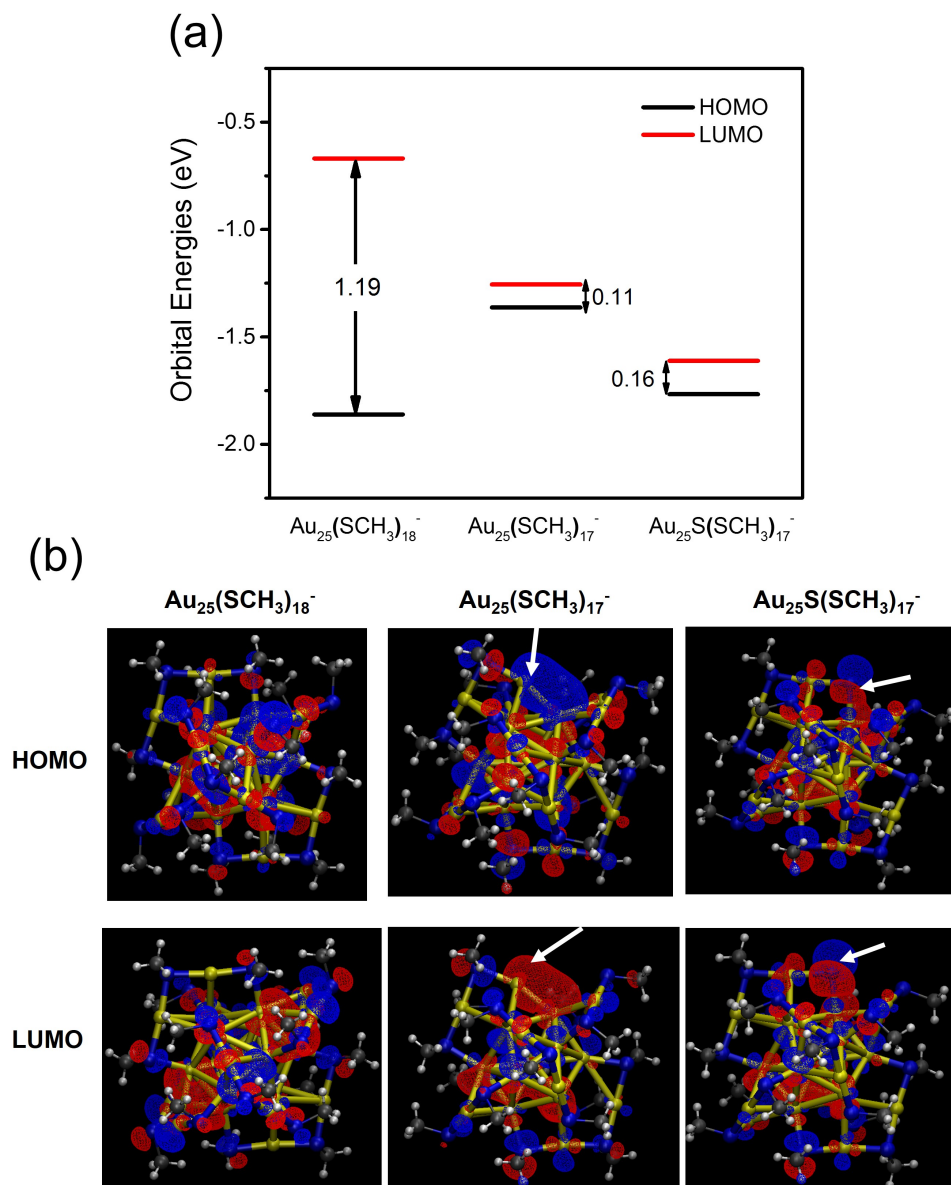


Figure A18: (a) HOMO-LUMO energy gaps (in eV) of the fully-protected and partially ligand-removed NCs. A dramatic decrease in the gap is observed with ligand removal. (b) Plots of the HOMO-LUMO orbitals. The white arrows point to the ligand removed sites ($-\text{SCH}_3$ and $-\text{CH}_3$) from the NCs. Compared to $\text{Au}_{25}(\text{SCH}_3)_{18}^-$, the electron density on the exposed Au site of $\text{Au}_{25}(\text{SCH}_3)_{17}^-$ becomes more localized and the exposed S site of $\text{Au}_{25}(\text{SCH}_3)_{17}^-$ becomes more directional, both of which contribute to the reactivity of these generated sites.

BIBLIOGRAPHY

- [1] J. Rockstrom, W. Steffen, K. Noone, A. Persson, F. S. Chapin, E. F. Lambin, T. M. Lenton, M. Scheffer, C. Folke, H. J. Schellnhuber, B. Nykvist, C. A. de Wit, T. Hughes, S. van der Leeuw, H. Rodhe, S. Sorlin, P. K. Snyder, R. Costanza, U. Svedin, M. Falkenmark, L. Karlberg, R. W. Corell, V. J. Fabry, J. Hansen, B. Walker, D. Liverman, K. Richardson, P. Crutzen, and J. A. Foley, “A safe operating space for humanity,” *Nature*, vol. 461, no. 7263, pp. 472–475, 2009.
- [2] W. Wang, S. P. Wang, X. B. Ma, and J. L. Gong, “Recent advances in catalytic hydrogenation of carbon dioxide,” *Chemical Society Reviews*, vol. 40, no. 7, pp. 3703–3727, 2011.
- [3] P. Tans and R. Keeling, “Trends in atmospheric carbon dioxide,” 2014.
- [4] J. Hansen, P. Kharecha, M. Sato, V. Masson-Delmotte, F. Ackerman, D. J. Beerling, P. J. Hearty, O. Hoegh-Guldberg, S. L. Hsu, C. Parmesan, J. Rockstrom, E. J. Rohling, J. Sachs, P. Smith, K. Steffen, L. Van Susteren, K. von Schuckmann, and J. C. Zacher, “Assessing “dangerous climate change”: Required reduction of carbon emissions to protect young people, future generations and nature,” *Plos One*, vol. 8, no. 12, pp. 1–26, 2013.
- [5] Y. W. Li, S. H. Chan, and Q. Sun, “Heterogeneous catalytic conversion of CO_2 : a comprehensive theoretical review,” *Nanoscale*, vol. 7, no. 19, pp. 8663–8683, 2015.
- [6] M. Aresta and A. Dibenedetto, “Utilisation of CO_2 as a chemical feedstock: opportunities and challenges,” *Dalton Transactions*, no. 28, pp. 2975–2992, 2007.
- [7] R. Zevenhoven, S. Eloneva, and S. Teir, “Chemical fixation of CO_2 in carbonates: Routes to valuable products and long-term storage,” *Catalysis Today*, vol. 115, no. 1-4, pp. 73–79, 2006.
- [8] G. Centi, E. A. Quadrelli, and S. Perathoner, “Catalysis for CO_2 conversion: a key technology for rapid introduction of renewable energy in the value chain of chemical industries,” *Energy & Environmental Science*, vol. 6, no. 6, pp. 1711–1731, 2013.

- [9] J. Y. Ye, C. J. Liu, D. H. Mei, and Q. F. Ge, "Methanol synthesis from CO_2 hydrogenation over a $\text{Pd-4/in}_2\text{O}_3$ model catalyst: A combined dft and kinetic study," *Journal of Catalysis*, vol. 317, pp. 44–53, 2014.
- [10] C. Tisseraud, C. Comminges, S. Pronier, Y. Pouilloux, and A. Le Valant, "The Cu-Zn synergy in methanol synthesis part 3: Impact of the composition of a selective Cu@ZnO core-shell catalyst on methanol rate explained by experimental studies and a concentric spheres model," *Journal of Catalysis*, vol. 343, pp. 106–114, 2016.
- [11] M. M. J. Li, Z. Y. Zeng, F. L. Liao, X. L. Hong, and S. C. E. Tsang, "Enhanced CO_2 hydrogenation to methanol over CuZn nanoalloy in Ga modified Cu/ZnO catalysts," *Journal of Catalysis*, vol. 343, pp. 157–167, 2016.
- [12] S. Kuld, M. Thorhauge, H. Falsig, C. F. Elkjaer, S. Helveg, I. Chorkendorff, and J. Sehested, "Quantifying the promotion of Cu catalysts by ZnO for methanol synthesis," *Science*, vol. 352, no. 6288, pp. 969–974, 2016.
- [13] C. Liu, T. R. Cundari, and A. K. Wilson, " CO_2 reduction on transition metal (Fe, Co, Ni, and Cu) surfaces: In comparison with homogeneous catalysis," *Journal of Physical Chemistry C*, vol. 116, no. 9, pp. 5681–5688, 2012.
- [14] Q. L. Tang, Q. J. Hong, and Z. P. Liu, " CO_2 fixation into methanol at Cu/ZrO₂ interface from first principles kinetic monte carlo," *Journal of Catalysis*, vol. 263, no. 1, pp. 114–122, 2009.
- [15] F. Solymosi, "The bonding, structure and reactions of CO_2 adsorbed on clean and promoted metal-surfaces," *Journal of Molecular Catalysis*, vol. 65, no. 3, pp. 337–358, 1991.
- [16] J. Ko, B. K. Kim, and J. W. Han, "Density functional theory study for catalytic activation and dissociation of CO_2 on bimetallic alloy surfaces," *Journal of Physical Chemistry C*, vol. 120, no. 6, pp. 3438–3447, 2016.
- [17] S. G. Wang, X. Y. Liao, D. B. Cao, C. F. Huo, Y. W. Li, J. G. Wang, and H. J. Jiao, "Factors controlling the interaction of CO_2 with transition metal surfaces," *Journal of Physical Chemistry C*, vol. 111, no. 45, pp. 16934–16940, 2007.
- [18] H. J. Freund and M. W. Roberts, "Surface chemistry of carbon dioxide," *Surface Science Reports*, vol. 25, no. 8, pp. 225–273, 1996.
- [19] F. Solymosi and G. Klivenyi, "HREELS study on the formation of CO_2 on a K-promoted Rh(111) surface," *Surface Science*, vol. 315, no. 3, pp. 255–268, 1994.
- [20] K. R. Hahn, M. Iannuzzi, A. P. Seitsonen, and J. Hutter, "Coverage effect of the CO_2 adsorption mechanisms on $\text{CeO}_2(111)$ by first principles analysis," *Journal of Physical Chemistry C*, vol. 117, no. 4, pp. 1701–1711, 2013.

- [21] M. Behrens, "Meso- and nano-structuring of industrial cu/zno/(al₂o₃) catalysts," *Journal of Catalysis*, vol. 267, no. 1, pp. 24–29, 2009.
- [22] F. Studt, M. Behrens, E. L. Kunkes, N. Thomas, S. Zander, A. Tarasov, J. Schumann, E. Frei, J. B. Varley, F. Abild-Pedersen, J. K. Norskov, and R. Schlögl, "The mechanism of co and co₂ hydrogenation to methanol over cu-based catalysts," *Chemcatchem*, vol. 7, no. 7, pp. 1105–1111, 2015.
- [23] L. C. Grabow and M. Mavrikakis, "Mechanism of methanol synthesis on cu through co₂ and co hydrogenation," *ACS Catalysis*, vol. 1, no. 4, pp. 365–384, 2011.
- [24] M. Behrens, F. Studt, I. Kasatkin, S. Kuehl, M. Haevecker, F. Abild-Pedersen, S. Zander, F. Girgsdies, P. Kurr, B.-L. Kniep, M. Tovar, R. W. Fischer, J. K. Norskov, and R. Schloegl, "The active site of methanol synthesis over cu/zno/al₂o₃ industrial catalysts," *Science*, vol. 336, no. 6083, pp. 893–897, 2012.
- [25] C. Yang, Z. Y. Ma, N. Zhao, W. Wei, T. D. Hu, and Y. H. Sun, "Methanol synthesis from co₂-rich syngas over a zro₂ doped cuzno catalyst," *Catalysis Today*, vol. 115, no. 1-4, pp. 222–227, 2006.
- [26] J. Nerlov and I. Chorkendorff, "Methanol synthesis from co₂, co, and h₂ over cu(100) and ni/cu(100)," *Journal of Catalysis*, vol. 181, no. 2, pp. 271–279, 1999.
- [27] J. Nerlov, S. Skerl, J. Wambach, and I. Chorkendorff, "Methanol synthesis from co₂, co and h₂ over cu(100) and cu(100) modified by ni and co," *Applied Catalysis a-General*, vol. 191, no. 1-2, pp. 97–109, 2000.
- [28] Y. Yang, M. G. White, and P. Liu, "Theoretical study of methanol synthesis from co₂ hydrogenation on metal-doped cu(111) surfaces," *Journal of Physical Chemistry C*, vol. 116, no. 1, pp. 248–256, 2012.
- [29] E. Vesselli, E. Monachino, M. Rizzi, S. Furlan, X. M. Duan, C. Dri, A. Peronio, C. Africh, P. Lacovig, A. Baldereschi, G. Comelli, and M. Peressi, "Steering the chemistry of carbon oxides on a nicu catalyst," *Acs Catalysis*, vol. 3, no. 7, pp. 1555–1559, 2013.
- [30] S. L. Han, X. L. Xue, X. C. Nie, H. Zhai, F. Wang, Q. Sun, Y. Jia, S. F. Li, and Z. X. Guo, "First-principles calculations on the role of ni-doping in cu-n clusters: From geometric and electronic structures to chemical activities towards co₂," *Physics Letters A*, vol. 374, no. 42, pp. 4324–4330, 2010.
- [31] Y. Yang and D. Cheng, "Role of composition and geometric relaxation in co₂ binding to cu-ni bimetallic clusters," *Journal of Physical Chemistry C*, vol. 118, no. 1, pp. 250–258, 2014.

- [32] J. Albo, M. Alvarez-Guerra, P. Castano, and A. Irabien, "Towards the electrochemical conversion of carbon dioxide into methanol," *Green Chemistry*, vol. 17, no. 4, pp. 2304–2324, 2015.
- [33] K. P. Kuhl, E. R. Cave, D. N. Abram, and T. F. Jaramillo, "New insights into the electrochemical reduction of carbon dioxide on metallic copper surfaces," *Energy & Environmental Science*, vol. 5, no. 5, pp. 7050–7059, 2012.
- [34] A. A. Peterson and J. K. Nørskov, "Activity descriptors for co₂ electroreduction to methane on transition-metal catalysts," *Journal of Physical Chemistry Letters*, vol. 3, no. 2, pp. 251–258, 2012.
- [35] C. W. Li and M. W. Kanan, "Co₂ reduction at low overpotential on cu electrodes resulting from the reduction of thick cu₂o films," *Journal of the American Chemical Society*, vol. 134, no. 17, pp. 7231–7234, 2012.
- [36] H. A. Hansen, J. B. Varley, A. A. Peterson, and J. K. Nørskov, "Understanding trends in the electrocatalytic activity of metals and enzymes for co₂ reduction to co," *Journal of Physical Chemistry Letters*, vol. 4, no. 3, pp. 388–392, 2013.
- [37] J. L. Qiao, Y. Y. Liu, F. Hong, and J. J. Zhang, "A review of catalysts for the electroreduction of carbon dioxide to produce low-carbon fuels," *Chemical Society Reviews*, vol. 43, no. 2, pp. 631–675, 2014.
- [38] B. Khezri, A. C. Fisher, and M. Pumera, "Co₂ reduction: the quest for electrocatalytic materials," *Journal of Materials Chemistry A*, vol. 5, no. 18, pp. 8230–8246, 2017.
- [39] E. L. Clark, C. Hahn, T. F. Jaramillo, and A. T. Bell, "Electrochemical co₂ reduction over compressively strained cu₂s surface alloys with enhanced multi-carbon oxygenate selectivity," *Journal of the American Chemical Society*, vol. 139, no. 44, pp. 15848–15857, 2017.
- [40] Gurudayal, J. Bullock, D. F. Sranko, C. M. Towle, Y. W. Lum, M. Hettick, M. C. Scott, A. Javey, and J. Ager, "Efficient solar-driven electrochemical co₂ reduction to hydrocarbons and oxygenates," *Energy & Environmental Science*, vol. 10, no. 10, pp. 2222–2230, 2017.
- [41] X. H. Zhou, R. Liu, K. Sun, Y. K. Chen, E. Verlage, S. A. Francis, N. S. Lewis, and C. X. Xiang, "Solar-driven reduction of 1 atm of co₂ to formate at 10 % energy-conversion efficiency by use of a tio₂-protected iii-v tandem photoanode in conjunction with a bipolar membrane and a pd/c cathode," *Acs Energy Letters*, vol. 1, no. 4, pp. 764–770, 2016.
- [42] A. A. Peterson, F. Abild-Pedersen, F. Studt, J. Rossmeisl, and J. K. Nørskov, "How copper catalyzes the electroreduction of carbon dioxide into hydrocarbon fuels," *Energy & Environmental Science*, vol. 3, no. 9, pp. 1311–1315, 2010.

- [43] Y. Hori, *Electrochemical CO₂ reduction on metal electrodes*, vol. 42. New York: Springer, 2008.
- [44] D. T. Whipple and P. J. A. Kenis, “Prospects of co₂ utilization via direct heterogeneous electrochemical reduction,” *Journal of Physical Chemistry Letters*, vol. 1, no. 24, pp. 3451–3458, 2010.
- [45] Y. Hori, K. Kikuchi, and S. Suzuki, “Production of co and ch₄ in electrochemical reduction of co₂ at metal-electrodes in aqueous hydrogencarbonate solution,” *Chemistry Letters*, no. 11, pp. 1695–1698, 1985.
- [46] H. Mistry, R. Reske, Z. H. Zeng, Z. J. Zhao, J. Greeley, P. Strasser, and B. R. Cuenya, “Exceptional size-dependent activity enhancement in the electroreduction of co₂ over au nanoparticles,” *Journal of the American Chemical Society*, vol. 136, no. 47, pp. 16473–16476, 2014.
- [47] W. L. Zhu, R. Michalsky, O. Metin, H. F. Lv, S. J. Guo, C. J. Wright, X. L. Sun, A. A. Peterson, and S. H. Sun, “Monodisperse au nanoparticles for selective electrocatalytic reduction of co₂ to co,” *Journal of the American Chemical Society*, vol. 135, no. 45, pp. 16833–16836, 2013.
- [48] D. R. Kauffman, D. Alfonso, C. Matranga, H. F. Qian, and R. C. Jin, “Experimental and computational investigation of au-25 clusters and co₂: A unique interaction and enhanced electrocatalytic activity,” *Journal of the American Chemical Society*, vol. 134, no. 24, pp. 10237–10243, 2012.
- [49] S. Back, M. S. Yeom, and Y. Jung, “Active sites of au and ag nanoparticle catalysts for co₂ electroreduction to co,” *Acs Catalysis*, vol. 5, no. 9, pp. 5089–5096, 2015.
- [50] B. Hvolbaek, T. V. W. Janssens, B. S. Clausen, H. Falsig, C. H. Christensen, and J. K. Nørskov, “Catalytic activity of au nanoparticles,” *Nano Today*, vol. 2, no. 4, pp. 14–18, 2007.
- [51] C. Rogers, W. S. Perkins, G. Veber, T. E. Williams, R. R. Cloke, and F. R. Fischer, “Synergistic enhancement of electrocatalytic co₂ reduction with gold nanoparticles embedded in functional graphene nanoribbon composite electrodes,” *Journal of the American Chemical Society*, vol. 139, no. 11, pp. 4052–4061, 2017.
- [52] A. S. Hall, Y. Yoon, A. Wuttig, and Y. Surendranath, “Mesostructure-induced selectivity in co₂ reduction catalysis,” *Journal of the American Chemical Society*, vol. 137, no. 47, pp. 14834–14837, 2015.
- [53] R. C. Jin, H. F. Qian, Z. K. Wu, Y. Zhu, M. Z. Zhu, A. Mohanty, and N. Garg, “Size focusing: A methodology for synthesizing atomically precise gold nanoclusters,” *Journal of Physical Chemistry Letters*, vol. 1, no. 19, pp. 2903–2910, 2010.

- [54] G. Li and R. C. Jin, "Atomically precise gold nanoclusters as new model catalysts," *Accounts of Chemical Research*, vol. 46, no. 8, pp. 1749–1758, 2013.
- [55] P. Haider, A. Urakawa, E. Schmidt, and A. Baiker, "Selective blocking of active sites on supported gold catalysts by adsorbed thiols and its effect on the catalytic behavior: A combined experimental and theoretical study," *Journal of Molecular Catalysis a-Chemical*, vol. 305, no. 1-2, pp. 161–169, 2009.
- [56] L. D. Menard, F. T. Xu, R. G. Nuzzo, and J. C. Yang, "Preparation of tio₂-supported au nanoparticle catalysts from a au-13 cluster precursor: Ligand removal using ozone exposure versus a rapid thermal treatment," *Journal of Catalysis*, vol. 243, no. 1, pp. 64–73, 2006.
- [57] Z. L. Wu, D. E. Jiang, A. K. P. Mann, D. R. Mullins, Z. A. Qiao, L. F. Allard, C. J. Zeng, R. C. Jin, and S. H. Overbury, "Thiolate ligands as a double-edged sword for co oxidation on ceo₂ supported au-25(sch₂ch₂ph)(18) nanoclusters," *Journal of the American Chemical Society*, vol. 136, no. 16, pp. 6111–6122, 2014.
- [58] D. R. Kauffman, J. Thakkar, R. Siva, C. Matranga, P. R. Ohodnicki, C. Zeng, and R. Jin, "Efficient electrochemical co₂ conversion powered by renewable energy," *ACS Applied Materials & Interfaces*, vol. 7, no. 28, pp. 15626–15632, 2015. PMID: 26121278.
- [59] D. R. Kauffman, D. Alfonso, C. Matranga, P. Ohodnicki, X. Deng, R. C. Siva, C. Zeng, and R. Jin, "Probing active site chemistry with differently charged au₂₅q nanoclusters (q = -1, 0, +1)," *Chem. Sci.*, vol. 5, pp. 3151–3157, 2014.
- [60] D. R. Alfonso, D. Kauffman, and C. Matranga, "Active sites of ligand-protected au-25 nanoparticle catalysts for co₂ electroreduction to co," *Journal of Chemical Physics*, vol. 144, no. 18, 2016.
- [61] X. T. Nie, H. F. Qian, Q. J. Ge, H. Y. Xu, and R. C. Jin, "Co oxidation catalyzed by oxide-supported au-25(sr)(18) nanoclusters and identification of perimeter sites as active centers," *Acs Nano*, vol. 6, no. 7, pp. 6014–6022, 2012.
- [62] X. Chen and H. Hakkinen, "Protected but accessible: Oxygen activation by a calixarene-stabilized undecagold cluster," *Journal of the American Chemical Society*, vol. 135, no. 35, pp. 12944–12947, 2013.
- [63] S. Zhao, N. Austin, M. Li, Y. Song, S. D. House, S. Bernhard, J. C. Yang, G. Mpourmpakis, and R. Jin, "Influence of atomic-level morphology on catalysis: The case of sphere and rod-like gold nanoclusters for co₂ electroreduction," *ACS Catalysis*, pp. 4996–5001, 2018.
- [64] G. Li, H. Abroshan, Y. X. Chen, R. C. Jin, and H. J. Kim, "Experimental and mechanistic understanding of aldehyde hydrogenation using au-25 nanoclusters with lewis acids: Unique sites for catalytic reactions," *Journal of the American Chemical Society*, vol. 137, no. 45, pp. 14295–14304, 2015.

- [65] S. Das, A. Goswami, M. Hesari, J. F. Al-Sharab, E. Mikmekova, F. Maran, and T. Asefa, “Reductive deprotection of monolayer protected nanoclusters: An efficient route to supported ultrasmall au nanocatalysts for selective oxidation,” *Small*, vol. 10, no. 8, pp. 1473–1478, 2014.
- [66] J. Fang, J. G. Li, B. Zhang, X. Yuan, H. Asakura, T. Tanaka, K. Teramura, J. P. Xie, and N. Yan, “The support effect on the size and catalytic activity of thiolated au-25 nanoclusters as precatalysts,” *Nanoscale*, vol. 7, no. 14, pp. 6325–6333, 2015.
- [67] J. A. Lopez-Sanchez, N. Dimitratos, C. Hammond, G. L. Brett, L. Kesavan, S. White, P. Miedziak, R. Tiruvalam, R. L. Jenkins, A. F. Carley, D. Knight, C. J. Kiely, and G. J. Hutchings, “Facile removal of stabilizer-ligands from supported gold nanoparticles,” *Nature Chemistry*, vol. 3, no. 7, pp. 551–556, 2011.
- [68] B. Zhang, S. Kaziz, H. Li, M. G. Hevia, D. Wodka, C. Mazet, T. Burgi, and N. Barrabes, “Modulation of active sites in supported au-38(sc2h4ph)(24) cluster catalysts: Effect of atmosphere and support material,” *Journal of Physical Chemistry C*, vol. 119, no. 20, pp. 11193–11199, 2015.
- [69] E. Andrews, S. Katla, C. Kumar, M. Patterson, P. Sprunger, and J. Flake, “Electrocatalytic reduction of co2 at au nanoparticle electrodes: Effects of interfacial chemistry on reduction behavior,” *Journal of the Electrochemical Society*, vol. 162, no. 12, pp. F1373–F1378, 2015.
- [70] J. A. Trindell, J. Clausmeyer, and R. M. Crooks, “Size stability and h2/co selectivity for au nanoparticles during electrocatalytic co2 reduction,” *J Am Chem Soc*, vol. 139, no. 45, pp. 16161–16167, 2017.
- [71] N. Austin, B. Butina, and G. Mpourmpakis, “Co2 activation on bimetallic cuni nanoparticles,” *Progress in Natural Science: Materials International*, vol. 26, no. 5, pp. 487–492, 2016.
- [72] A. D. Becke, “Density-functional thermochemistry .3. the role of exact exchange,” *Journal of Chemical Physics*, vol. 98, no. 7, pp. 5648–5652, 1993.
- [73] J. P. Perdew, K. Burke, and M. Ernzerhof, “Generalized gradient approximation made simple,” *Physical Review Letters*, vol. 77, no. 18, pp. 3865–3868, 1996.
- [74] K. Eichkorn, O. Treutler, H. Ohm, M. Haser, and R. Ahlrichs, “Auxiliary basis-sets to approximate coulomb potentials,” *Chemical Physics Letters*, vol. 240, no. 4, pp. 283–289, 1995.
- [75] K. Eichkorn, F. Weigend, O. Treutler, and R. Ahlrichs, “Auxiliary basis sets for main row atoms and transition metals and their use to approximate coulomb potentials,” *Theoretical Chemistry Accounts*, vol. 97, no. 1-4, pp. 119–124, 1997.

- [76] A. Schafer, H. Horn, and R. Ahlrichs, "Fully optimized contracted gaussian-basis sets for atoms li to kr," *Journal of Chemical Physics*, vol. 97, no. 4, pp. 2571–2577, 1992.
- [77] F. Weigend, M. Haser, H. Patzelt, and R. Ahlrichs, "Ri-mp2: optimized auxiliary basis sets and demonstration of efficiency," *Chemical Physics Letters*, vol. 294, no. 1-3, pp. 143–152, 1998.
- [78] R. Ahlrichs, M. Bar, M. Haser, H. Horn, and C. Kolmel, "Electronic-structure calculations on workstation computers - the program system turbomole," *Chemical Physics Letters*, vol. 162, no. 3, pp. 165–169, 1989.
- [79] S. Grimme, "Accurate description of van der waals complexes by density functional theory including empirical corrections," *Journal of Computational Chemistry*, vol. 25, no. 12, pp. 1463–1473, 2004.
- [80] S. Grimme, "Semiempirical gga-type density functional constructed with a long-range dispersion correction," *Journal of Computational Chemistry*, vol. 27, no. 15, pp. 1787–1799, 2006.
- [81] N. Austin and G. Mpourmpakis, "Understanding the stability and electronic and adsorption properties of subnanometer group xi monometallic and bimetallic catalysts," *Journal of Physical Chemistry C*, vol. 118, no. 32, pp. 18521–18528, 2014.
- [82] R. Ferrando, J. Jellinek, and R. L. Johnston, "Nanoalloys: From theory to applications of alloy clusters and nanoparticles," *Chemical Reviews*, vol. 108, no. 3, pp. 845–910, 2008.
- [83] M. J. Piotrowski, P. Piquini, and J. L. F. Da Silva, "Platinum-based nanoalloys ptntm55-n (tm=co, rh, au): A density functional theory investigation," *Journal of Physical Chemistry C*, vol. 116, no. 34, pp. 18432–18439, 2012.
- [84] C. Steffen, K. Thomas, U. Huniar, A. Hellweg, O. Rubner, and A. Schroer, "Software news and updates tmolex-a graphical user interface for turbomole," *Journal of Computational Chemistry*, vol. 31, no. 16, pp. 2967–2970, 2010.
- [85] J. P. K. Doye and D. J. Wales, "Global minima for transition metal clusters described by sutton-chen potentials," *New Journal of Chemistry*, vol. 22, no. 7, pp. 733–744, 1998.
- [86] C. Kittel, *Introduction to Solid State Physics*. Hoboken, NJ: John Wiley & Sons, Inc, 8th ed., 2005.
- [87] Y.-N. Wen and H.-M. Zhang, "Surface energy calculation of the fcc metals by using the maeam," *Solid State Communications*, vol. 144, no. 3-4, pp. 163–167, 2007.
- [88] L.-L. Wang and D. D. Johnson, "Predicted trends of core-shell preferences for 132 late transition-metal binary-alloy nanoparticles," *Journal of the American Chemical Society*, vol. 131, no. 39, pp. 14023–14029, 2009.

- [89] G. Mpourmpakis, A. N. Andriotis, and D. G. Vlachos, “Identification of descriptors for the co interaction with metal nanoparticles,” *Nano Letters*, vol. 10, no. 3, pp. 1041–1045, 2010.
- [90] B. Hammer and J. K. Norskov, “Electronic factors determining the reactivity of metal surfaces,” *Surface Science*, vol. 343, no. 3, pp. 211–220, 1995.
- [91] B. Hammer and J. K. Norskov, *Theoretical surface science and catalysis - Calculations and concepts*, vol. 45 of *Advances in Catalysis*, pp. 71–129. 2000.
- [92] R. Jin and K. Nobusada, “Doping and alloying in atomically precise gold nanoparticles,” *Nano Research*, vol. 7, no. 3, pp. 285–300, 2014.
- [93] H. Qian, D.-e. Jiang, G. Li, C. Gayathri, A. Das, R. R. Gil, and R. Jin, “Monoplatinum doping of gold nanoclusters and catalytic application,” *Journal of the American Chemical Society*, vol. 134, no. 39, pp. 16159–16162, 2012.
- [94] N. Austin, J. Ye, and G. Mpourmpakis, “Co₂ activation on cu-based zr-decorated nanoparticles,” *Catalysis Science & Technology*, 2017 (Advance Article).
- [95] J. VandeVondele, M. Krack, F. Mohamed, M. Parrinello, T. Chassaing, and J. Hutter, “Quickstep: Fast and accurate density functional calculations using a mixed gaussian and plane waves approach,” *Computer Physics Communications*, vol. 167, no. 2, pp. 103–128, 2005.
- [96] Y. K. Zhang and W. T. Yang, “Comment on ”generalized gradient approximation made simple”,” *Physical Review Letters*, vol. 80, no. 4, pp. 890–890, 1998.
- [97] J. VandeVondele and J. Hutter, “Gaussian basis sets for accurate calculations on molecular systems in gas and condensed phases,” *Journal of Chemical Physics*, vol. 127, no. 11, 2007.
- [98] S. Goedecker, M. Teter, and J. Hutter, “Separable dual-space gaussian pseudopotentials,” *Physical Review B*, vol. 54, no. 3, pp. 1703–1710, 1996.
- [99] G. Henkelman, B. P. Uberuaga, and H. Jonsson, “A climbing image nudged elastic band method for finding saddle points and minimum energy paths,” *Journal of Chemical Physics*, vol. 113, no. 22, pp. 9901–9904, 2000.
- [100] G. Henkelman, A. Arnaldsson, and H. Jonsson, “A fast and robust algorithm for bader decomposition of charge density,” *Computational Materials Science*, vol. 36, no. 3, pp. 354–360, 2006.
- [101] A. V. Ruban, H. L. Skriver, and J. K. Norskov, “Surface segregation energies in transition-metal alloys,” *Physical Review B*, vol. 59, no. 24, pp. 15990–16000, 1999.

- [102] Q. J. Hong and Z. P. Liu, "Mechanism of CO_2 hydrogenation over $\text{Cu}/\text{ZrO}_2(2\overline{1}0\overline{1}2)$ interface from first-principles kinetics monte carlo simulations," *Surface Science*, vol. 604, no. 21-22, pp. 1869–1876, 2010.
- [103] F. Arena, G. Italiano, K. Barbera, S. Bordiga, G. Bonura, L. Spadaro, and F. Frusteri, "Solid-state interactions, adsorption sites and functionality of $\text{Cu-ZnO}/\text{ZrO}_2$ catalysts in the CO_2 hydrogenation to CH_3OH ," *Applied Catalysis a-General*, vol. 350, no. 1, pp. 16–23, 2008.
- [104] A. N. Andriotis, G. Mpourmpakis, S. Broderick, K. Rajan, S. Datta, M. Sunkara, and M. Menon, "Informatics guided discovery of surface structure-chemistry relationships in catalytic nanoparticles," *Journal of Chemical Physics*, vol. 140, no. 9, p. 8, 2014.
- [105] I. A. Fisher and A. T. Bell, "In-situ infrared study of methanol synthesis from H_2/CO_2 over Cu/SiO_2 and $\text{Cu}/\text{ZrO}_2/\text{SiO}_2$," *Journal of Catalysis*, vol. 172, no. 1, pp. 222 – 237, 1997.
- [106] C. Schild, A. Wokaun, and A. Baiker, "On the hydrogenation of CO and CO_2 over copper/zirconia and palladium/zirconia catalysts," *Fresenius' Journal of Analytical Chemistry*, vol. 341, pp. 395–401, May 1991.
- [107] E. Ortelli, J. Wambach, and A. Wokaun, "Methanol synthesis reactions over a CuZr based catalyst investigated using periodic variations of reactant concentrations," *Applied Catalysis A: General*, vol. 216, no. 1, pp. 227 – 241, 2001.
- [108] D. James, Y. Yaghi, A. Natalie, V. Götz, and M. Giannis, "Design of copperbased bimetallic nanoparticles for carbon dioxide adsorption and activation," *ChemSusChem*, vol. 11, no. 7, pp. 1169–1178, 2018.
- [109] G. Li, H. Abroshan, C. Liu, S. Zhuo, Z. M. Li, Y. Xie, H. J. Kim, N. L. Ros, and R. C. Jin, "Tailoring the electronic and catalytic properties of Au_{25} nanoclusters via ligand engineering," *Acs Nano*, vol. 10, no. 8, pp. 7998–8005, 2016.
- [110] Z. Wu, J. Suhan, and R. Jin, "One-pot synthesis of atomically monodisperse, thiol-functionalized Au_{25} nanoclusters," *J. Mater. Chem.*, vol. 19, pp. 622–626, 2009.
- [111] H. Qian, M. Zhu, E. Lanni, Y. Zhu, M. E. Bier, and R. Jin, "Conversion of polydisperse Au nanoparticles into monodisperse Au_{25} nanorods and nanospheres," *The Journal of Physical Chemistry C*, vol. 113, no. 41, pp. 17599–17603, 2009.
- [112] L. Ma, K. Laasonen, and J. Akola, "Catalytic Activity of AuCu Clusters on $\text{MgO}(100)$: Effect of Alloy Composition for CO Oxidation," *Journal of Physical Chemistry C*, vol. 121, no. 20, SI, pp. 10876–10886, 2017.
- [113] Y.-G. Wang, D. Mei, V.-A. Glezakou, J. Li, and R. Rousseau, "Dynamic formation of single-atom catalytic active sites on ceria-supported gold nanoparticles," *Nature Communications*, vol. 6, MAR 2015.

- [114] M. Prakash, K. Mathivon, D. M. Benoit, G. Chambaud, and M. Hochlaf, "Carbon dioxide interaction with isolated imidazole or attached on gold clusters and surface: competition between sigma H-bond and pi stacking interaction," *Physical Chemistry Chemical Physics*, vol. 16, no. 24, pp. 12503–12509, 2014.
- [115] Y.-G. Wang, Y. Yoon, V.-A. Glezakou, J. Li, and R. Rousseau, "The Role of Reducible Oxide-Metal Cluster Charge Transfer in Catalytic Processes: New Insights on the Catalytic Mechanism of CO Oxidation on Au/TiO₂ from ab Initio Molecular Dynamics," *Journal of the American Chemical Society*, vol. 135, pp. 10673–10683, JUL 24 2013.
- [116] C. Liu, Y. Tan, S. Lin, H. Li, X. Wu, L. Li, Y. Pei, and X. C. Zeng, "CO Self-Promoting Oxidation on Nanosized Gold Clusters: Triangular Au-3 Active Site and CO Induced O-O Scission," *Journal of the American Chemical Society*, vol. 135, pp. 2583–2595, FEB 20 2013.
- [117] M. Zhu, C. M. Aikens, F. J. Hollander, G. C. Schatz, and R. Jin, "Correlating the crystal structure of a thiol-protected au₂₅ cluster and optical properties," *Journal of the American Chemical Society*, vol. 130, no. 18, pp. 5883–5885, 2008. PMID: 18407639.
- [118] J. K. Norskov, J. Rossmeisl, A. Logadottir, L. Lindqvist, J. R. Kitchin, T. Bligaard, and H. Jonsson, "Origin of the overpotential for oxygen reduction at a fuel-cell cathode," *Journal of Physical Chemistry B*, vol. 108, no. 46, pp. 17886–17892, 2004.
- [119] J. B. Varley, H. A. Hansen, N. L. Ammitzboll, L. C. Grabow, A. A. Peterson, J. Rossmeisl, and J. K. Norskov, "Ni-fe-s cubanesin co₂ reduction electrocatalysis: A dft study," *Acs Catalysis*, vol. 3, no. 11, pp. 2640–2643, 2013.
- [120] D. F. Gao, H. Zhou, J. Wang, S. Miao, F. Yang, G. X. Wang, J. G. Wang, and X. H. Bao, "Size-dependent electrocatalytic reduction of co₂ over pd nanoparticles," *Journal of the American Chemical Society*, vol. 137, no. 13, pp. 4288–4291, 2015.
- [121] S. A. Akhade, W. J. Luo, X. W. Nie, A. Asthagiri, and M. J. Janik, "Theoretical insight on reactivity trends in co₂ electroreduction across transition metals," *Catalysis Science & Technology*, vol. 6, no. 4, pp. 1042–1053, 2016.
- [122] A. Venzo, S. Antonello, J. A. Gascon, I. Guryanov, R. D. Leapman, N. V. Perera, A. Sousa, M. Zamuner, A. Zanella, and F. Maran, "Effect of the charge state (z = -1, 0, +1) on the nuclear magnetic resonance of monodisperse au-25 s(ch₂)(2)ph (18)(z) clusters," *Analytical Chemistry*, vol. 83, no. 16, pp. 6355–6362, 2011.
- [123] M. Z. Zhu, C. M. Aikens, M. P. Hendrich, R. Gupta, H. F. Qian, G. C. Schatz, and R. C. Jin, "Reversible switching of magnetism in thiolate-protected au-25 superatoms," *Journal of the American Chemical Society*, vol. 131, no. 7, pp. 2490–+, 2009.
- [124] M. Z. Zhu, W. T. Eckenhoff, T. Pintauer, and R. C. Jin, "Conversion of anionic au-25(sch₂ch₂ph)(18) (-) cluster to charge neutral cluster via air oxidation," *Journal of Physical Chemistry C*, vol. 112, no. 37, pp. 14221–14224, 2008.

- [125] G. Periyasamy, E. Durgun, J. Y. Raty, and F. Remacle, “Dft studies of solvation effects on the nanosize bare, thiolated, and redox active ligated au-55 cluster,” *Journal of Physical Chemistry C*, vol. 114, no. 38, pp. 15941–15950, 2010.
- [126] J. A. Keith and E. A. Carter, “Quantum chemical benchmarking, validation, and prediction of acidity constants for substituted pyridinium ions and pyridinyl radicals,” *Journal of Chemical Theory and Computation*, vol. 8, no. 9, pp. 3187–3206, 2012.
- [127] K. Chan, C. Tsai, H. A. Hansen, and J. K. Norskov, “Molybdenum sulfides and selenides as possible electrocatalysts for co2 reduction,” *Chemcatchem*, vol. 6, no. 7, pp. 1899–1905, 2014.
- [128] H. F. Qian, M. Y. Sfeir, and R. C. Jin, “Ultrafast relaxation dynamics of au-25(sr)(18)(q) nanoclusters: Effects of charge state,” *Journal of Physical Chemistry C*, vol. 114, no. 47, pp. 19935–19940, 2010.
- [129] J. Akola, M. Walter, R. L. Whetten, H. Hkkinen, and H. Grnbeck, “On the structure of thiolate-protected au25,” *Journal of the American Chemical Society*, vol. 130, no. 12, pp. 3756–3757, 2008. PMID: 18321117.
- [130] X. Hong, K. R. Chan, C. Tsai, and J. K. Norskov, “How doped mos2 breaks transition-metal scaling relations for co2 electrochemical reduction,” *Acs Catalysis*, vol. 6, no. 7, pp. 4428–4437, 2016.
- [131] D. Kim, C. L. Xie, N. Becknell, Y. Yu, M. Karamad, K. Chan, E. J. Crumlin, J. K. Norskov, and P. D. Yang, “Electrochemical activation of co2 through atomic ordering transformations of aucu nanoparticles,” *Journal of the American Chemical Society*, vol. 139, no. 24, pp. 8329–8336, 2017.
- [132] M. R. Singh, E. L. Clark, and A. T. Bell, “Effects of electrolyte, catalyst, and membrane composition and operating conditions on the performance of solar-driven electrochemical reduction of carbon dioxide,” *Physical Chemistry Chemical Physics*, vol. 17, no. 29, pp. 18924–18936, 2015.
- [133] S. Zhao, R. X. Jin, Y. B. Song, H. Zhang, S. D. House, J. C. Yang, and R. C. Jin, “Atomically precise gold nanoclusters accelerate hydrogen evolution over mos2 nanosheets: The dual interfacial effect,” *Small*, vol. 13, no. 43, p. 7, 2017.
- [134] S. Chretien, S. K. Buratto, and H. Metiu, “Catalysis by very small au clusters,” *Current Opinion in Solid State and Materials Science*, vol. 11, no. 5-6, pp. 62–75, 2007.
- [135] C. Shi, K. Chan, J. S. Yoo, and J. K. Norskov, “Barriers of electrochemical co2 reduction on transition metals,” *Organic Process Research & Development*, vol. 20, no. 8, pp. 1424–1430, 2016.

- [136] X. W. Nie, W. J. Luo, M. J. Janik, and A. Asthagiri, “Reaction mechanisms of CO_2 electrochemical reduction on $\text{Cu}(111)$ determined with density functional theory,” *Journal of Catalysis*, vol. 312, pp. 108–122, 2014.
- [137] N. Shuichi, “A unified formulation of the constant temperature molecular dynamics methods,” *The Journal of Chemical Physics*, vol. 81, no. 1, pp. 511–519, 1984.
- [138] N. Shuichi, “A molecular dynamics method for simulations in the canonical ensemble,” *Molecular Physics*, vol. 52, no. 2, pp. 255–268, 1984.